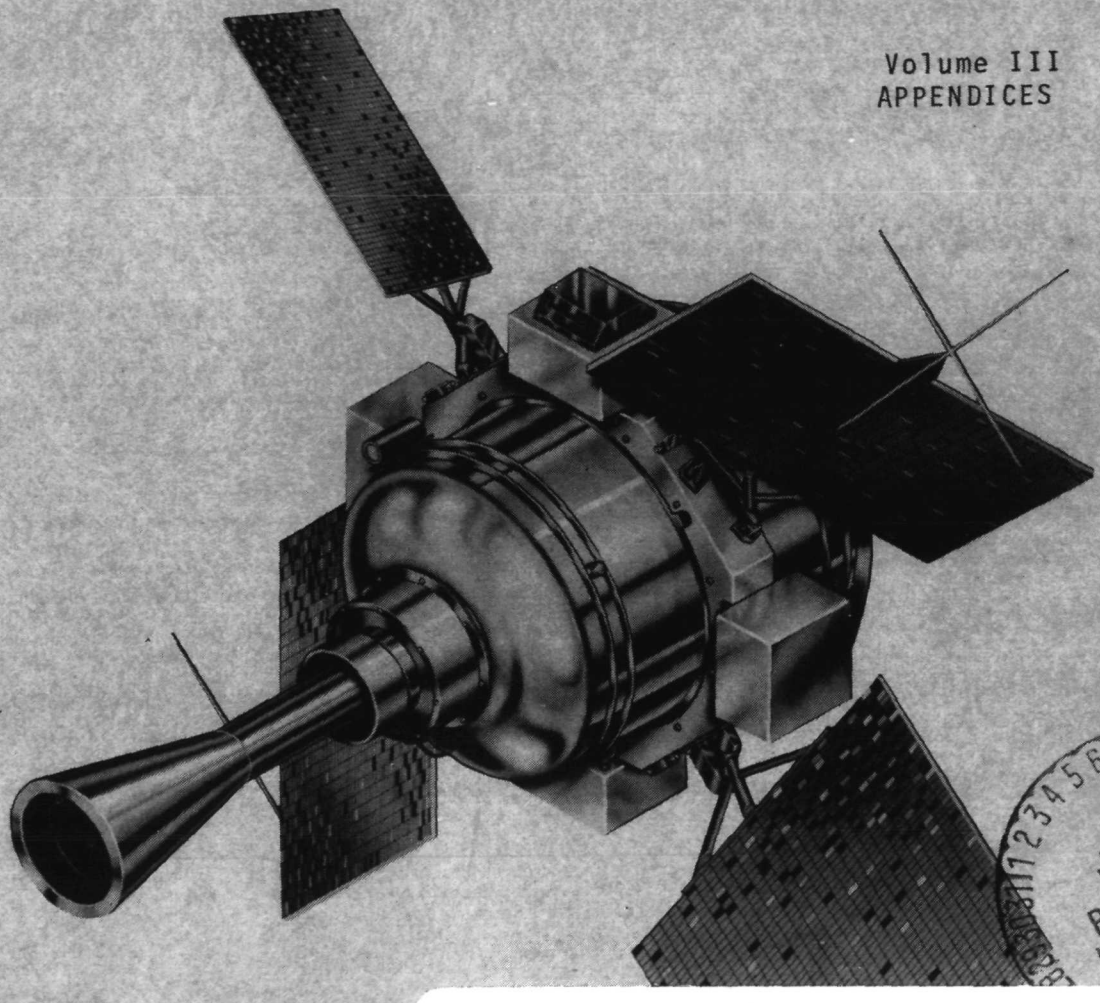
MISSION DEFINITION
for

STANFORD RELATIVITY SATELLITE

FINAL REPORT F71-07

Volume III
APPENDICES



JAN 1972
RECEIVED
NASA STI FACILITY
INPUT BRANCH

PREPARED FOR

MARSHALL SPACE FLIGHT CENTER
NATIONAL AERONAUTICS and
SPACE ADMINISTRATION

FACILITY FORM 602

(ACCESSION NUMBER)	(THRU)
141	GB
(PAGES)	(CODE)
CR 124797	3/
(NASA CR OR TMX OR AD NUMBER)	(CATEGORY)

BALL BROTHERS RESEARCH CORPORATION
SUBSIDIARY OF BALL CORPORATION
BOULDER, COLORADO

N72-14886 (F71-07-Vol-3-App) MISSION DEFINITION STUDY FOR STANFORD RELATIVITY SATELLITE. VOLUME 3: APPENDICES Final Report (Ball Bros. Research Corp.) 22 Dec. 1971 141 p
Unclas 11820 CSCL 22B
G3/31

Volume III

APPENDICES

Final Report

MISSION DEFINITION STUDY
FOR
STANFORD RELATIVITY SATELLITE

Prepared for

MARSHALL SPACE FLIGHT CENTER
of
NATIONAL AERONAUTICS AND SPACE ADMINISTRATION

22 December 1971

Report F71-07



BALL BROTHERS RESEARCH CORPORATION
SUBSIDIARY OF BALL CORPORATION
BOULDER, COLORADO

PRECEDING PAGE BLANK NOT FILMED

APPENDICES

CONTENTS

Appendix		Page
A	Derivation of Mission Reliability Number	A-1
B	Thermal Analysis Methods	B-1
C	Thermal Analysis Details (Dewar)	C-1
D	Structural Analysis of Cylinders	D-1
E	Reliability Plan	E-1
F	Quality Assurance Plan	F-1
G	Control System Simulation	G-1

Appendix A

DERIVATION OF MISSION RELIABILITY NUMBER

For this program, we have done a crude analysis to get a feel for the cost of doing the mission as a function of the following variables:

- Amount of redundancy in the spacecraft.
- Amount of care taken in building the spacecraft (functional and environmental tests, screening of components, quality control, etc.).
- The number of flights to accomplish the mission.

The following analysis derives the cost of doing the mission as a function of reliability per flight. Only hardware costs are used because most of the other mission costs are not a strong function of reliability. Information to be used as inputs to this study is not known accurately, but an analysis such as this is still much better than just shooting in the dark. Satellite hardware costs are stated in terms of booster costs since only this ratio is important in deriving the reliability number.

To find the cost of performing the mission, it is necessary to determine the most probable number of flights and the cost per flight. Both of these are functions of the reliability per flight. Figure A-1 is a plot of cost per flight vs. reliability and required number of flights vs. reliability.

The cost per flight was the more difficult information to obtain. Guesses at the cost per flight (cost of hardware and launch support for both the booster and satellite) as a function of reliability were arrived at as follows: The launch booster cost is essentially a fixed quantity. It was assumed that the satellite could not be built for any less than 0.6 of a booster cost, no matter how many corners were cut. Thus, this gives us a point

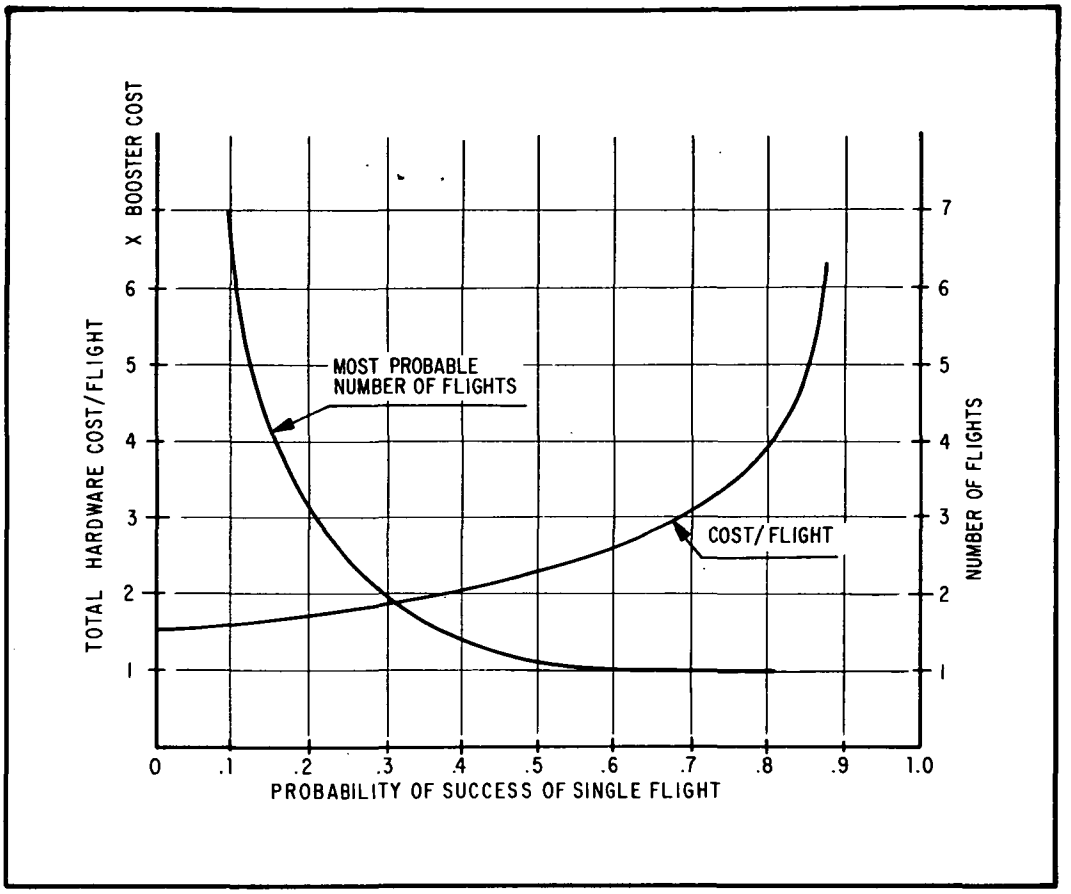


Fig. A-1 Cost per Flight and Most Probable Number of Flights

on the left hand side of Fig. A-1. The cost of the spacecraft with redundancy only in highly critical series elements and doing normal testing was assumed to be about 1.6 boosters. Since this was assumed to be a typical program, a reliability was assigned which is consistent with past OSO's (0.9 vehicle x 0.7 satellite = 0.63).

For the purpose of this curve, higher reliabilities were assumed to be accomplished by greater redundancy within the spacecraft.

The third point was derived assuming total redundancy within the spacecraft. The cost of the additional redundancy and the necessary additional testing was assumed to double the cost of the

satellite. However, the reliability improvement only affects the satellite, so the total reliability improvement only results in a flight reliability of 0.82. The final point was derived assuming that all systems were backed up twice (each system had three parallel paths). Because of complexities of such a spacecraft, additional testing costs were assumed, and total hardware cost could be over six times the booster cost. Here again only the satellite reliability was increased, so that the total flight reliability would be 0.87. Note that this curve has to be asymptotic to the assumed vehicle reliability of 0.9.

The most probable number of flights is the number that gives a mission probability of success of 0.5 with a given probability of success for each flight. For the special case where the chance for success is 0.5 for n tries and n is greater than 1, the probability equation for discrete events reduces to approximately:

$$0.85\ pn = 0.5 \text{ or}$$

$$p = \frac{0.59}{n}$$

p = probability of success for one try

n = number of tries (n > 1)

The points on the curve are the solution to this equation. Since there cannot be less than one flight, the curve is made asymptotic to 1 for high reliability numbers.

Figure A-2 shows the product of the hardware cost per flight times the most probable number of flights, which is the most probable cost for the mission hardware. The cost of the mission goes to infinity as we try to approach the vehicle limit reli-

ability of 0.9. At the low end of reliability, the cost increases because we cannot reduce the cost of the spacecraft no matter how small the reliability is, and the vehicle cost is fixed. Note that the cost curve has a rather flat bottom. It is desirable, of course, to work at the high success (right hand) portion of the bottom, since this end is more likely to result in early data for the experimenters. The chance of getting the relativity data on the first flight is higher, but the cost is not significantly increased.

For this set of input assumptions, a flight reliability of something like 0.75 will result in only a moderate increase above the minimum costs for the mission. This corresponds to a satellite reliability of 0.83.

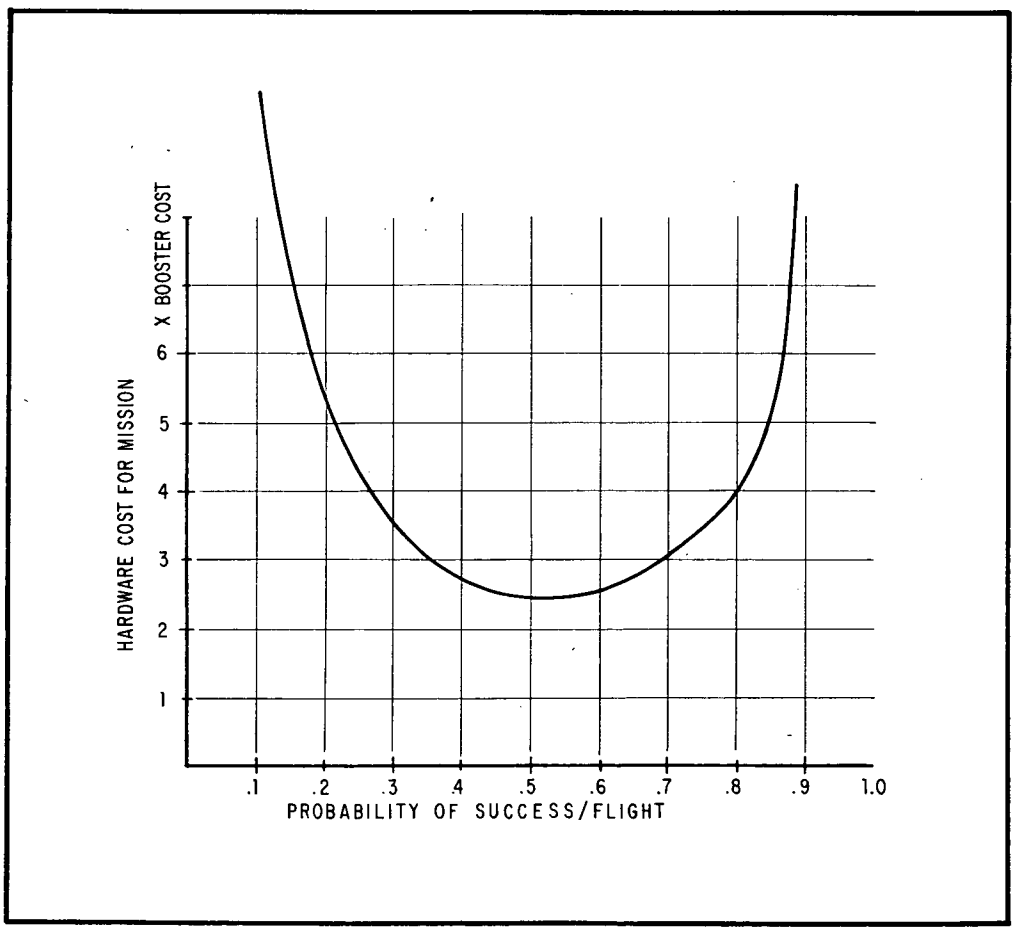


Fig. A-2 Most Probable Total Orbiting Hardware Cost per Completed Mission

Appendix B

THERMAL ANALYSIS METHODS

Appendix B
THERMAL ANALYSIS METHODS

The thermal analysis is based upon the requirement of an overall heat balance for any component. The heat balance equation mathematically states that the heat input to the spacecraft or component from direct solar radiation, the solar radiation reflected from the earth, the direct planetary radiation, the electrical heating of the power components, and aerodynamic heating--all must equal the heat radiated from the spacecraft plus the heat absorbed by the change of temperature of the spacecraft.

An exact analysis of any structure involves solutions of non-linear integro-differential equations of extreme complexity. Because a closed form solution for any complex structure treated as a continuous system is impractical--if not impossible--numerical methods must be used. Mathematical simplification results when a continuous system is replaced by a series of discrete elements that are coupled thermally. These elements, or nodes, are treated as having constant temperatures at any point in time but differing discontinuously in temperature from the temperatures of the adjacent elements. This is the approach used at BBRC. A further advantage of handling the analysis through a solution by elements is that it easily permits adding or changing components for future studies.

The general equation solved for each node of the thermal model is presented below, where it is shown that the temperature of each node is dependent upon the temperature of other nodes in the system. Thus, a temperature time history for a particular node results only from the solution of N simultaneous equations producing the temperature time histories of each node in the system.

For the analysis, the first step is to divide the structure and components into elements or nodes. The assembly of nodes that approximates the system forms the thermal model. The heat balance for each node involves the heat capacity of the node, the

thermal radiation and conduction interchange between the node and all others, the external heat absorbed by that node, and the electrical heat dissipation within the node. The external heating is determined for the particular orbit or thermal environment. The heating parameters determined by the environment are the duration of sunlight and darkness, the duration and intensity of solar and albedo radiation, the intensity of planetary radiation, and aerodynamic heating. With this information, the time histories for all of the nodes can be obtained.

When the temperature time history of a node has been calculated, it becomes apparent whether the node will operate within the specified temperature range. If it is not satisfactory, the node temperature can generally be varied by altering the surface finish of the node or neighboring nodes to increase or decrease the amount of thermal radiation exchanged and by altering the conduction paths between nodes. In diagnosing the problem of exactly what items to alter, a BBRC heat flow computer program is used; it calculates the amount and direction of the heat flow from each model node. The flow diagram of the analytical effort is shown in Fig. B-1.

B.1 HEAT BALANCE EQUATION

The calculation of the temperature time histories of the components requires determining the thermal behavior of each node within its own environment. When this environment is composed of other nodes, each with its own thermal environment dependent upon other nodes, the temperature time history of all nodes must be obtained simultaneously. Thus, it is necessary to set up one specific equation for each node of the system and solve all of these equations simultaneously. The transient equation describing the thermal behavior of a particular node is as follows:

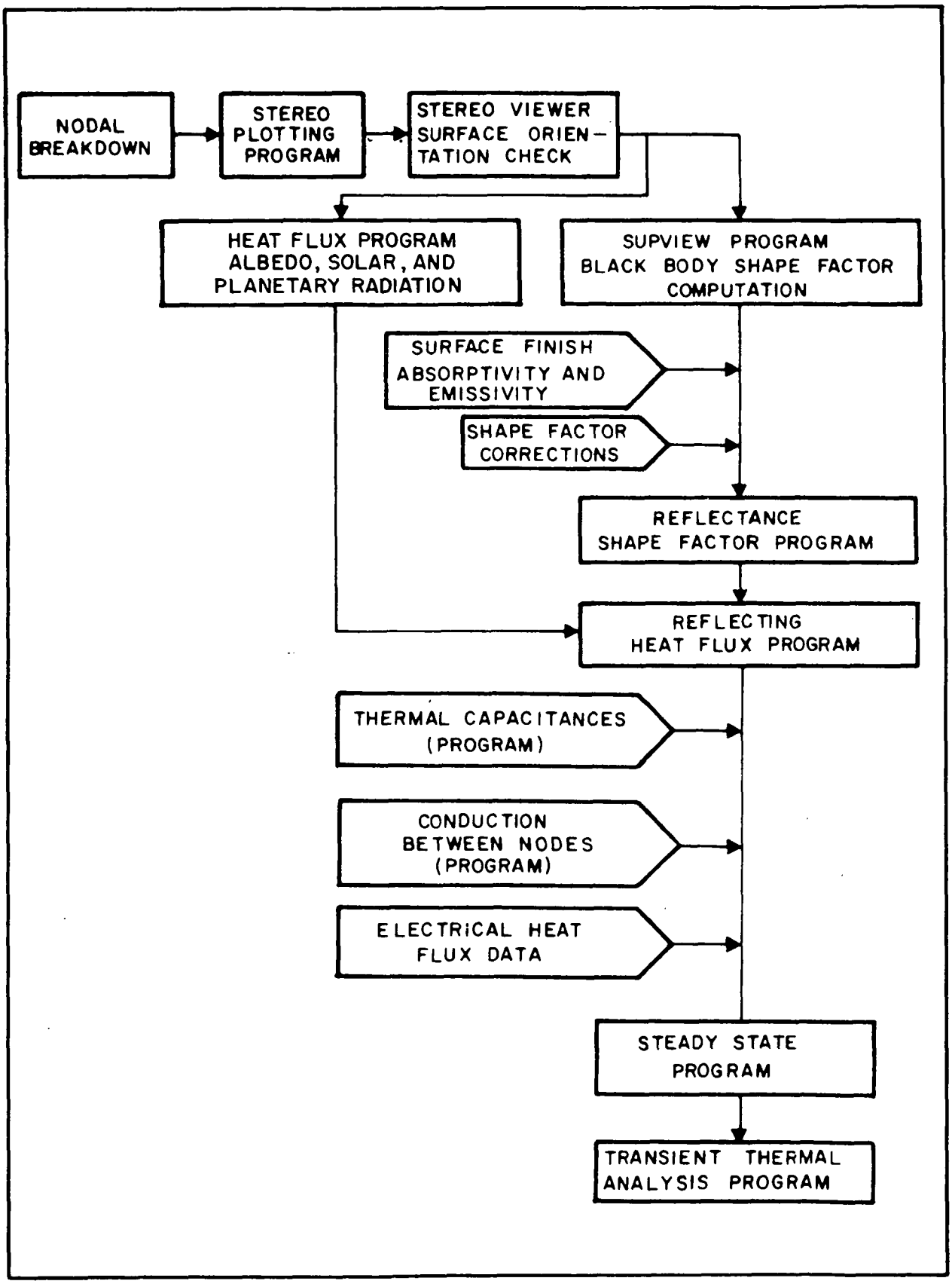


Fig. B-1 Thermal Analysis Program

$$M_n c_{P_n} \frac{dT_n}{d\theta} = \sum_m b_{n,m}\sigma \left(T_m^4 - T_n^4 \right) + \sum_m c_{n,m} \left(T_m - T_n \right) + D_n K_n(\theta)$$

where M_n = mass of node n

c_{P_n} = specific heat of node n

T_n = absolute temperature of node n

θ = time

$b_{n,m}$ = radiation exchange factor between node n and node m

σ = Stefan-Boltzmann constant

T_m = absolute temperature of node m

$c_{n,m}$ = thermal conductance between node n and node m

$K_n(\theta)$ = absorbed solar, albedo, planetary radiation, electrical and aerodynamic heating of node n (in general, this is a time dependent input table)

D_n = multiplying factor (usually unity)

This equation is derived by forming a heat balance on a node considering all energy entering and leaving the node and equating the difference to the energy absorbed or lost by the node. The meaning of each term starting with the left-hand side is as follows:

(1) The term on the left represents the rate of change of the energy stored in node n.

(2) The first term on the right represents the net energy exchange by radiation between all nodes of the system and node n.

(3) The second term on the right represents the net energy exchange by conduction between all other nodes of the system and node n. Note that this term is zero for all nodes except those in intimate contact with node n.

(4) The third term on the right represents the heat input rate into node n from joule heating, aerodynamic heating, and absorbed solar, albedo and planetary radiation.

The resulting set of differential equations is solved using the BBRC Transient Temperature Computer Program with a CDC-3800 computer. This program in addition to utilizing the analytical method described above also incorporates the radiosity method (see "Radiation Analysis by the Network Method", A. K. Oppenheim, Trans. ASME, May 1956, P. 726) to be used for systems modeled with 50 or less nodes. This method circumvents the need for the use of the Reflectance Shape Factor and the Reflecting Heat Flux Programs; it permits a rapid evaluation of surface finish requirements by permitting individual, separate changes of surface finishes where the previously described method does not.

B.2 MATHEMATICAL THERMAL MODEL

The mathematical thermal model consists of the subdivisions or nodes of the system as previously described, the numerical values of the thermophysical properties of mass and specific heat of each subdivision, and the parameters between the subdivisions. The heat input rates to each of the subdivisions or nodes are

not considered a part of the thermal model, since changing the environmental parameters changes only the heat inputs while the physical characteristics of the thermal model remain unchanged.

The components or subdivisions of the spacecraft are simulated by simple blocklike shapes representing the actual shapes as closely as possible. The quadrilateral sides of those blocks, or nodes, are located relative to each other by the coordinates of their corners. A common coordinate system is used for the entire structure. The resulting model is checked visually for accuracy by using the corner coordinates for computer plotted stereo drawings.

The thermo-physical properties of the structure are then combined with the nodal geometry and a sequence of computer programs used to obtain the instrument temperature distributions. The first computation is to obtain the geometrical view factors between nodes. This provides quantitative values for how much each node "sees" all other nodes; the computer program used accounts for the blockage and partial blockage of nodes by other nodes.

Since thermal nodes are seldom thermally black, multiple reflections occur which, except in the radiosity method, require a reflecting view factor computation to account for the surface finish emissivities of the nodes involved. Combined with the reflecting view factor computer program are programs to balance the accumulated view factors so that small errors in each view factor calculation will not result in each node radiating either more or less than its actual hemispherical radiative total and to eliminate reflective view factors which are negligible so as not to cause unnecessarily long computer runs for subsequent computations. The reflecting view factors are then combined

with the conductances, capacitances, and heat inputs to the heat balance equations to compute the temperature of each node.

B.3 ENVIRONMENTAL HEAT FLUX INPUT

The heat sources from the environment of an earth-orbiting spacecraft are as follows:

- Solar radiation impinging directly upon the spacecraft
- The solar radiation that is first reflected from the earth in direct ratio to the earth albedo constant and then impinges upon the spacecraft
- The impinging radiation originating at the earth due to the absolute temperature of the earth

These thermal contributions are defined here as solar, albedo, and planetary radiation, respectively.

The thermal environment of the spacecraft is strongly dependent upon the angle, designated as β, between the spacecraft orbital plane and the solar vector. When this angle is zero, a "high noon" orbit exists for which the albedo energy impinging upon the spacecraft is a maximum. When this angle is 90 degrees, the spacecraft is in the sunlight continuously and the albedo energy input is a minimum. The β angle varies in value as a function of time due to the orbital regression of the line of nodes and the seasonal variation of the angle of inclination with the ecliptic.

For the calculations of the solar, albedo and planetary radiation input rates to the mathematical model, all blockages and

shielding are taken into account in a CDC-3800 computer program.

In addition to calculating initially impinging heat fluxes, it is necessary, except when using the radiosity method described above, to calculate the distribution of the heat fluxes over the model nodes resulting from the reflection and re-reflection between nodal surfaces that are not thermally black for the impinging radiation. In general, the method used for these calculations is the same as that described by McAdams*, except that the reflected portion of the impinging flux is set up mathematically as an equivalent emission from the nodal surface. The calculations for N nodes require the simultaneous solution of N algebraic equations--for which numerous standard computational methods exist (for use with a computer such as the CDC-3800). This computation is required for each point in time for which environmental fluxes are computed. Since--in general--the surface absorptivity for solar and albedo radiation wavelengths is different from that for the long wavelength radiation from the planet, the reflections for solar-albedo fluxes and planetary fluxes must be computed separately.

B.4 TEMPERATURE INFORMATION

The computer print outs on the following pages give complete temperature information for all nodes. The plots presented in Section 6.2, Volume I, are from selected nodes of this data.

* W. H. McAdams, "Heat Transmission," (Third Edition), pp. 72-75, McGraw-Hill, New York, New York, 1954.

STEADY STATE $\beta = 0$, $\phi = 0$

33 ITERATIONS WERE PERFORMED
GREATEST TEMP. DIFFERENCE ON LAST ITERATION WAS 0.009378

MEAN TEMP.'S (DEGREES CENT) -----

2	-68.378	3	-65.712	4	-42.603	5	-53.334	6	-49.353
7	-53.066	8	-58.426	9	-60.592	10	-60.915	11	-60.785
12	-59.090	14	-60.068	15	-39.425	16	-41.047	17	-47.793
18	-46.890	25	-49.976	26	-48.331	27	-49.655	28	-58.208
29	-59.410	30	-61.498	31	-58.372	32	-59.626	50	15.583
60	-3.988	70	20.922	80	45.504	81	44.988	82	44.567
115	15.260	116	14.738	117	9.441	118	9.775		

STEADY STATE $\beta = 90$, $\phi = 0$

38 ITERATIONS WERE PERFORMED
GREATEST TEMP. DIFFERENCE ON LAST ITERATION WAS 0.009377

MEAN TEMP.'S (DEGREES CENT) -----

2	-59.269	3	-53.458	4	-63.236	5	-63.474	6	-53.693
7	-36.700	8	-29.481	9	-36.373	10	-53.633	11	-63.478
12	-67.700	14	-59.261	15	-66.343	16	-27.660	17	-26.602
18	-65.652	25	-62.566	26	-64.499	27	-35.163	28	-27.581
29	-35.636	30	-64.405	31	-62.735	32	-68.859	50	45.177
60	-83.304	70	44.205	80	-55.025	81	-75.551	82	-81.034
115	2.470	116	24.251	117	24.317	118	2.625		

STEADY STATE $\beta = 90$, $\phi = 45$

39 ITERATIONS WERE PERFORMED
GREATEST TEMP. DIFFERENCE ON LAST ITERATION WAS 0.008362

MEAN TEMP.'S (DEGREES CENT) -----

2	-59.827	3	-54.073	4	-64.740	5	-68.713	6	-66.823
7	-57.132	8	-39.173	9	-32.293	10	-38.161	11	-56.629
12	-66.691	14	-60.517	15	-70.931	16	-66.728	17	-30.702
18	-63.009	25	-67.701	26	-67.788	27	-56.410	28	-37.998
29	-33.095	30	-36.789	31	-55.957	32	-67.756	50	27.946
60	-87.242	70	-87.382	80	30.097	81	23.067	82	21.701
115	-0.446	116	4.269	117	23.311	118	5.492		

MINIMUM INTEGRATION INTERVAL = 2.2352684-001 FOR NODE 10

HEAT FLUX--- FLUX INTO NODE IS (+), FLUX OUT IS (-)

12	-57.703	14	-56.102	15	-26.495	16	-27.950	17	-52.716
18	-49.104	25	-47.442	26	-43.920	27	-47.278	28	-56.561
29	-58.709	30	-61.319	31	-58.717	32	-57.528	50	36.320
60	15.973	70	45.198	80	69.723	81	68.389	82	68.239
115	15.823	116	15.248	117	9.940	118	10.231	1000	-273.111

CYCLE NO 5 THETA= 1.04000

N	TEMP (DEG	CENT)							
2	-67.615	3	-55.205	4	-42.025	5	-49.842	6	-44.886
7	-49.630	8	-56.924	9	-61.217	10	-61.879	11	-61.330
12	-57.716	14	-57.122	15	-53.620	16	-56.086	17	-78.145
18	-70.916	25	-47.686	26	-43.682	27	-47.497	28	-57.020
29	-59.520	30	-62.509	31	-59.644	32	-57.997	50	14.663
60	-0.373	70	21.882	80	44.665	81	38.918	82	42.097
115	15.830	116	15.251	117	9.816	118	10.134	1000	-273.111

CYCLE NO 5 THETA= 1.12000

N	TEMP (DEG	CENT)							
2	-72.120	3	-65.422	4	-43.605	5	-50.170	6	-45.509
7	-49.947	8	-57.213	9	-61.613	10	-62.557	11	-61.744
12	-57.960	14	-57.989	15	-56.280	16	-57.509	17	-75.795
18	-69.574	25	-48.185	26	-44.326	27	-47.971	28	-57.479
29	-59.994	30	-63.201	31	-60.219	32	-58.429	50	-0.731
60	-12.180	70	5.274	80	26.336	81	18.729	82	23.248
115	15.757	116	15.178	117	9.692	118	10.028	1000	-273.111

CYCLE NO 5 THETA= 1.24000

N	TEMP (DEG	CENT)							
2	-77.261	3	-65.896	4	-45.160	5	-51.132	6	-47.046
7	-50.862	8	-57.855	9	-62.140	10	-63.450	11	-62.289
12	-58.520	14	-59.360	15	-59.631	16	-59.129	17	-71.759
18	-66.823	25	-48.971	26	-45.705	27	-48.689	28	-58.134
29	-60.529	30	-64.026	31	-60.843	32	-59.017	50	-17.676
60	-26.016	70	-12.936	80	5.902	81	-2.447	82	2.538
115	15.623	116	15.054	117	9.520	118	9.876	1000	-273.111

CYCLE NO 5 THETA= 1.32000

N	TEMP (DEG	CENT)							
2	-79.887	3	-66.278	4	-45.717	5	-52.004	6	-48.363
7	-51.687	8	-58.356	9	-62.427	10	-63.917	11	-62.580
12	-58.966	14	-60.312	15	-62.276	16	-61.223	17	-69.174
18	-64.792	25	-49.567	26	-46.869	27	-49.224	28	-58.557
29	-60.787	30	-64.422	31	-61.122	32	-59.387	50	-26.077
60	-33.300	70	-22.036	80	-4.542	81	-12.799	82	-7.936
115	15.522	116	14.965	117	9.417	118	9.785	1000	-273.111

CYCLE NO 5 THETA= 1.44000

N	TEMP (DEG CENT)							
2	-82.838	3	-66.850	4	-46.514	5	-53.526	6	-50.611
7	-53.178	8	-59.121	9	-62.575	10	-64.108	11	-62.713
12	-59.663	14	-61.711	15	-67.876	16	-67.576	17	-65.807
18	-61.690	25	-50.687	26	-49.001	27	-50.290	28	-59.242
29	-61.063	30	-64.620	31	-61.336	32	-59.971	50	-36.055
60	-41.360	70	-33.115	80	-17.670	81	-25.680	82	-21.072
115	15.342	116	14.805	117	9.280	118	9.662	1000	-273.111

CYCLE NO 5 THETA= 1.52000

N	TEMP (DEG CENT)							
2	-83.360	3	-67.139	4	-46.744	5	-54.564	6	-52.090
7	-54.216	8	-59.608	9	-62.477	10	-63.884	11	-62.591
12	-60.105	14	-62.575	15	-52.397	16	-51.540	17	-50.487
18	-48.748	25	-51.429	26	-50.444	27	-51.026	28	-59.661
29	-61.131	30	-64.460	31	-61.339	32	-60.310	50	-38.704
60	-43.438	70	-36.217	80	-21.676	81	-28.661	82	-24.907
115	15.205	116	14.679	117	9.201	118	9.594	1000	-273.111

CYCLE NO 5 THETA= 1.64000

N	TEMP (DEG CENT)							
2	-75.743	3	-66.684	4	-44.056	5	-55.106	6	-52.634
7	-54.730	8	-59.912	9	-61.874	10	-62.846	11	-61.951
12	-60.373	14	-63.362	15	-42.382	16	-41.876	17	-39.463
18	-39.877	25	-51.278	26	-50.909	27	-50.859	28	-59.644
29	-60.854	30	-63.704	31	-60.920	32	-60.214	50	-17.498
60	-30.027	70	-12.884	80	5.420	81	6.093	82	3.854
115	15.159	116	14.652	117	9.232	118	9.620	1000	-273.111

CYCLE NO 5 THETA= 1.72000

N	TEMP (DEG CENT)							
2	-71.329	3	-66.227	4	-42.733	5	-55.353	6	-52.848
7	-54.980	8	-59.904	9	-61.282	10	-61.796	11	-61.332
12	-60.367	14	-63.704	15	-42.912	16	-42.947	17	-37.586
18	-38.802	25	-51.312	26	-51.028	27	-50.888	28	-59.595
29	-60.603	30	-62.873	31	-60.516	32	-60.144	50	-5.222
60	-21.618	70	0.017	80	21.056	81	24.304	82	20.206
115	15.139	116	14.643	117	9.276	118	9.655	1000	-273.111

CYCLE NO 5 THETA= 1.72100

N	TEMP (DEG CENT)							
2	-71.277	3	-66.220	4	-42.719	5	-55.356	6	-52.851
7	-54.983	8	-59.903	9	-61.274	10	-61.782	11	-61.324
12	-60.366	14	-63.707	15	-42.818	16	-42.961	17	-37.563
18	-38.789	25	-51.313	26	-51.031	27	-50.889	28	-59.594
29	-60.600	30	-62.861	31	-60.510	32	-60.143	50	-5.082
60	-21.518	70	0.161	80	21.234	81	24.503	82	20.390
115	15.138	116	14.642	117	9.276	118	9.655	1000	-273.111

TRANSIENT $\beta = 0, \phi = 0$

CYCLE NO 5 THETA= 0.00000 HOURS

N	TEMP (DEG CENT)							
2	-71.275	3	-56.185	4	-42.655	5	-55.266	6	-52.763
7	-54.893	8	-59.812	9	-61.181	10	-61.690	11	-61.234
12	-60.277	14	-63.560	15	-42.801	16	-42.945	17	-37.549
18	-38.767	25	-51.223	26	-50.945	27	-50.798	28	-59.504
29	-60.506	30	-62.770	31	-60.422	32	-60.055	50	-5.080
60	-21.516	70	0.163	80	21.192	81	24.501	82	20.391
115	15.190	116	14.689	117	9.322	118	9.700	1000	-273.111

CYCLE NO 5 THETA= 0.12000

N	TEMP (DEG CENT)							
2	-66.038	3	-55.489	4	-41.468	5	-55.524	6	-52.984
7	-55.170	8	-59.596	9	-60.191	10	-59.975	11	-60.211
12	-60.093	14	-63.556	15	-39.702	16	-41.190	17	-33.808
18	-35.242	25	-51.345	26	-51.227	27	-50.919	28	-59.297
29	-59.876	30	-61.193	31	-59.618	32	-59.876	50	10.716
60	-10.585	70	15.573	80	41.515	81	46.454	82	41.607
115	15.165	116	14.673	117	9.410	118	9.771	1000	-273.111

CYCLE NO 5 THETA= 0.24000

N	TEMP (DEG CENT)							
2	-62.369	3	-54.939	4	-41.070	5	-55.618	6	-53.070
7	-55.293	8	-59.176	9	-59.180	10	-58.377	11	-59.210
12	-59.752	14	-62.762	15	-36.021	16	-38.529	17	-30.850
18	-32.707	25	-51.391	26	-51.369	27	-50.976	28	-58.876
29	-58.954	30	-59.441	31	-58.605	32	-59.558	50	24.262
60	-1.653	70	27.587	80	59.114	81	64.270	82	60.099
115	15.165	116	14.670	117	9.535	118	9.876	1000	-273.111

CYCLE NO 5 THETA= 0.32000

N	TEMP (DEG CENT)							
2	-61.136	3	-54.821	4	-41.009	5	-55.527	6	-52.963
7	-55.233	8	-58.852	9	-58.739	10	-57.697	11	-58.785
12	-59.492	14	-61.823	15	-31.686	16	-34.344	17	-30.834
18	-33.098	25	-51.291	26	-51.235	27	-50.881	28	-58.498
29	-58.327	30	-58.524	31	-57.960	32	-59.264	50	31.791
60	3.620	70	34.627	80	67.735	81	72.231	82	68.875
115	15.188	116	14.687	117	9.630	118	9.956	1000	-273.111

CYCLE NO 5 THETA= 0.44000

N	TEMP (DEG CENT)							
2	-61.028	3	-55.153	4	-41.024	5	-55.112	6	-52.460
7	-54.882	8	-58.375	9	-58.577	10	-57.479	11	-58.654
12	-59.096	14	-59.854	15	-25.839	16	-28.734	17	-31.376
18	-34.083	25	-50.868	26	-50.587	27	-50.459	28	-57.848
29	-57.570	30	-57.833	31	-57.238	32	-58.724	50	40.911
60	10.860	70	44.347	80	75.934	81	78.950	82	76.689
115	15.270	116	14.758	117	9.773	118	10.072	1000	-273.111

CYCLE NO 5 THETA= 0.52000

N	TEMP (DEG CENT)							
2	-61.487	3	-55.478	4	-41.064	5	-54.599	6	-51.785
7	-54.406	8	-59.064	9	-58.704	10	-57.719	11	-58.798
12	-58.830	14	-58.490	15	-24.114	16	-27.428	17	-35.486
18	-37.045	25	-50.439	26	-43.864	27	-50.064	28	-57.444
29	-57.298	30	-57.836	31	-57.010	32	-58.374	50	44.397
60	15.015	70	48.770	80	78.137	81	80.037	82	78.448
115	15.352	116	14.829	117	9.859	118	10.141	1000	-273.111

CYCLE NO 5 THETA= 0.60000

N	TEMP (DEG CENT)							
2	-62.001	3	-55.683	4	-41.090	5	-53.871	6	-50.776
7	-53.703	8	-57.764	9	-58.975	10	-58.189	11	-59.077
12	-58.568	14	-57.367	15	-22.552	16	-26.261	17	-40.013
18	-40.328	25	-49.909	26	-48.899	27	-49.612	28	-57.123
29	-57.271	30	-58.203	31	-57.038	32	-58.086	50	45.213
60	18.501	70	50.775	80	77.723	81	78.491	82	77.547
115	15.445	116	14.909	117	9.919	118	10.192	1000	-273.111

CYCLE NO 5 THETA= 0.72000

N	TEMP (DEG CENT)							
2	-62.661	3	-55.774	4	-41.046	5	-52.516	6	-48.841
7	-52.377	8	-57.372	9	-59.588	10	-59.224	11	-59.693
12	-58.194	14	-56.183	15	-23.095	16	-26.280	17	-45.750
18	-44.395	25	-48.957	26	-47.106	27	-48.797	28	-56.785
29	-57.607	30	-59.265	31	-57.468	32	-57.756	50	43.346
60	21.628	70	50.756	80	74.669	81	74.182	82	73.852
115	15.601	116	15.041	117	9.962	118	10.234	1000	-273.111

CYCLE NO 5 THETA= 0.84000

N	TEMP (DEG CENT)							
2	-62.567	3	-55.577	4	-40.709	5	-51.128	6	-46.739
7	-50.982	8	-57.066	9	-60.192	10	-60.222	11	-60.296
12	-57.871	14	-55.873	15	-25.652	16	-27.430	17	-50.948
18	-48.182	25	-48.039	26	-45.221	27	-47.903	28	-56.616
29	-58.221	30	-60.484	31	-58.171	32	-57.580	50	39.358
60	19.266	70	47.769	80	71.519	81	70.376	82	70.245
115	15.741	116	15.168	117	9.962	118	10.242	1000	-273.111

CYCLE NO 5 THETA= 0.92000

N	TEMP (DEG CENT)							
2	-62.164	3	-55.276	4	-40.277	5	-50.240	6	-45.333
7	-50.054	8	-56.901	9	-60.598	10	-60.872	11	-60.700

MEAN TEMPERATURES FOR CYCLE NO ` 5

N	TEMP (DEG CENT)							
2	-68.408	3	-55.749	4	-42.596	5	-53.249	6	-49.867
7	-52.984	8	-58.352	9	-60.598	10	-60.802	11	-60.691
12	-59.011	14	-59.849	15	-39.442	16	-41.067	17	-47.798
18	-46.891	25	-49.903	26	-48.247	27	-49.585	28	-58.131
29	-59.307	30	-61.379	31	-59.269	32	-58.945	50	15.428
60	-4.096	70	20.759	80	45.222	81	44.933	82	44.330
115	15.434	116	14.897	117	9.615	118	9.947	1000	-273.111

Appendix C

THERMAL ANALYSIS DETAILS (DEWAR)

C.1 TANK DESIGN CALCULATIONS

BBRC has developed two programs which compute the temperatures of the actively cooled shields and the expulsion rate of fluid from the dewar. These programs are HEL2, which considers a dewar with two active shields, and HEL3, which considers a dewar with three active shields.

At present both programs assume that the active shields are isothermal and that the fluid passing over the shield attains shield temperature before leaving the shield. Both of these assumptions can be met by proper fabrication of the insulation system. A third assumption is that the supports are tied to the shields. If this is not desired, a slight reprogramming effort would be required.

The programs perform their computations by evaluating the temperature-dependent thermal conductivity integrals for the support material and the insulation, and making heat balances on the shields and the dewar. Neither HEL2 nor HEL3 computes the plumbing and wiring heat leaks; these are input as direct heat loads onto the shields and the dewar, along with the penetrations. A third program is going through the final stages of checkout which computes plumbing and wiring heat leaks as well, by evaluating the thermal conductivity integrals as a function of temperature, for the appropriate material. So far, stainless steel, titanium alloy, and OFHC copper routines are available. Others can be developed as required.

A heat balance on a typical shield is given by

$$Q_{in}, \text{ multi-layer} + Q_{in}, \text{ support} + Q_{net}, \text{ plumbing + wiring + penetrations} = Q_{out}, \text{ multi-layer} + Q_{out}, \text{ support} + Q \text{ picked up by helium}$$

where

$$Q_{in}, \text{ multi-layer} = aF_{h-s,m}(T_h^4 - T_s^4)$$

$$Q_{out}, \text{ multi-layer} = aF_{s-c,m}(T_s^4 - T_c^4)$$

Q_{net}, plumbing + wiring + penetrations = an input value from hand calculations

$$Q_{in}, \text{ support} = F_{h-s,sup}\left[c_1(T_h^4 - T_s^4) + c_2(T_h - T_s)\right]$$

$$Q_{out}, \text{ support} - F_{s-c,sup}\left[c_1(T_s^4 - T_c^4) + c_2(T_s - T_c)\right]$$

$$Q_{\text{picked up by helium}} = \dot{m}\left[c_3(T_s - T_c) + c_4(1/T_c - 1/T_s)\right]$$

using the following nomenclature:

a, c_1, c_2, c_3, c_4 = empirically determined constants

$F_{h-s,m}$ = area to thickness ratio of multi-layer insulation between the shield and the next warmer isothermal surface.

$F_{s-c,m}$ = area to thickness ratio of multi-layer insulation between the shield and the next cooler isothermal surface.

$F_{h-s,sup}$ = area to length ratio of support between shield and next cooler isothermal surface.

T_h = temperature of next warmer isothermal surface

T_s = temperature of shield

T_c = temperature of next cooler isothermal surface

$\dot{m}$ = fluid expulsion rate

The heat balance on the dewar is given by

$$Q_{in}, \text{ multi-layer} + Q_{in}, \text{ support} + Q_{in}, \text{ plumbing + wiring + penetrations} = \dot{m}\left(\frac{dQ}{dm}\right)$$

where (dQ/dm) is the thermodynamic expulsion parameter given by

$$\frac{dQ}{dm} = \Delta H_v\left(1 - \frac{x\rho v}{\rho L - \rho v}\right) \quad \text{for two-phase constant pressure expulsion}$$

where ΔH_v = heat of vaporization

ρv = density of saturated vapor

ρL = density of saturated liquid

x = mass ratio of liquid being expelled

(set x=0 for all vapor expulsion, x=1 for all liquid expulsion).

The method of solution is to solve for the shield temperatures and the expulsion rate simultaneously by the Newton method given initial guesses of these temperatures and the expulsion rate.

C.2 PENETRATION CALCULATIONS

At present, the temperature profiles of the multi-layer insulation and supports are calculated ignoring the radiation interchange caused by a support or fluid transfer line passing through a hole in the insulation. This radiation interchange is then calculated separately and the impact of this interchange on the previously calculated temperature profiles is evaluated.

Two computer programs have been developed for the calculation of the geometric view factors for the special geometries of cylinders and concentric cylinders. These two cases have been chosen because nearly all penetrations will be of one type or the other. The equations on which these programs are based were found in Radiation Heat Transfer for Space Vehicles by J. A. Stevenson and J. C. Grafton, North American Aviation report for Wright-Patterson AFB, ASD Technical Report 61-119, Part 1, December 1961, pp. 188-197. The programmed equations are:

A. For a cylinder of radius R and height H

$$B_{\text{end-end}} = A_{\text{end}} F_{\text{end-end}} = \frac{\pi}{2} R^2 \left[2 + \left(\frac{H}{R}\right)^2 - \frac{H}{R}\sqrt{4 + \left(\frac{H}{R}\right)^2} \right]$$

$$B_{\text{end-side}} = \pi R^2 - B_{\text{end-end}}$$

$$B_{\text{side-side}} = 2(\pi RH - B_{\text{end-side}})$$

All other B's are zero. Remember that $B_{ij} = B_{ji}$.

B. For two concentric cylinders the enclosure is formed by two discs (surfaces 1 and 4), the inside of the outer cylinder (surface 2), and the outside of the inner cylinder (surface 3).

Let the radius of the inner cylinder = r

Let the radius of the outer cylinder = R

Let the height of the two cylinders = H

Define the following parameters:

$$Y_1 = r/R \qquad X_1 = Y_2^2 + Y_1^2 - 1$$

$$Y_2 = H/R \qquad X_2 = Y_2^2 - Y_1^2 + 1$$

Then

$$B_{2-3} = 2\pi RH\left\{Y_1\left(1 - \frac{1}{\pi}\,\mathrm{Cos}^{-1}\,\frac{X_1}{X_2}\right) + \frac{1}{2\pi Y_2}\left[\sqrt{(X_1+2)^2 - 4Y_1^2}\;\mathrm{Cos}^{-1}\,\frac{Y_1X_1}{X_2} + X_1\mathrm{Sin}^{-1}\,Y_1 - \frac{\pi X_2}{2}\right]\right\}$$

$$B_{2-2} = 2\pi RH\left[1-Y_1 + \frac{2Y_1}{\pi}\,\mathrm{Tan}^{-1}\,\frac{2\sqrt{1-Y_1^2}}{Y_2} - \frac{\sqrt{4+Y_2^2}}{2\pi}\right.$$

$$\mathrm{Sin}^{-1}\,\frac{4(1-Y_1^2) + Y_2^2(1-2Y_1^2)}{4(1-Y_1^2) + Y_2^2} + \frac{Y_2}{2\pi}\,\mathrm{Sin}^{-1}\,(1-2Y_1^2) -$$

$$\left.\frac{1}{4}\left(\sqrt{4 + Y_2^2} - Y_2\right)\right]$$

$$B_{2-1} = B_{2-4} = \frac{1}{2}\,(2\pi RH - B_{2-3} - B_{2-2})$$

$$B_{3-1} = B_{3-4} = \frac{1}{2}(2\pi rH - B_{2-3})$$

$$B_{1-4} = \pi r^2 - B_{3-1} - B_{2-1}$$

All other B's are zero. Remember that $B_{ij} = B_{ji}$.

Should any more complex situations arise, BBRC has developed a program to calculate view factors for completely general geometries. This program is very long-running, so it is used only when necessary.

Once the geometrical view factors have been calculated, a second BBRC program calculates the reflecting view factors, also known as total radiation interchange factors. These account for both specular and diffuse reflections based on the emissivity and reflectivity of each surface. A discussion of this method may be found in "A Script-F Matrix Formulation for Enclosures With Arbitrary Surface Emission and Reflection Characteristics" by R. P. Bobco, ASME Paper No. 70-HT/SpT-3. For systems with diffusely reflecting surfaces only, the method may be summarized as follows:

1. Let $F_{ij} = B_{ij}/A_i$, ε_i = emissivity of surface i,

   ρ_i = reflectivity of surface i.

2. Form the transfer matrix, D, whose elements are given by:

$$D_{ij} = \delta_{ij} - \rho_i F_{ij}$$

where δ_{ij} is the Kronecker delta.

3. Invert the transfer matrix, obtaining the matrix β with elements β_{ij}.

4. Form the reflecting view factors, B^*_{ij}, given by

$$B^*_{ij} = A_i \varepsilon_i \varepsilon_i \Sigma_k F_{ik} \beta_{kj}$$

Now if any of the surfaces in the system has an unknown temperature, this temperature may be found by solving the equation or equations (one for each unknown temperature) $\Sigma_j B^*_{ij} (T_j^4 - T_i^4) = 0$. Once all of the temperatures have been evaluated, the net heat to a surface with a known temperature is given by

$$Q_i = \sigma \Sigma_j B^*_{ij} (T_j^4 - T_i^4)$$

where σ is the Stefan-Boltzmann constant. Q_i will be positive if the net heat load is incoming, negative if the net heat load is outgoing. The Q for all surfaces for which the temperatures were determined in the first part of this step will be zero.

Since the above analysis assumes each surface to be isothermal, it is important to use a realistic average temperature on any surface which actually varies in temperature from one end to the other. An example of this would be to use $T_{ave} = [\frac{1}{2}(T_a^4 + T_b^4)]^{1/4}$ rather than $T_{ave} = \frac{1}{2}(T_a + T_b)$ for the surface representing the cut edges of a stack of multi-layer insulation.

The most conservative approach is to neglect any net heat leaving either the insulation or the support, and to consider that any net heat entering the insulation or support is transmitted directly to the coldest surface, a shield or the dewar. In reality, this radiative interchange will merely distort the temperature profiles of the supports and of the insulation in the neighborhood of the penetration, but will not result in all of the heat being dumped on the coldest surface. Computer programs capable of handling nodal heat transfer calculations complete with temperature-varying thermal conductivities and fluid flow properties would be required to perform a rigorous thermal analysis of a dewar such as this one.

Appendix D

STRUCTURAL ANALYSIS OF CYLINDERS

D.1 COMPUTER PROGRAM FOR STRUCTURAL ANALYSIS OF SUPPORTS

This program was developed specifically for the analysis of fiberglass supports, and is capable of analyzing parts with anisotropic elastic properties. The finite element program uses three-node triangular elements. The program is presently capable of analyzing a structure with 600 degrees of freedom, permitting a very detailed representation of a support. Provisions are made to specify boundary conditions in any angular orientation. This enables an accurate representation of the spools in the ends of the supports. Specifically, in the spool area no motion is allowed normal to the spool surface while some degree of tangential motion is allowed. Frictional forces between the support and the spool can be accounted for.

The results of one study using the program are shown in Fig. B-1. The analysis was performed to determine the effects of the ratio of the spool radius to the band thickness upon the stress on the inner surface of the support (the stress on the inner surface is the maximum in the band). The results definitely show that small radius-thickness ratios are to be avoided.

D.2 STRESS ANALYSIS OF A CYLINDER-HEMISPHERE JUNCTION

This analysis is to develop equations for meridional and circumferential stresses at the junction of a cylinder and hemisphere. Loading is by a uniform hydrostatic pressure as shown in Fig. B-2.

The analysis uses the methods of NASA TR R-103*. This involves equating the edge deflections which are determined using the edge influence coefficients provided by the report.

---

*Johns, R. W. and Orange, T. W., "Theoretical Elastic Stress Distributions Arising from Discontinuities and Edge Loads in Several Shell Type Structures", NAS8-103, 1961.

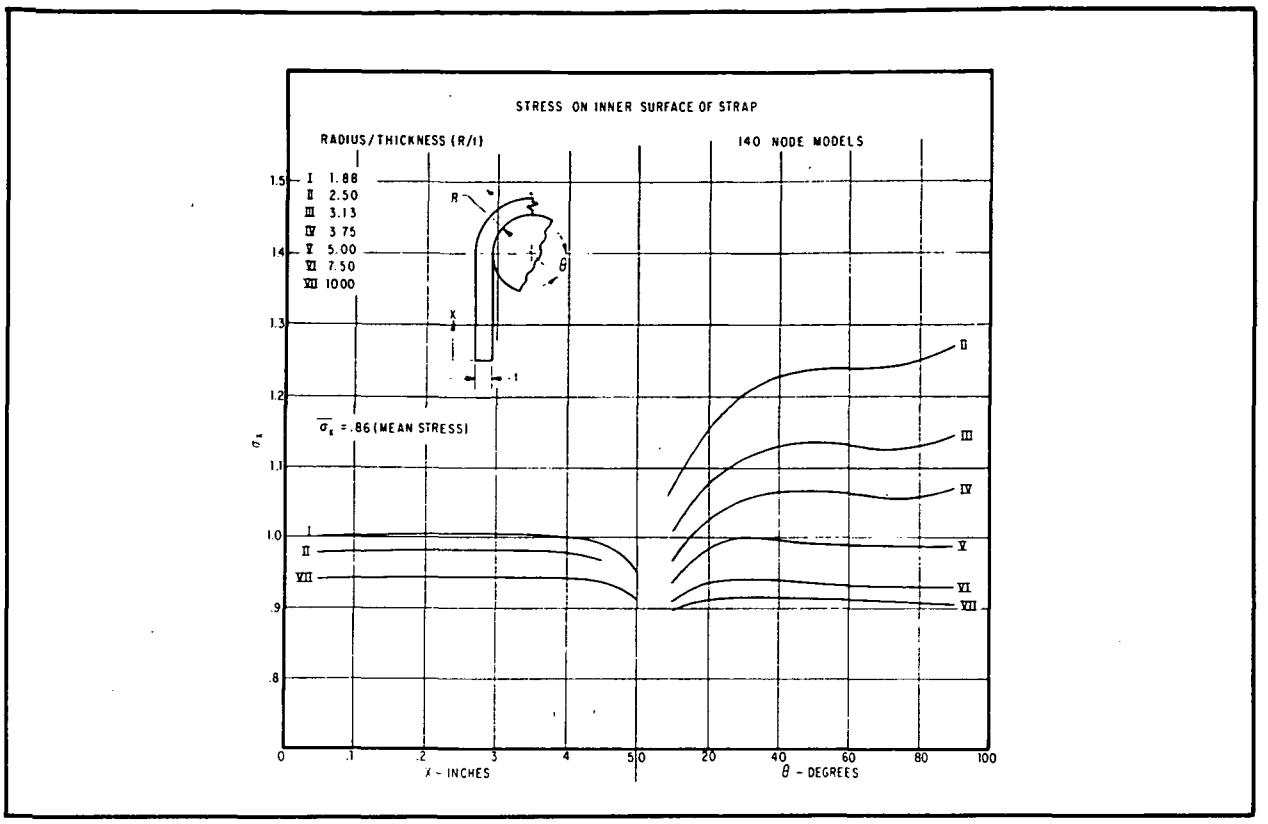


Fig. D-1 Stress on Inner Surface of Strap

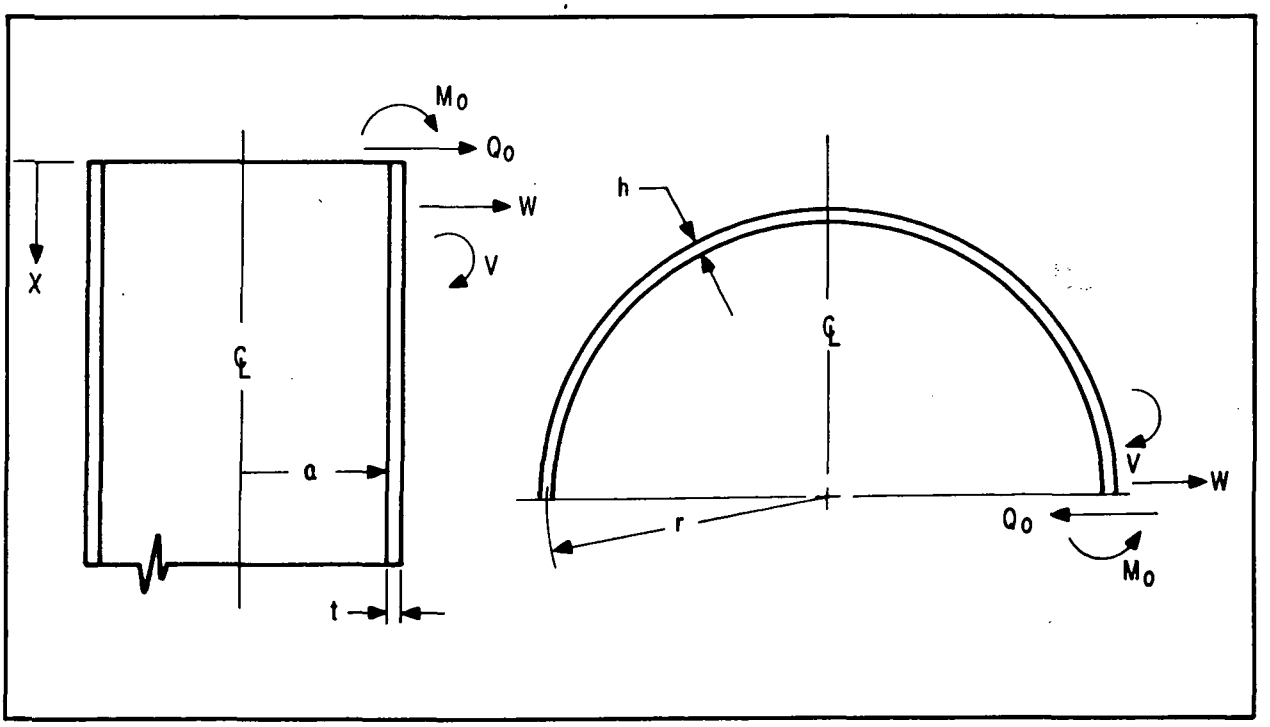


Fig. D-2 Cylinder - Hemisphere Junction Loading

The following symbols are used:

$D = \frac{Et^3}{12(1-\nu^2)}$

E = Elastic modulus

M_o = Edge moment

P = Hydrostatic pressure

Q_o = Edge shear

V = Meridional rotation

W = Deflection normal to center line

a = cylinder radius

h = sphere thickness

r = sphere radius

t = cylinder thickness

x = Distance from edge of cylinder

α = Angle from pole to sphere edge

$\beta = \left[\frac{3(1-\nu^2)}{a^2t^2}\right]^{1/4}$

$\lambda = \left[3(1-\nu^2)\ \frac{r^2}{h^2}\right]^{1/4}$

ν = Poisson's ratio

δ = Edge deflection influence coefficient

ω = Edge rotation influence coefficient

$\Phi(\ ) = e^{-(\ )}[\cos(\ ) + \sin(\ )]$

$\psi(\ ) = e^{-(\ )}[\cos(\ ) - \sin(\ )]$

$\Omega(\ ) = e^{-(\ )}\sin(\ )$

$\theta(\ ) = e^{-(\ )}\cos(\ )$

ψ = Angle from edge of sphere

$\sigma\psi$ = Meridional stress

$\sigma\theta$ = Circumferential stress

Edge influence coefficients per NASA TR R-103:

Sphere

$$\omega_{ms} = -\frac{4\lambda^3}{rEh} \; ; \; \omega_{qs} = \frac{2\lambda^2 \sin\alpha}{Eh} \; ; \; \omega_{ps} = o$$

$$\delta_{ms} = \frac{2\lambda^2 \sin\alpha}{Eh} \; ; \; \delta_{qs} = -\frac{2\lambda r \sin^2\alpha}{Eh} \; ; \; \delta_{ps} = \frac{r^2(1-\nu)\sin\alpha}{2Eh}$$

Cylinder

$$\omega_{mc} = \frac{1}{\beta D} \; ; \; \omega_{qc} = \frac{1}{2\beta^2 D} \; ; \; \omega_{pc} = o$$

$$\delta_{mc} = \frac{1}{2\beta^2 D} \; ; \; \delta_{qc} = \frac{1}{2\beta^3 D} \; ; \; \delta_{pc} = \frac{a^2(2-\nu)}{2Et}$$

Edge deflection and rotation:

Sphere

$$W_s = M_o\delta_{ms} + Q_o\delta_{qs} + P\delta_{ps}$$

$$V_s = M_o\omega_{ms} + Q_o\omega_{qs} + P\omega_{ps}$$

Cylinder

$$W_c = M_o\delta_{mc} + Q_o\delta_{qc} + P\delta_{pc}$$

$$V_c = M_o\omega_{mc} + Q_o\omega_{qc} + P\omega_{pc}$$

For compatible deformations at the edges of the two shells:

$$W_s = W_c$$

$$V_s = V_c$$

Thus providing two equations to solve for M_o and Q_o.

These values of M_o and Q_o are applied to the following equations of NASA TR R-103 to determine stresses.

Sphere

$$\sigma\psi = -\left[\frac{2\lambda}{rh}\cot(\alpha - \psi)\ \Omega(\lambda\psi) \pm \frac{6}{h^2}\Phi(\lambda\psi)\right]M_o$$

$$-\left[\frac{1}{h}\cot(\alpha - \psi)\ \psi(\lambda\psi) \pm\frac{6}{\lambda h^2}\Omega(\lambda\psi)\right]Q_o + \frac{Pr}{2h}$$

$$\sigma\theta = \left[\frac{2\lambda^2}{rh}\psi(\lambda\psi) \pm\frac{6\nu}{h^2}\Phi(\lambda\psi)\right]M_o - \left[\frac{2\lambda}{h}\theta(\lambda\psi) \pm\frac{6\nu r}{\lambda h^2}\Omega(\lambda\psi)\right]Q_o + \frac{Pr}{2h}$$

Cylinder

$$\sigma\psi = \pm\frac{6}{t^2}\left[M_o\Phi(\beta x) + \frac{1}{\beta}Q_o\Omega(\beta x)\right] + \frac{Pa}{2t}$$

$$\sigma\theta = \left[2\beta^2\frac{a}{t}\psi(\beta x) \pm\frac{6\nu}{t^2}\Phi(\beta x)\right]M_o + \left[2\beta\frac{a}{t}\theta(\beta x) \pm\frac{6\nu}{\beta t^2}\Omega(\beta x)\right]Q_o + \frac{Pa}{t}$$

In the above equations, the upper sign refers to stresses on the inner surface while the lower sign refers to stresses on the outer surface.

B.3 CALCULATIONS FOR APPROXIMATE SHELL THICKNESSES

The following calculations are a rough approximation to determine the order of shell thickness. The purpose of the calculations is to convey approximate shell thickness and to aid in obtaining weight estimates. They are not intended as an example of our analysis as used in a detailed design. The dimensions do not agree with those of the drawings, because it was considered unnecessary to work to even that degree of refinement at this time.

The loading on the shells is far more complicated than that of a uniform external pressure. Also, much higher strength can be obtained using stiffening of the shells. Such factors must be considered in the final analysis of the design.

Assuming an ultimate external pressure of 22.5 psi (1.5 x 15), head thickness for the inner tank is derived as follows:

A conservative equation for the critical external pressure of a sphere is:

$$P = 0.3E \frac{t^2}{R^2}$$

where

P = External pressure = 22.5 psi

E = Elastic modulus = 10×10^6 psi (aluminum)

t = Head thickness

R = Head radius = 70 in.

Rearranging the equation:

$$t = R\left[\frac{P}{0.3E}\right]^{1/2} = 70\left[\frac{22.5}{3 \times 10^6}\right]^{1/2}$$

$$t = 0.191 \text{ in.}$$

A cylinder thickness will be established using NACA TN-3783; "Handbook of Structural Stability, Part III, Buckling of Curved Plates and Shells," 1957.

Dimensions are:

L = Cylinder length = 35.5 in.

R = Cylinder radius = 21.0 in.

t = Cylinder thickness

Estimate t = 0.150 in.

$$100\,\frac{t}{R} = \frac{100 \times 0.150}{21} = 0.71$$

$$\left(\frac{L}{R}\right)^2 = \left(\frac{35.5}{21}\right)^2 = 2.86$$

$$\frac{5R}{t} = \frac{5 \times 21}{0.150} = 700$$

$$100\,\frac{t}{R} < \left(\frac{L}{R}\right)^2 < \frac{5R}{t}$$

This condition shows Eq. A11 to be applicable. This is:

$$F_{cr} = 0.93E\left(\frac{t}{R}\right)^{3/2}\left(\frac{R}{L}\right)$$

where

F_{cr} = Critical stress

with the assumed thickness of 0.150 in:

$$F_{cr} = 0.93 \times 10 \times 10^6 \times \left(\frac{0.150}{21}\right)^{3/2}\left(\frac{21}{35.5}\right)$$

$$F_{cr} = 3321 \text{ psi.}$$

The membrane hoop stress in the cylinder is:

$$f_c = \frac{PR}{t} = 15 \times 1.5 \times \frac{21}{0.150}$$

$$f_c = 3150 \text{ psi}$$

Since $F_{cr} > f_c$ the thickness of 0.150 in. is adequate for the cylinder.

For the outer shell:

Using the same equations as for the inner vessel with:

$$R = 73.0 \text{ in.}$$

$$t = R\left[\frac{P}{0.3E}\right]^{1/2} = 73.0\left[\frac{22.5}{3 \times 10^6}\right]^{1/2}$$

$$t = 0.200 \text{ in.}$$

For the cylinder:

$L = 33.5$ in.

$R = 25.8$ in.

Estimate $t = 0.170$ in.

$$F_{cr} = 0.93E\left(\frac{t}{R}\right)^{3/2}\left(\frac{R}{L}\right) = 0.93 \times 10^{7}\left(\frac{0.17}{25.8}\right)^{3/2}\left(\frac{25.8}{33.5}\right)$$

$$F_{cr} = 3831 \text{ psi}$$

$$f_c = \frac{PR}{t} = \frac{22.5 \times 25.8}{0.17}$$

$$f_c = 3415 \text{ psi}$$

Since $F_{cr} > f_c$ the thickness is adequate.

Appendix E

RELIABILITY PLAN

Appendix E
RELIABILITY PLAN

Reliability analysis concepts have been applied during the mission definition study to derive a reliability goal, make basic reliability assignments, and determine the need for redundancy and back ups.

These practices must be refined and extended during the formal reliability program for both the test flights and the main satellite. The refinements and extensions that we feel are necessary for the successful completion of this program are discussed here.

Table E-1 summarizes the reliability tasks for the test flights and the main flight.

E.1 RELIABILITY ENGINEERING

Reliability engineering involves the critical examination of hardware design for adequacy of operating margins, test verification, failure modes, parts application, and the reporting, analysis, and recommendation of methods for correction of failures. The activities and processes and their relationship to engineering, fabrication and test are shown in Fig. E-1 and described in the following paragraphs.

E.2 RELIABILITY ANALYSES

E.2.1 Reliability Allocation

A numerical probability within which a system is expected to operate for a specified period of time is derived based on the mission requirements of the system. The system reliability is apportioned to subsystems, and the results of the allocations provide a guide to the reliability design requirements of the subsystem.

Table E-1

RELIABILITY TASKS AND FUNCTIONS

Activity	Test Flights 1 and 2	Main Flight Program
Guidelines for Preparation of Reliability Plan	See below (consistent with plans used for rocket programs).	NHB 5300
Reliability Analysis		
Mission Reliability Tradeoff and Assignment	Based on test flight lifetime, portion of flt. proven equipment used, cost vs. est. rel. of new equipment.	Based on lifetime of expendables, test flt experience, cost vs. rel. of launch vehicle and satellites of similar complexity.
Reliability Allocation	For flight-proven hardware - based on flt. record or previous analysis - for new black-boxes, allocation compatible with achieving overall reliability requirement.	Allocation to subsystems based on inherent complexity, criticality, feasibility of providing redundancy and backups.
Reliability Predictions	Previous analysis for existing designs, parts count estimates for new, conventional subassemblies.	Parts count estimates for all subassemblies, special emphasis on non-conventional or state-of-the-art subassemblies.
Failure Mode and Effects Analysis	Development of back-up procedures to cover single point failures. Review of S/S interfaces for possible chain-reaction failure modes.	Single-point failure modes minimized by use of redundancy. Alternative opr. modes and contingency action for any single point failures.
Stress Analysis	By design engineer according to established derating guidelines.	Independent review of parts application to insure derating and interface compatibility over environmental range.
Parts Program		
Subassembly Qualification Status	Review of existing designs - qual. by previous testing, similarity of application or flt. exp.	Qual. by test flight exp., similarity, review qual. levels for new designs.

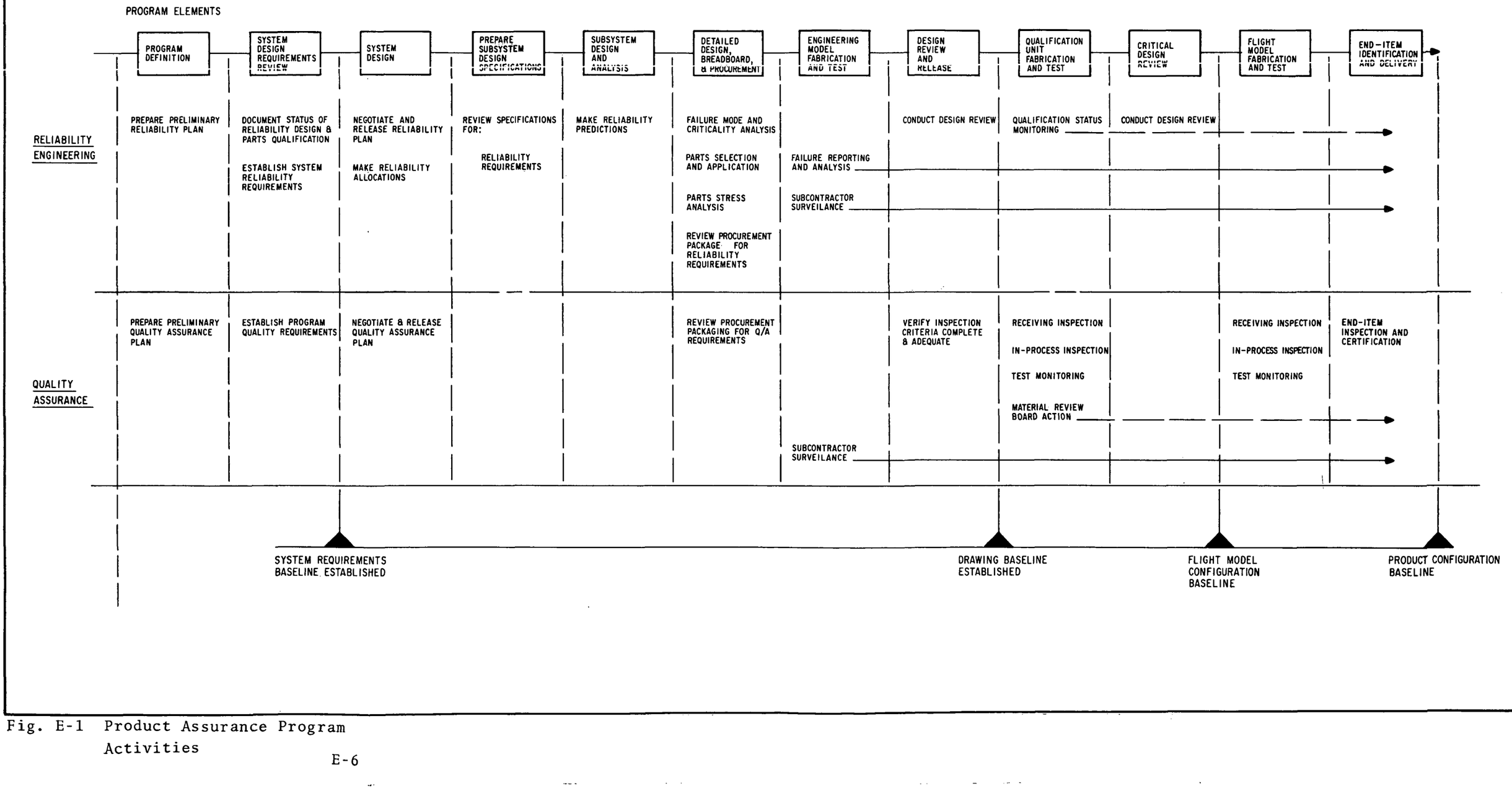


Fig. E-1 Product Assurance Program Activities

Table E-1 (Cont.)

Activity	Test Flights 1 and 2	Main Flight Program
Parts Specifications	Use existing specs. for conventional parts, create new specs for S.O.A. parts.	Same as for test flt. 1 and 2.
Parts Evaluation	During engineering development and qualification testing	State-of-the-art parts if characteristics are not well established or if stress margins are small.
Parts Lists, Materials, and Processes	Government and Contractor lists and specifications used where possible	Approved lists and specifications only, state-of-art components will require new documentation.
Malfunction Reporting and Failure Analysis	Informal for all equipment, starting with initial subassembly functional testing.	Formal reports and analysis for all proto and flt. equipment starting with subassembly functional tests.
Design Reviews	Informal design reviews during design phase to resolve difficulties.	Formal design reviews at concept stage, design release and completion of prototype testing.

E.2.2 Reliability Predictions

As the detail design evolves, reliability predictions are made using component failure rate data. Comparisons of alternative design approaches are made and the resulting effects on subsystem reliabilities calculated.

Such information is used in considering the need for redundancy, increased design emphasis, and the advisability of design changes. The finalized design is assessed against system reliability allocations. Reliability predictions are made from a part type-part count basis, assuming nominal operating environments and stress levels.

Designs are reviewed for the purpose of identifying parts or components which have a high failure history. Failure history is based on experience and industry data. Any item which has a high failure rate is identified and followed up to assure that corrective action is taken.

E.2.3 Failure Mode and Effect Analysis (FMEA) and Safety Hazard Analysis

This analysis identifies failure modes and the probability of occurrence for specific parts or subassemblies. Such information can be used by the designer to consider alternative designs that enhance the ultimate probability of success.

The initial FMEA will be conducted at the major subsystem level, and at interfaces between black boxes and external support equipment. Failure modes are evaluated for the conditions of premature operation, failure to operate at a prescribed time, failure to cease operating at a prescribed time, and failure during operation.

During conduct of the FMEA, program safety requirements are examined and safety hazards isolated. Hazards include damage to the satellite by test equipment as well as danger to personnel. Single point failures and catastrophic safety hazards are identified and measures developed which can be taken to preclude failure and accident occurrence.

E.2.4 Stress Analyses

Stress analyses are performed to assure that parts are used within prescribed limits, and that parts are derated for high reliability. Detail design will be done with the aid of derating factors such as those shown by Table E-2.

Calculations are made for the critical parameters for each component as it is used in the circuit. The calculated values are compared with the manufacturer's rated value to arrive at a stress ratio. This value is compared with the established derating guidelines. For stresses exceeding the guidelines, resolution is reached with the design engineer to either reduce the stress or justify the condition.

E.2.5 Parts and Components Qualification Status

Reliability engineering is responsible for monitoring system qualification testing to assure that performance is adequately appraised through test methods. Reliability consideration of tests performed are evaluated through review and approval of controlling specifications. Problems encountered during qualification testing are documented by the failure reporting and analysis system.

Table E-2
TYPICAL COMPONENT DERATING GUIDELINES

Part Type	Stress
Capacitors	$T_A \leq 80°C$ on all capacitors, subject to individual exceptions.
Solid Tantalum	Voltage less than 50 percent rated. Steady state reverse voltage shall not exceed 3 percent of the rated forward DC voltage. Transient reverse voltage shall not exceed 5 percent of the rated forward DC voltage. AC voltage - Peak AC plus DC must never exceed DC ratings as defined above. Negative AC peak plus DC not to exceed negative DC rating.
Integrated Circuits - Digital	Fan out not to exceed 80 percent of the specified rating.
Transistors Power	Power less than 30 percent of "no heat sink" rating. Voltage less than 80 percent rated across any junction. Rated voltage to be determined by safe operating curve. Current less than 80 percent rated. Rating to be determined by safe operating curve.

E.2.6 Part Evaluation

Evaluation tests are performed for parts on which there has been no evaluation experience or on parts for which a manufacturing process has been changed. Tests are performed on samples to observe parameters and parameter changes in selected environments.

The parts program involves part specification, application, evaluation, and control. To assure that reliable parts are used, the activities are employed as described in the following paragraphs.

E.2.7 Part Specifications

Part specifications identify critical parameters and test performance requirements. Parts required for a specific design are reviewed to determine whether an existing specification is adequate; if not, design specifications must be developed.

Specifications include MSFC, BBRC, JAN TX or MIL ER, MIL-STD, or AN, NAS Parts Specifications.

These specifications form the basis for parts screening tests such as those shown in Table E-3.

E.2.8 Program Parts List

A program parts list identifies all electronic, and electrical parts to be used. Parts appearing on one of the following preferred parts lists, MIL-established reliability (ER) parts and JAN TX parts, meet the intent of MSFC 85M03640 through their previous history of use in space applications.

Table E-3
TYPICAL PARTS SCREENING REQUIREMENTS

Connector	Dielectric strength, insulation resistance
Crystal	Frequency, aging
Diode	Forward voltage, reverse current, X-ray, power age
Resistor, Metal Film	DC resistance, X-ray, temperature cycle, power age
Resistor, Wirewound	DC resistance, burn-in
Transformer	Turns ratio, impedance, resistance, X-ray, high temperature storage, thermal shock
Transistor, FET	V_p, I_{DSS}, I_{GSS}, X-ray, channel test, power age
Transistor, NPN	h_{FE}, I_{CBO}, X-ray, power age
Transistor, PNP	h_{FE}, I_{CBO}, X-ray, channel test, power age
Wire	DC resistance, breakdown test, electrical leakage

MSFC 85M02716	Preferred Electrical Parts List for AAP
PPL-11	GSFC Preferred Parts List
TN69-47 (BBRC)	Preferred Parts Handbook for Space Systems
MIL-STD-1471A	Guided Missiles Preferred Items List, Mechanical and Materials.

Selection of parts not on the lists requires justification and evaluation tests and a data search to substantiate the suitability.

E.2.9 Material and Processes

A list of materials and processes to be used will be maintained as a section of the program parts and materials list. Typical entires from this list are shown in Table E-4.

All materials and processes are identified by applicable engineering design documents. The control of materials and processes is accomplished through the use of military, federal, BBRC, or other specifications.

Table E-4

PREFERRED MATERIALS AND PROCESSES

Material/Process	Specifications	Related Space Performance
Non-Metals		
Hexan Polycarbonate	BBRC	AAP (ATM)
Vespel Polyimide, Filled and Unfilled	BBRC	AAP (ATM)
Teflon	MIL-I-22129 MIL-P-22241	OSO, Ariel, Courier, Ranger
Zytel 101 Nylon	MIL-M-20693, Type 1 LP-410, Nylon 6/6	OSO, AAP (ATM)
Diallyl Phthallate	MIL-M-14 BBRC	OSO, AAP (ATM)
Epon 828, Versamid 125, Cured Epoxy. General Purpose, Unfilled and Cab-O-Sil Filled	BBRC	OSO, AAP (ATM), Syncom, Nimbus

E.3 MALFUNCTION REPORTING AND FAILURE ANALYSIS

Problems encountered during system development are monitored, analyzed, and documented. The resultant data determine the need for corrective action. Two documents are used to report problem areas: (1) reliability data reports (RDR) for minor discrepancies; and (2) failure reports that record the inability of a part of meet specification requirements.

Failure reporting will start with the first functional test of a Qualification model serialized subassembly and continue through the flight and flight spare equipment delivery. Failure analysis is required when the malfunction is attributed to a part or design failure or when the cause is not immediately apparent.

E.4 SUBCONTRACTOR SURVEILLANCE

Reliability engineering assures that components or subsystems developed by subcontractors are compatible with program reliability requirements. Depending upon the equipment type and criticality, this task may involve all aspects of the reliability program.

Visits to manufacturer's facilities provide familiarity with part construction and characteristics. Visits are not necessary except for state-of-the-art components or those components involving critical processes or special problems.

E.5 DESIGN REVIEWS

Three formal system reviews are scheduled: (1) a concept design review near the beginning of the program, (2) a preliminary design review (PDR) after detail design, and (3) a critical design review (CDR) at completion of qualification testing. Informal reviews are held as required for resolution of problems.

Topics to be discussed at the design review may include the following items, supported by informal documentation:

- Functional description of equipment operation
- System analysis, such as block diagrams, error budgets, power requirements
- Identification of known problem areas
- Method of implementing quality and reliability
- Compliance with design requirements

Design Review by Suppliers. Design reviews will be conducted on subcontracted items commensurate with the type of equipment and its end use. Design reviews provide a formalized approach to design definition. These reviews may involve representatives from the customer, project, design, materials specialists, reliability, quality assurance, production, and other specialists as required.

Appendix F

QUALITY ASSURANCE PLAN

Appendix F
QUALITY ASSURANCE PLAN

F.1 INTRODUCTION

The Quality Assurance program we recommend for this mission satisfies the applicable requirements of quality specification NHB 5300 "Quality Program Provisions for Aeronautical and Space System Contractors". The program is designed to assure that the quality of the deliverable article is in accordance with contract and mission requirements.

The requirements of NHB 5300 also apply to subcontracts for major purchased items.

The Quality Assurance tasks for the test flights and the main flight are given in Table F-1. The text gives details of each activity. Note that this text tells what should be done when full compliance is recommended. For the test flights more limited effort will be done as indicated in the table. The efforts of Quality Assurance will (1) support the Reliability Program, (2) verify the supplier's conformance with Reliability Assurance provisions, (3) assure that Reliability engineers participate in the disposition of major and end item test failures, (4) review Malfunction Reports for corrective actions and pursue those to completion where Quality Assurance actions will be affected, (5) consult with Reliability on questionable test requirements or conditions. The relationship of Quality Assurance activities to engineering and fabrication processes is shown in Fig. E-2.

Table F-1

QUALITY ASSURANCE TASKS

	Test Flights 1 and 2	Main Flight
Design Reviews	Informal Participation by quality engineering during design reviews.	Participation in formal design reviews.
Material Review Board	Quality engineering represented on board.	Quality engineering represented on board.
Procurement Surveillance Source Inspection	Government Source Inspection (GSI), if required.	Review of procurement requirements for compliance with QA requirements. In-process surveillance of critical assemblies. GSI where possible.
Receiving Inspection	Standard components inspected according to established procedures. State-of-art components inspected in laboratory.	Formal incoming inspection procedures for all components.
In-Process Inspection	100 percent inspection of critical characteristics (mechanical parts). Audit inspection of non-critical characteristics. 100 percent of electrical assemblies for soldering.	Same as for Flight 1 and 2 except electrical assemblies inspected to NHB 5300.
In-Process Testing	Initiation of non-conformance reports.	QA monitoring of environmental and acceptance testing. Certification of acceptance and environmental test results. Initiation of non-conformance reports.
Final Inspection and Acceptance Testing	Preshipment visual inspection.	Continuous monitoring. Final visual inspection.
Control of Non-Conforming Material	Informal review of discrepant items by board consisting of QA, Reliability and engineering.	Formal review of discrepant items by Material Review Board.

F.2 BASIC REQUIREMENTS

The Quality Assurance program is organized and performed in coordination with the prime contractor's other organizations including Engineering, Production, Purchasing, and Project. The program is preventive in nature by enabling early detection and correction of deficiencies. Objective evidence is maintained of all quality operations and is available for customer review.

F.2.1 Inspection Plan

A typical flow chart illustrating the inspection and test operations is shown in Fig. F-1.

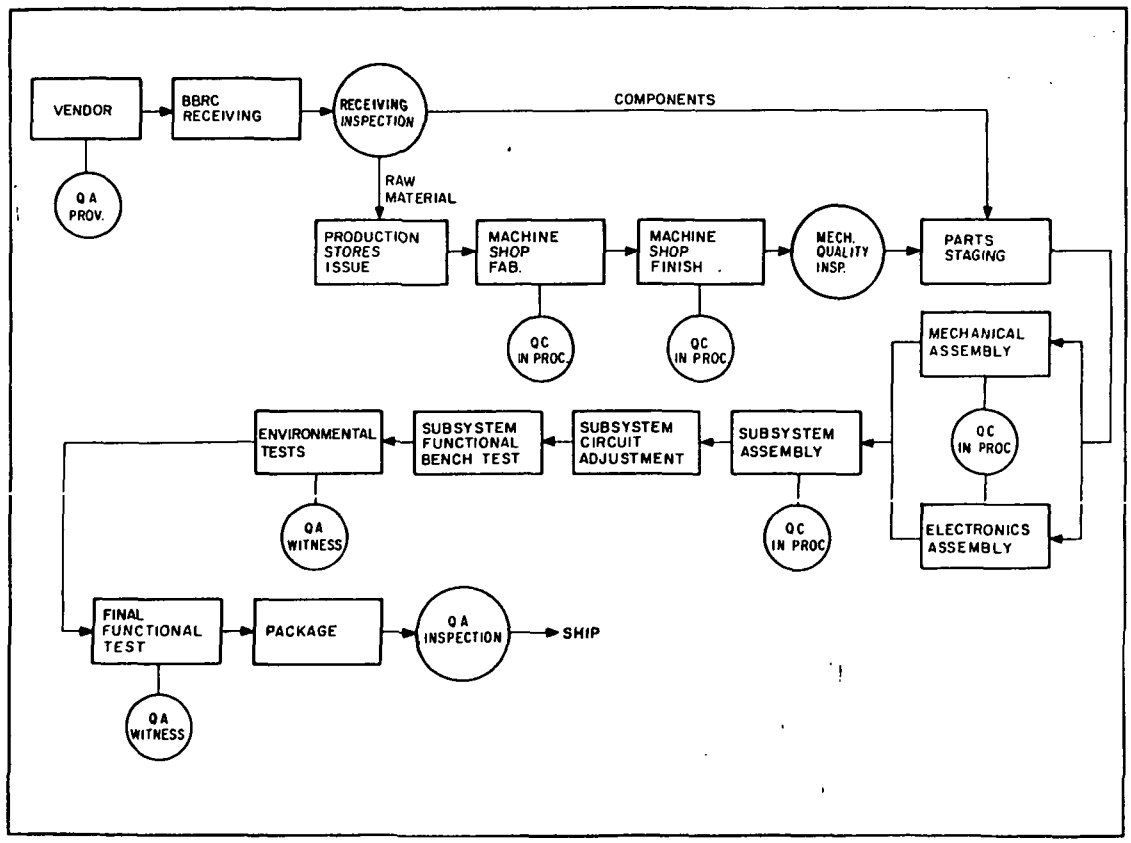


Fig. F-1 Product Flow Chart and Inspection/Test Stations

F.2.2 Change Control

During manufacture and test, all drawing deviations and changes other than substitutions will be recorded by issuing a liaision engineer action (LEA). Substitutions are allowed when called out on a substitutions list (released drawing) and require design approval. Quality Assurance ensures that the necessary LEA's and any substitutions are accomplished and so evidenced on the inspection records of the part, component, or assembly.

F.3 DETAILED INSPECTION REQUIREMENTS

F.3.1 Purchased Materials Control

Procedures must establish controls of procured materials, supplies, and services. The Quality Assurance Provisions (QAP's), Reliability Assurance Provisions (RAP's) and inspection codes are specified on purchase orders.

Inspection is accomplished in accordance with pre-planned inspection instructions, engineering drawings, and specifications. The instructions identify the characteristics to be inspected, the method/equipment to be used, and the information to be recorded.

Receiving inspection of materials, parts, and components is as follows:

- Hardware components such as AN, NAS, and MS nuts, bolts, screws, washers will be sample inspected in accordance with MIL-STD-105D.

- Mechanical piece parts will receive 100 percent inspection of critical characteristics. Non-critical characteristics will be inspected only as required to determine conformance to applicable drawings and specifications.

- Other components will be inspected according to their drawing requirements.

- Electronic piece parts will be inspected and tested in accordance with a test specification for electronic parts.

F.3.2 Government Source Inspection (GSI)

GSI does not relieve the contractor from his responsibility of meeting hardware quality and reliability requirements. GSI will only be applied to purchase orders when so directed by the authorized Government representatives.

F.3.3 Identification, Handling and Storage of Material

Purchased materials, parts, components, and assemblies will be identified at receiving inspection with a materials identification tag (MIT), identifying part number and/or applicable specification number, including revision letter, purchase order number, and bearing the inspector's acceptance stamp. The MIT accompanies the material and becomes part of the historical record. Limited life materials are identified with the expiration date, cure date or date of manufacture.

F.3.4 Raw Materials Control

Receiving inspection obtains chemical and/or physical tests on raw material to be used in applications where material strength, temperature characteristics and/or outgassing is critical. The materials are stored in a controlled access storeroom. Stock issue tags referencing the proper MIT are used and included as part of the assembly historical records.

F.3.5 Inspection and Tests

F.3.5.1 In-process Inspection

In-process inspections are performed by quality inspection personnel at designated inspection stations during fabrication and assembly sequences. In-process inspections are as follows:

- Machined articles are inspected 100 percent for critical characteristics. Non-critical characteristics are audit inspected (approximately 15 percent). The application of auditing is based upon the qualification of the individual machinist and his performance subsequent to qualification.

- Electrical assemblies are soldered in accordance with the requirements of NASA Quality Publication NHB 5300.4(3A), "Requirements for Soldered Electrical Connections" except for negotiated deviations. Electrical assemblies are 100 percent inspected in accordance with the requirements of NHB 5300.4(3A). Electronic welding is controlled by testing of weld samples in addition to visual verifications that all weld straps are present. Parts placement and component orientations are also verified by inspection.

F.3.5.2 In-process Test

In-process tests (bench tests) are performed to verify compliance with functional requirements. Test results and any malfunctions are documented on the test record form and included in the appropriate system log book.

F.3.5.3 Final Inspection and Test

Final acceptance inspection of the completed subsystem verifies compliance to applicable nonfunctional characteristics, and is documented in the system log book.

Quality personnel witness the environmental and final functional tests of each flight system to assure compliance with the applicable test procedures. Results of these tests are documented in the system test record and become part of the system log book.

F.3.6 Process Controls

A defect prevention program is maintained for the control of bonding, coating, plating, material cleaning, and other processes where standard inspection procedures and techniques alone are not adequate to assure a quality product.

Special processes are monitored and controlled for uniformity and accuracy and corrective action taken upon process rejections. Daily process testing procedures and records determine and verify the adequacy of surface finish process solutions. Radiography will be performed by trained, certified, and experienced Quality Assurance personnel. Solderers, module welders, and inspecting personnel are formally trained and certified.

F.3.7 Control of Nonconforming Material

Nonconformances found during manufacturing, assembly, inspection, or test operations are documented on a quality action item list and reviewed as follows:

- Preliminary Material Review

  Nonconformances noted during receiving inspection: Preliminary dispositions of Return to Purchasing, Scrap, Complete to Drawing (Rework to Drawing), or Refer to Material Review Board (MRB) are made by the Inspection Supervisor after coordination with the requisitioner and procurement representative.

  Preliminary disposition of nonconformances on BBRC fabricated/assembled hardware prior to the end-item assembly level: Preliminary disposition of complete to Drawing, Scrap, Refer to Initial MRB or Trouble-shoot are made by the Inspection Supervisor after coordination with the production supervisor and, if appropriate, the design engineer.

  Nonconformances noted on the End Item Assembly prior to start of acceptance testing: Preliminary disposition to Complete to Drawing, Scrap, Investigate, or Refer to Initial MRB is made by the project QA engineer after coordinating with the design and project engineer.

- Initial Material Review

  Initial Material Review Board actions may be any of the following:

  a. "Use as is" or "repair" if the nonconformance will not detrimentally affect assembly, performance, safety or reliability; is not an end-item acceptance test failure; nor is the article GFE.

  b. "Investigate" (troubleshoot) to determine the cause and extent of the nonconformance.

  c. "Continue Testing" if the nonconformance is not hazardous to subsequent testing and continued testing is of advantage to the program.

  d. "Scrap" may be made by any MRB member without unanimous concurrence.

  e. "Refer to Final MRB"

- Final Material Review

  Final Material Review Board is required on all nonconformances which:

  a. May detrimentally affect the end item safety, reliability, performance, interchangeability, weight or other basic requirements of the contract.

  b. Are on GFE.

These nonconformances will be documented on Material Discrepancy Reports (MDR's) and may be dispositioned Use As Is, Repair, Scrap, or other appropriate recommendations. These dispositions are recommendations which are to be submitted (via telephone, telex or letter) to the designated Technical Officer for final disposition.

Rejected items at all levels shall be positively identified and if practical shall be segregated in a Material Review area.

F.3.8 Inspection, Measuring and Test Equipment

The metrology laboratory calibrates mechanical inspection tools against certified standards traceable to national standards. Electrical test equipment is similarly calibrated by the standards laboratory.

F.3.9 Preservation, Packing and Shipping

The Quality Assurance Department is responsible for performing a final inspection of each deliverable item before it is shipped to verify that it is complete, packed, packaged, and identified in accordance with applicable requirements, and that all required shipping and technical documents are included with the shipment.

Appendix G

CONTROL SYSTEM SIMULATION AND ANALYSIS

CONTROL SYSTEM SIMULATION AND ANALYSIS

G.1 INTRODUCTION AND SUMMARY

Control system analysis was performed at three levels during the mission definition study. Simplified single-rigid-body analysis was conducted for each of the control loops to roughly establish their required characteristics. These analyses are described in Section 6 of the main text. The pitch-yaw loop was assumed to be a single stage controller (i.e., without the quartz block gimbals) which only uses the helium thrusters for control torques. Simplified analyses were also applied to the roll axis, each of the translation axes, and to the gyro suspension controllers. The calculations, based on the simplified analyzes, are for the normal operating modes of each controller.

In the second level of analysis root-locus and frequency response (BODE) plots were generated using digital computer programs. These "classical" control system design tools were used to substantiate the conclusions of the simplified analyses and to attempt to compare the performance of a simple second-order lead-lag-lag pitch-yaw controller with the two stage modern controller designed by Stanford.

In the third level of analysis, analog computer simulations were conducted to demonstrate the performance of Stanford's modern two-stage pitch-yaw controller. The computer simulation is described in Section G.3 and the results of the simulation are given in Section G.4. The results include the system response to white noise, to initial conditions, step responses to external and interbody torques and to commanded offsets, the effects of

variation of the interbody vibration frequencies, and the effects of variation of each of the estimator and controller gains.

The analysis during the mission definition study was concentrated on the normal fine pointing operations. The pitch-yaw simulations are for stellar daytime operation. Perfect mechanization was assumed in controller components except that a brief look was taken at the effect of the flattening of the telescope response for errors larger than about 0.5 arc-second.

The analysis of a number of control modes was limited to crude calculations. More careful analysis should be initiated as soon as possible in the program. The stellar night-time pitch-yaw pointing loop should be designed and its performance verified by analog computer simulation. As currently envisioned, this design only involves the modification of several of the daytime controller-estimator gains.

Simulations should also be performed to verify that night-to-day transitions can be made smoothly by simply switching the controller gains. The simulations already conducted show that the nonlinearity in the telescope output will prevent guide star acquisition (using the normal daytime gains) for initial errors as large 10 arc-seconds. Coarse acquisition by the telescope may require an additional set of controller-estimator gains, it may require that the telescope signal be used for position error while the gyroscope signals are used for rate information, and it may be preferable to use a separate controller and filter. Further analysis and computer simulation should be performed to arrive at a satisfactory design.

Analysis and simulation work should also be started in the near future to verify that the initial acquisitions sequence works properly. The roll axis, translation, and gyro suspension controllers should be simulated and a multi-axis simulation should be performed to show that the loops work well together. Finally, analysis should be performed to arrive at allowable hardware mechanization errors in each of the control loops.

Important conclusions of the analysis already completed are:

- The gyro acceleration requirements makes jitter acceleration (and not just position) important. This makes the noise attenuation problem more difficult as described in Section G.2.

- It is important to place the satellite mechanical vibration frequencies as high as possible.

- The system response of the modern controller-estimator is insensitive to variation of many of its gains but is quite sensitive to variations which cause errors in the estimator's model of the plant. Parameters which must be accurately placed (±20 to ±30 percent) are the quartz block vibration frequency in its gimbal, four of the estimator gains and the control torquer gains.

- A simple single-state controller may be adequate for pitch-yaw control (see Section 6).

- The tightest controller design problem appears to be that of the gyro suspensions.

G.2 ROOT-LOCUS AND FREQUENCY RESPONSE PLOTS

The fundamental design problem in each of the SRS controller loops is that of providing a bandwidth high enough to meet the DC gain and transient settling time requirements and at the same time low enough for adequate attenuation of sensor noise. This is a common servo design problem; however, it is usually sufficient to adequately attenuate the position jitter caused by sensor noise. The SRS gyro acceleration requirements make it necessary to attenuate acceleration jitter as well. This makes the noise attenuation problem significantly more difficult.

For design purposes we have assumed that the sensor noise is white noise, band-limited in some bandwidth. Lightly damped mechanical vibration modes produce response spikes which must also be attenuated sufficiently. A linear second-order controller with position feedback and lead-lag compensation does not provide sufficient noise attenuation for the SRS control loops, because the acceleration response to sensor noise does not fall off for frequencies above the lag break frequency. Such a controller would probably be adequate for position jitter attenuation because the position response has a -2 slope above the lag break. A double lag is required to attenuate the acceleration caused by sensor noise.

Linear second-order controllers with position feedback and lead-lag-lag controllers are described which meet the requirements for each of the SRS control loops. The simple controllers for the roll and translation loops easily meet the system requirements. The simple one-stage pitch-yaw controller has rather modest DC gain and sensor noise attenuation margins and depends on excellent performance from the helium thrusters. The performance margins of the simple pitch-yaw controller could be substantially increased by integral feedback (because the transient settling time of the described system is substantially faster than required).

Rapid settling times are required in the gyro suspensions to help attenuate the first overshoot in the transient response following a meteoroid impact. Also, the suspension bandwidth must be higher than the other control loop bandwidths to reliably support the gyro rotors during control activity in the other loops. The required high bandwidth and damping makes the suspension noise response high. The gyro position sensor noise must be less than 1/10th as large the best current estimate for the existing high voltage suspension to meet the gyro acceleration requirement. The gyro suspension appears to be the tightest SRS controller design problem at this time.

Most of the analysis during the mission definition study was applied to the pitch-yaw control loop. Root-locus and frequency-response plots were made for the single-stage controller to decide where the lead and lag breaks should be placed to get adequate sensor noise attenuation, and at the same time, reasonable gain and phase margins. These plots were also made for the two-stage controller and for the last set of gains supplied by Stanford. For properly chosen gain and lead and lag break points the single stage system response near the unity cross-over was

found to be comparable to that of the Stanford design. The low frequency performance of the Stanford system is substantially different from that of the single stage controller because the former has integral error feedback while the latter does not. It is probably desirable to add integral error feedback to the single-stage system. This was not done during the mission definition study because time was not available to weigh the advantages and disadvantages.

Figure G-1 gives the frequency response characteristic of the modern two-stage pitch-yaw controller for the last set of gains supplied by Stanford. Four curves are plotted. The amplitude ratio of the open-loop transfer function between error angle and sensor noise is labeled open-loop θ/w. The open-loop phase is plotted as a dash line. The open-loop curves are not plotted for low frequencies because of difficulties in reading a Nichols chart to transform from closed to open-loop characteristics. The closed-loop position responses from sensor noise to position error and to acceleration error are labeled θ/w and $\ddot{\theta}/w$, respectively. The slight rise in the position response of the system near 0.4 rad/sec occurs at the dominant control frequency of the outer control loop. The more pronounced rise near 2.5 rad/sec is at the dominant frequency of the inner control loop. The shape of the position response peak suggests that the damping is good. This is substantiated by the 32° phase margins and the fact that the open-loop unity cross-over is well centered with respect to the open-loop phase curve. The system's gain margin of 11 dB is probably acceptable.

Figure G-2 gives the frequency response of a simple one-stage system with an open-loop unity crossover point equal to that of of the modern system. The simple system's open-loop resonant

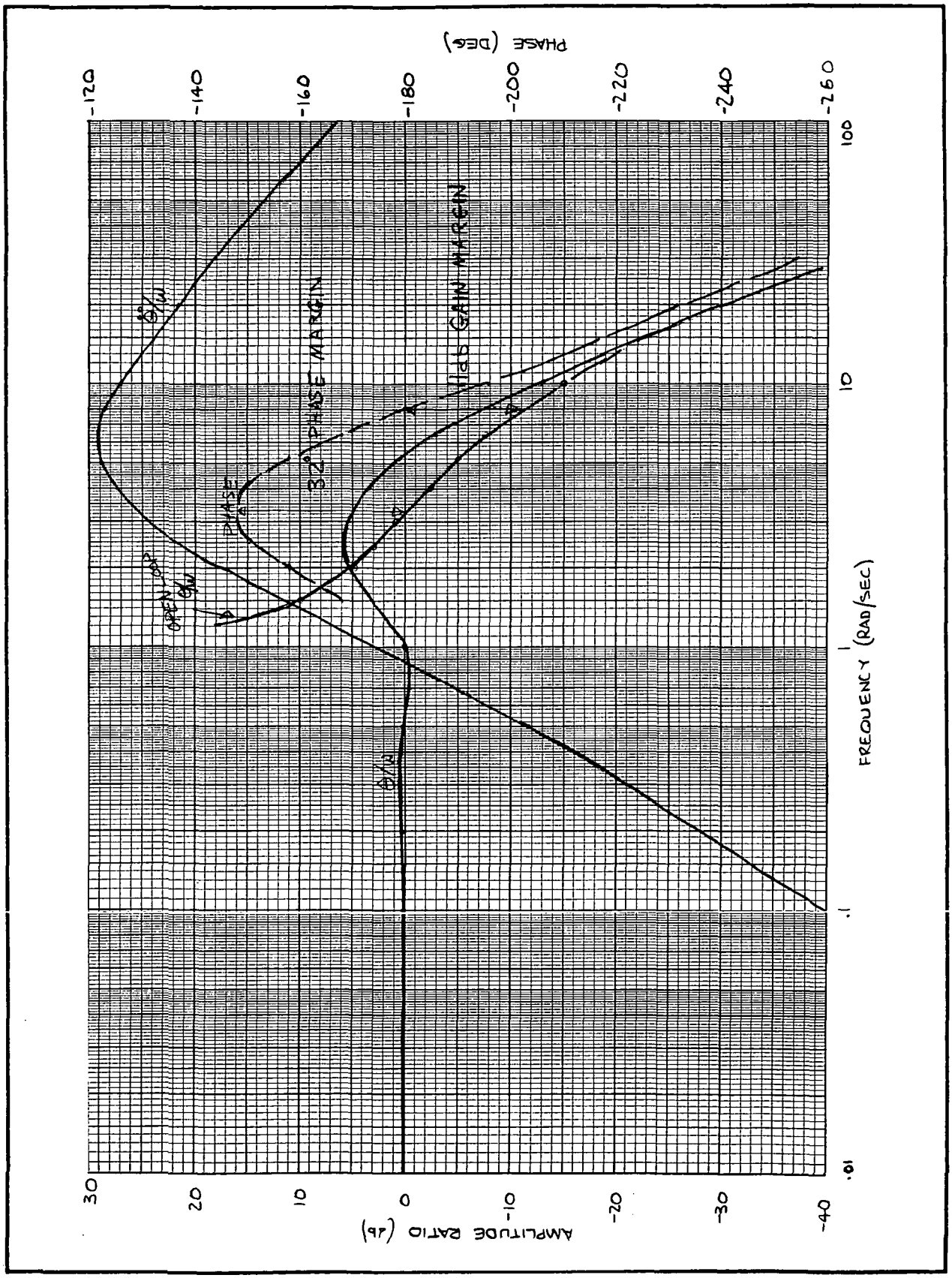


Fig. G-1 Frequency Response of the Modern Two-Stage Pitch-Yaw System

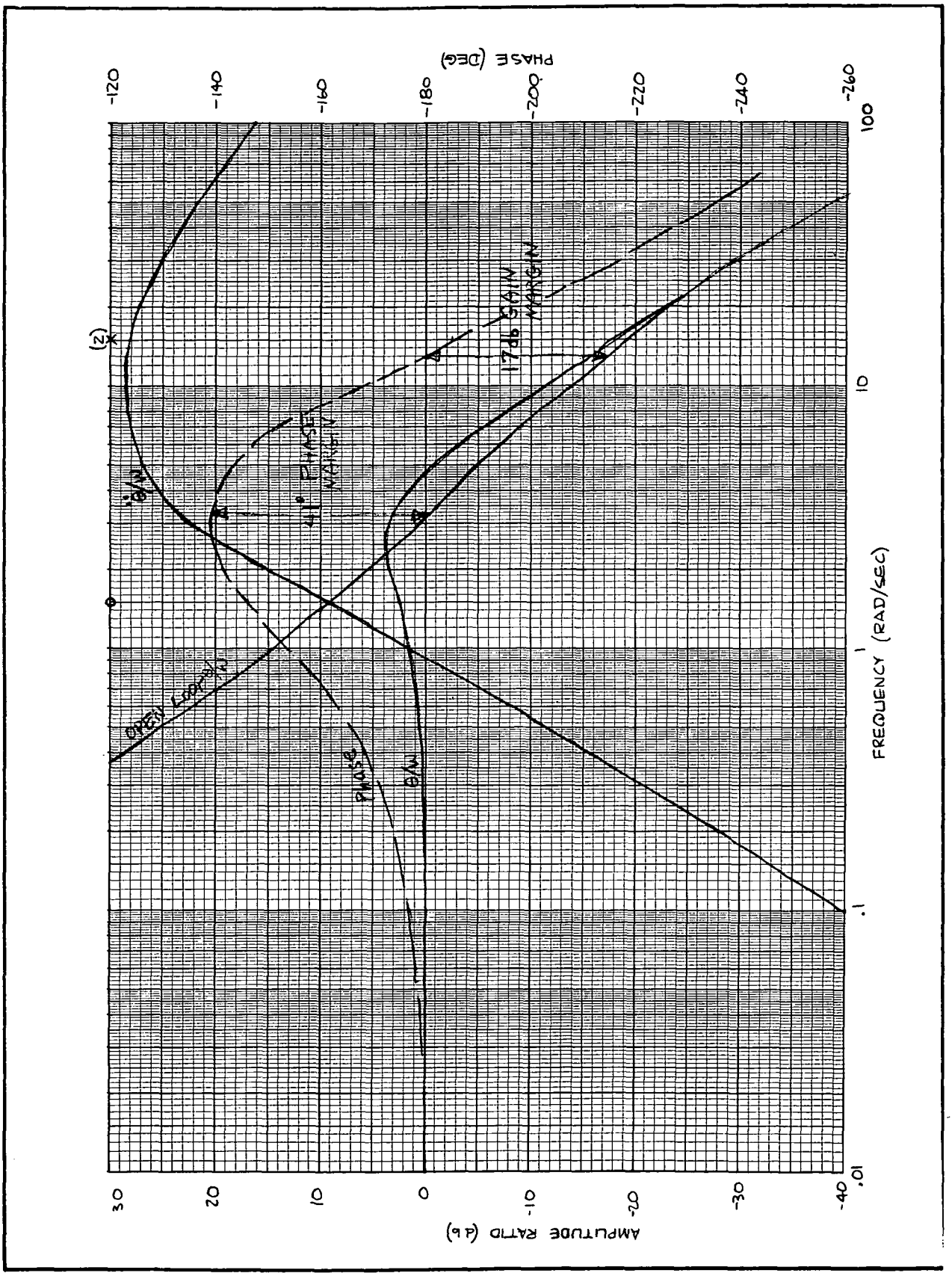


Fig. G-2 Frequency Response of One-Stage System with $\sqrt{K/I}$ = 2.1 rad/sec, Lead at 1.5, Lags at 15 rad/sec

frequency is at 2.1 rad/sec, and the lead and lag-lag breaks in its compensation are at 1.5 and 15 rad/sec respectively. This simple system has better damping (as indicated by its 41° phase margin), and a higher gain margin than does the modern system. Furthermore, its jitter amplitude sensitivity to sensor noise is lower than for the modern system. However, its jitter acceleration sensitivity to sensor noise greater than the modern system. The closed-loop acceleration response of the modern system peaks at about 6 rad/sec and is falling off at a -1 slope by 10 rad/sec. The simple system's acceleration response peaks at about the same amplitude but the peak is at 10 rad/sec and the -1 slope is not reached until about 25 rad/sec. Therefore, this version of the simple system has a substantially higher "acceleration noise bandwidth" than does the modern system.

In the interest of reducing the acceleration bandwidth of the simple system the double-lag was pulled back from 15 to 7.5 rad/sec. The effect of this modification is shown in Fig. G-3. This modification had the desired effect in that the acceleration response peak is pulled back to about 3 rad/sec and the -1 slope is achieved soon after the peak. As is widely known, earlier interruption of the lead degrades damping. The degradation is substantiated by the factor of roughly 2 reduction in phase margin. This modification also substantially reduces the system gain margin from 17 to 9.4 dB. It is interesting to note that this modification made the simple system amplitude sensitivity to noise substantially worse while it made its acceleration sensitivity to noise substantially better. This shows that the amplitude response characteristics cannot be relied upon, although this is common practice, in the design of a low acceleration jitter controller.

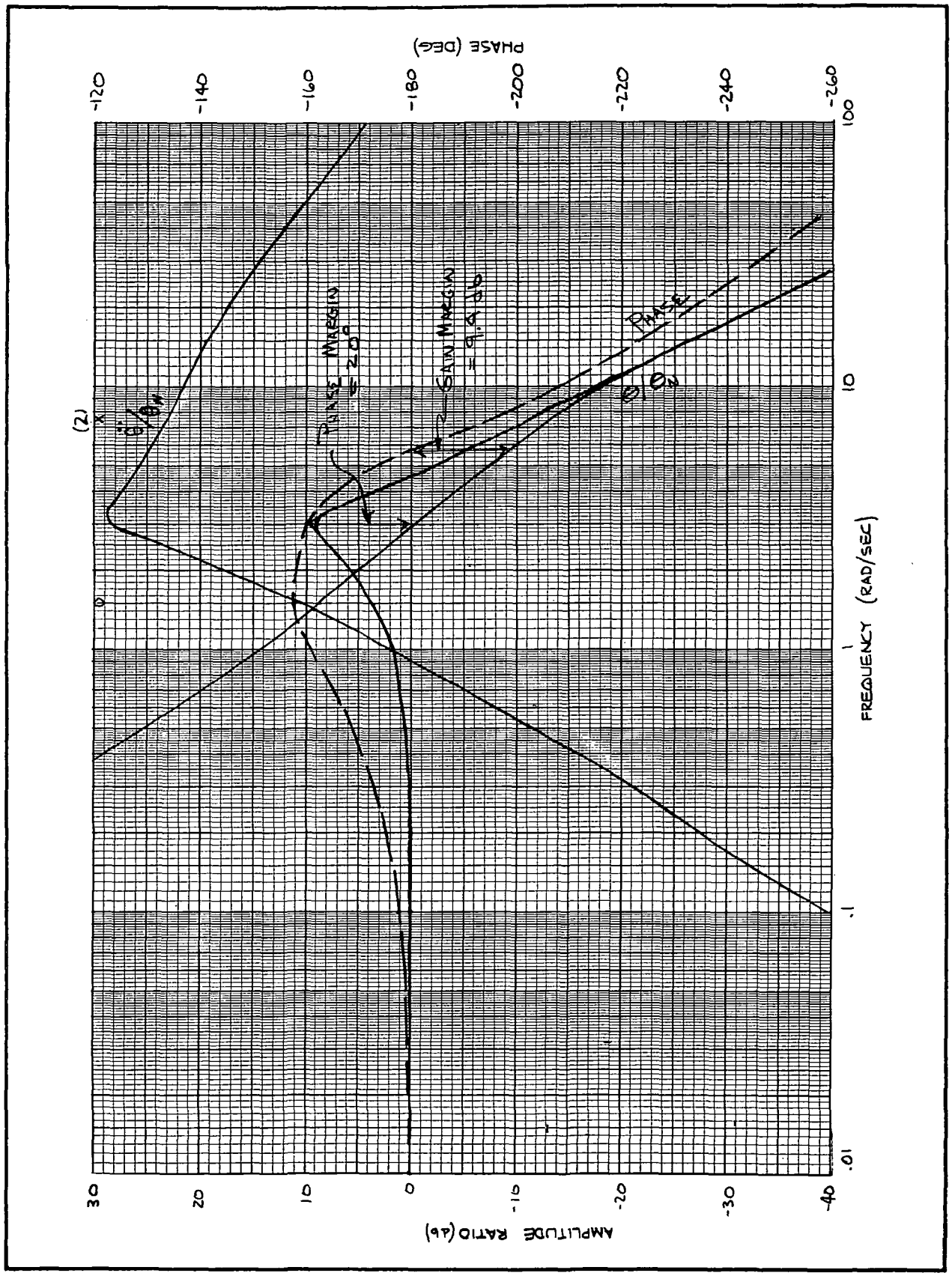


Fig. G-3 Frequency Response of One Stage System with $\sqrt{K/I}$ = 2.1, Lead at 1.5, Lags at 7.5 rad/sec

Comparing Figures G-1, G-2, and G-3 we see that the damping, phase margin, gain margin, amplitude noise sensitivity, and acceleration noise sensitivity of the two simple systems brackets the performance of the modern system. The three dB bandwidths of the three systems are equal. Their low frequency responses (not plotted in Fig. G-1) would differ little, if integral control was added in the simple systems.

Another important factor, for a system whose jitter acceleration sensitivity to noise is important, is the effect of lightly damped high frequency plant vibration modes. The dashed curves with overlaid circles in Fig. G-3 are the position and acceleration response spikes caused by a 0.01 times critically damped 50 rad/sec vibration mode in the dewar wall. The spike in the position response is of little concern because it is 25 dB down. On the other hand, the spike in acceleration response nearly destroys the acceleration attenuation achieved in the compensation. The system's acceleration response is degraded from 30 to 60 rad/sec. The system's noise performance is substantially degraded because there are far more cycles of white noise in this range than under the original response peak from 2 to 10 rad/sec. This shows that it is important to place the satellites mechanical frequencies as high as possible. Decoupling the quartz block from the outer body helps attenuate the vibration noise but both translational and rotational decoupling will probably be necessary if the vibration frequencies can't be set high enough.

Figure G-4 shows root locus plots for four versions of the simple one-stage system. For each system the lead break is at 1.5 rad/sec and unity gain gives $\sqrt{\frac{k}{I}} = 3$ rad/sec. The systems differ in that the double lag is placed at 4, 5, 6 and 10 times 1.5 rad/sec.

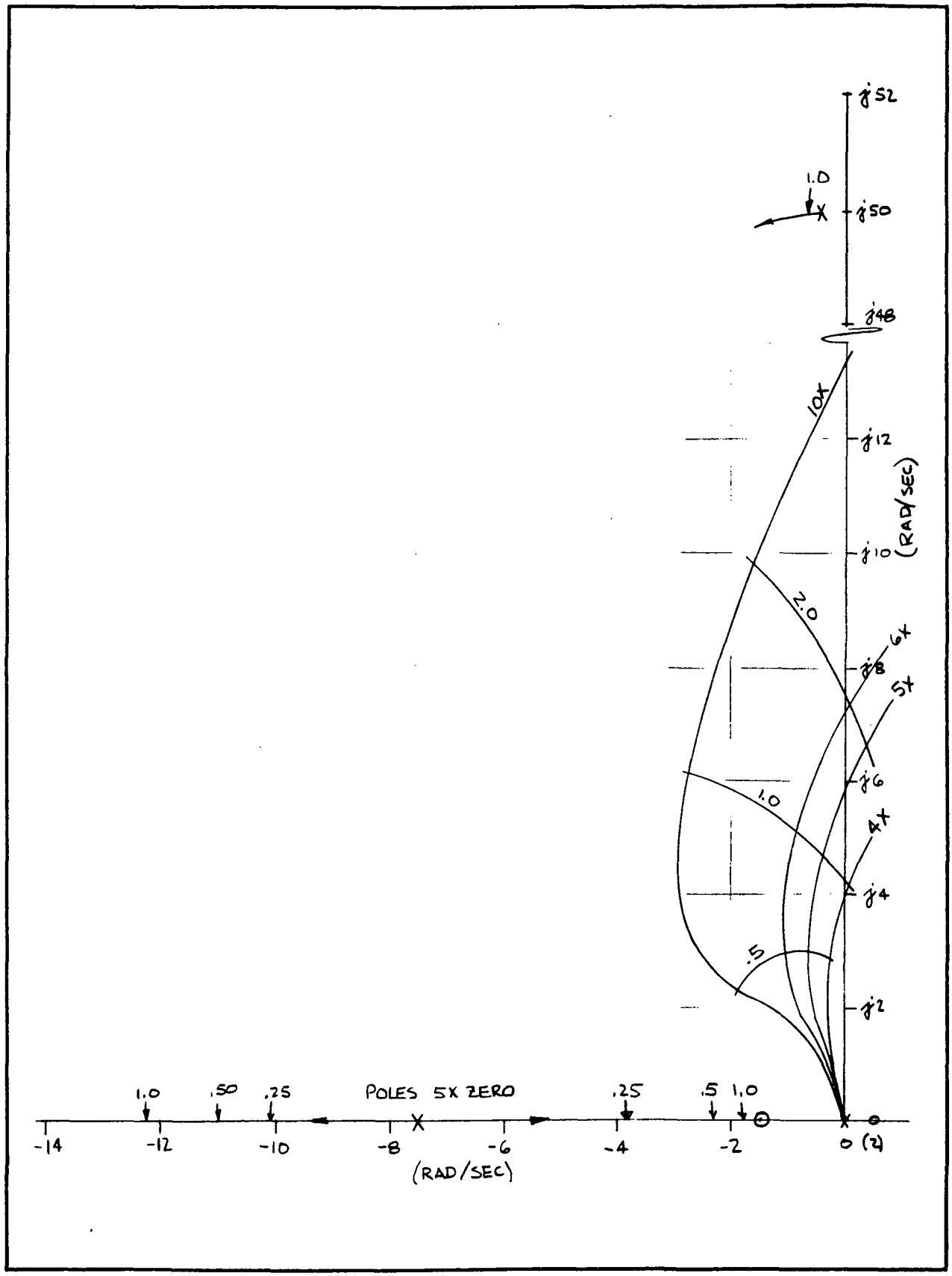


Fig. G-4 Root-Locus for One-Stage System with Lead at 1.5 rad/sec and Lags at 4, 5, 6 and 10 Times as High

The locuses show how the gain margin and damping are reduced as the open-loop poles are brought in closer to the zero. For a factor of 5 spacing and using a nominal gain of one-half, the simple system has a gain margin of a factor of 3, and its best damping is 0.3 times critical. This spacing was tentatively selected for the simple system because its acceleration response is much less sensitive than for wider spacing.

The simple systems whose frequency responses are given in Figs. G-5, G-6, and G-7 differ from those in G-2 and G-3 in that the gain is reduced to give $\sqrt{\frac{k}{I}}$ = 1.5 rad/sec as was recommended in Section 6. The spacing between the zero and poles in these three figures is the same, but the location of the zero is varied from 1 to 1.5 to 2 rad/sec. It is a rule-of-thumb that the lead break must be put in at a lower frequency than the open-loop unity crossover to get good damping. However, the close spacing of the poles (which roll-off the sensor noise) invalidates this rule. Damping is worse in Fig. G-5 where the zero and poles are nearly equally spaced below and above the open loop unity crossover. Best damping is achieved in Fig. G-6 where the zero is on top of the unity crossover. Damping in Fig. G-7, where the zero is actually above the unity crossover point, is slightly better than in Fig. G-5.

The difference in acceleration sensitivity to sensor noise is more dramatic than the difference in damping. The noise sensitivity is substantially reduced by increasing the lead break frequency.

Although these three systems have the same DC gain, their bandwidths differ considerably. The system in Fig. G-5 has a bandwidth of over 4 rad/sec. The bandwidth of the system in Fig. G-7 is only about half as large. Therefore the system in Fig. G-5

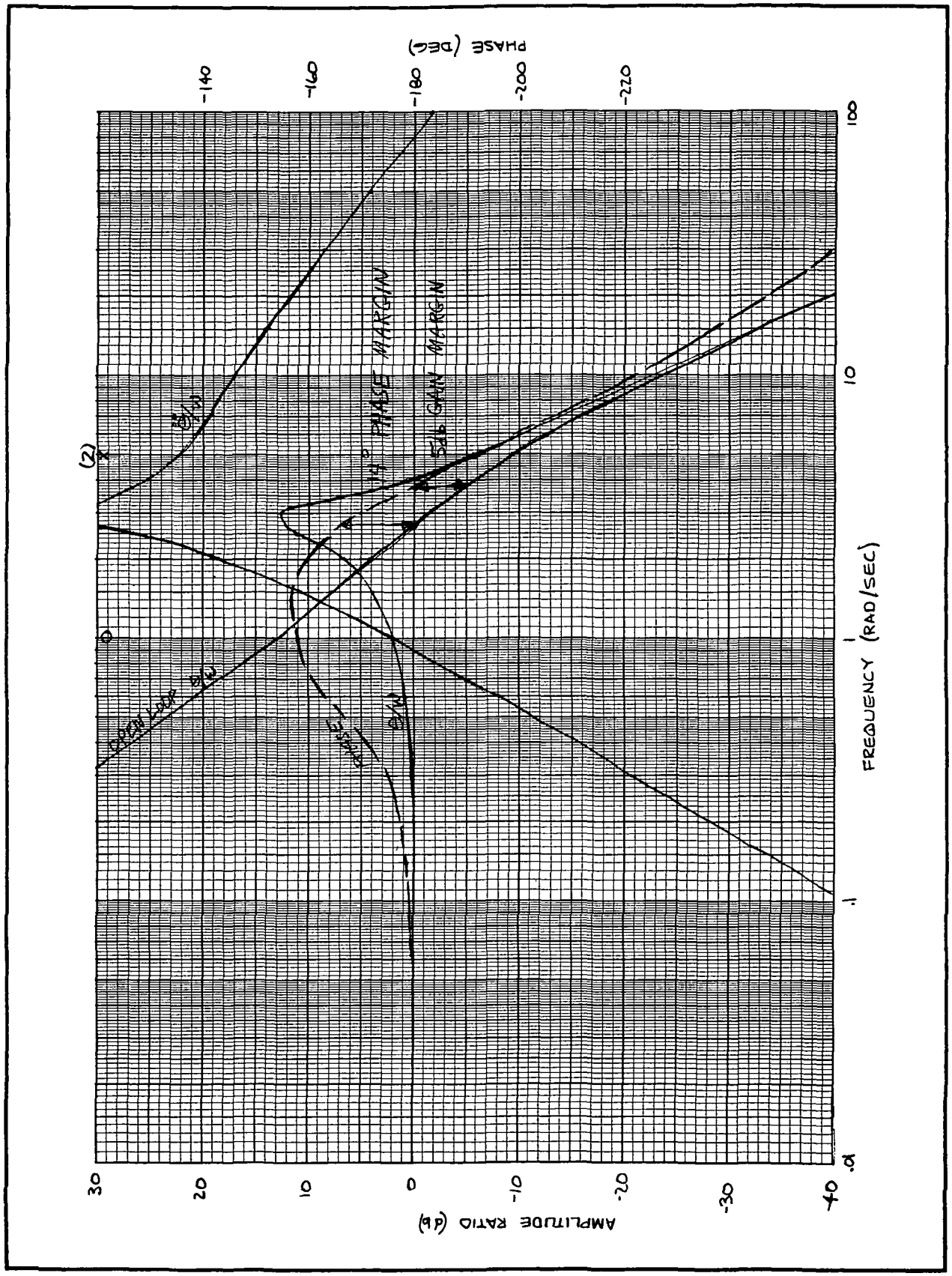


Fig. G-5 Frequency Response of One-Stage System with $\sqrt{K/I}$ = 1.5, Lead at 1, Lags at 5 rad/sec

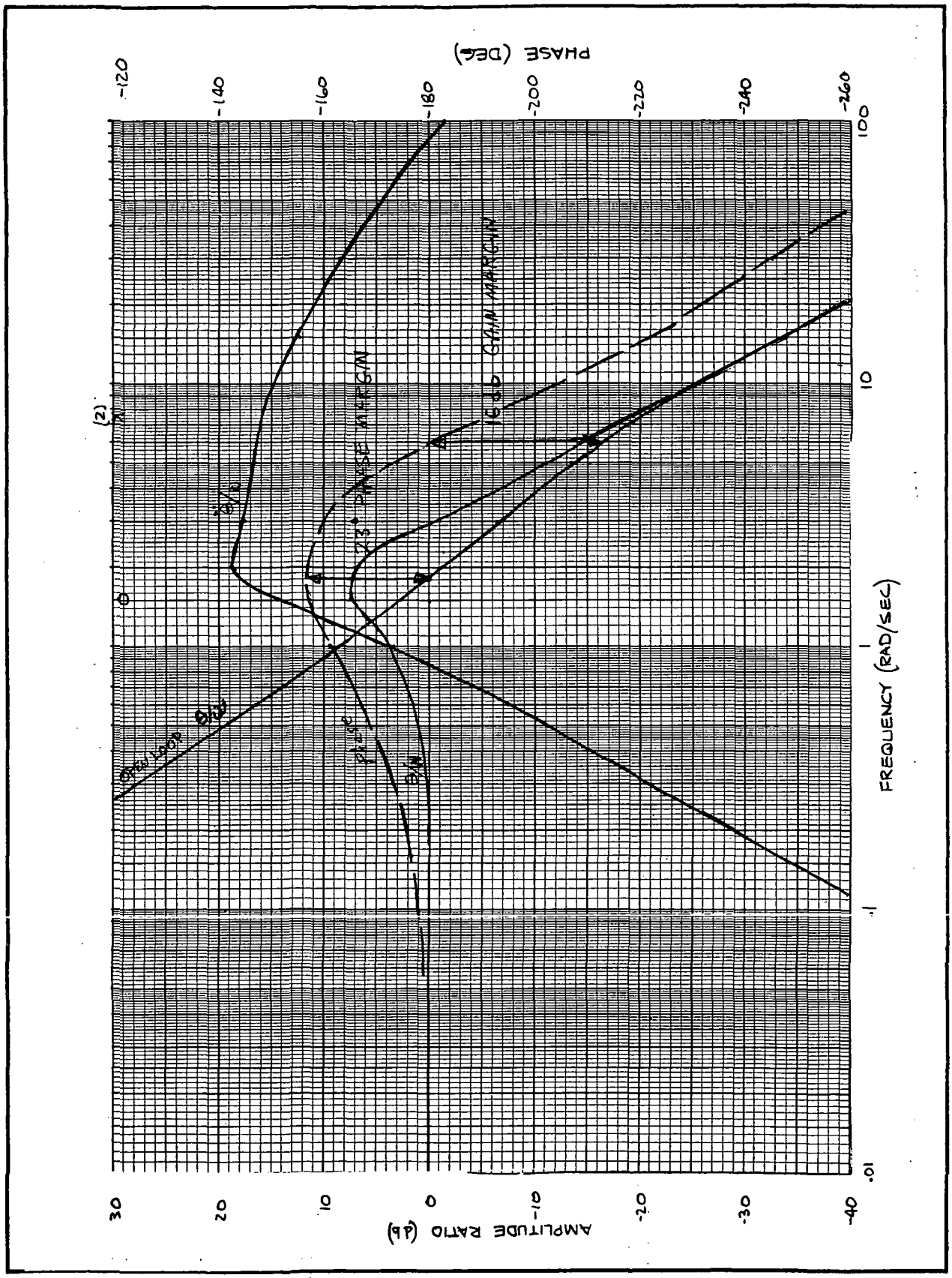


Fig. G-6 Frequency Response of One-Stage System with $\sqrt{K/I}$ = 1.5, Lead at 1.5, Lags at 7.5 rad/sec

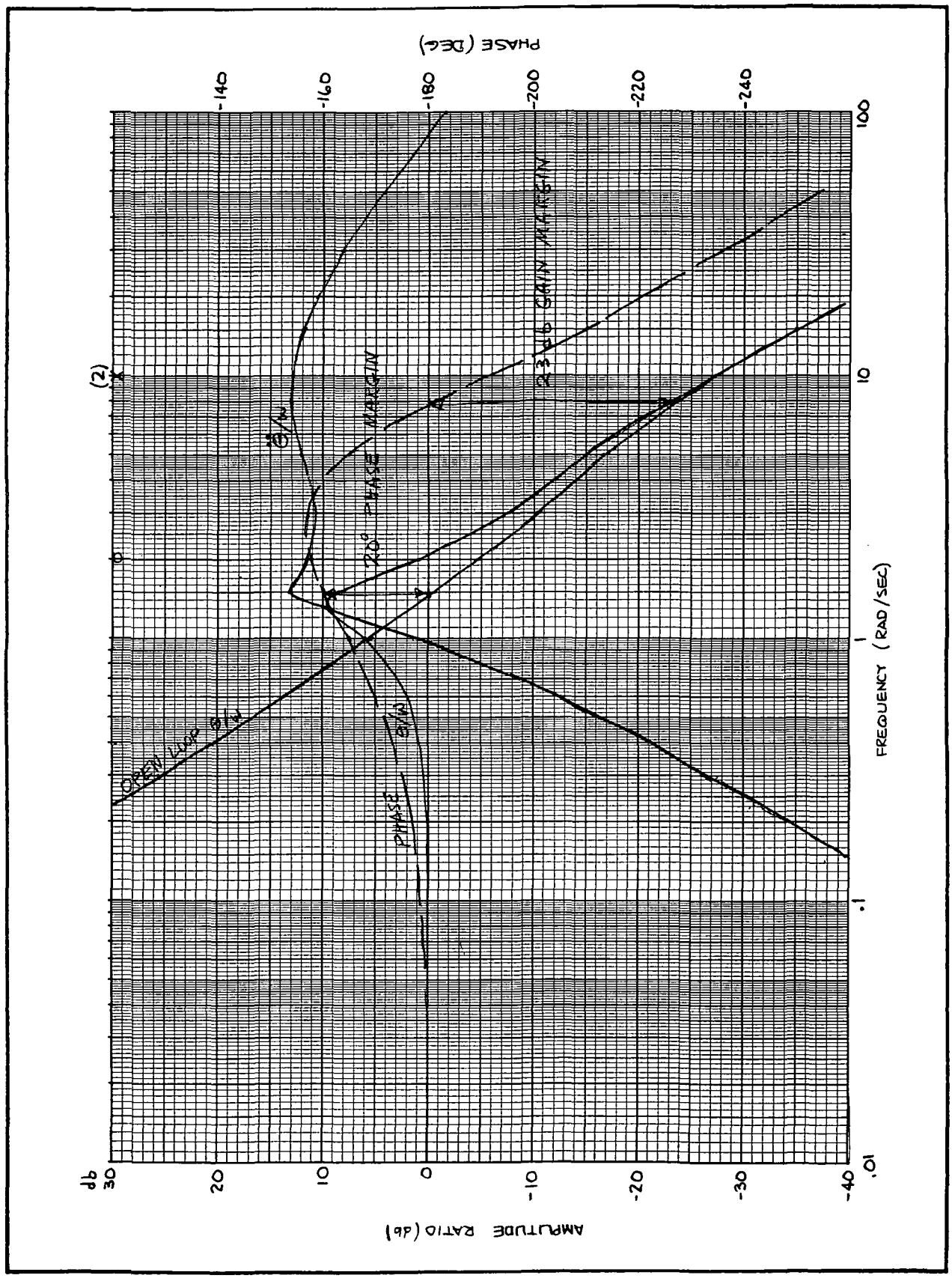


Fig. G-7 Frequency Response of One-Stage System with $\sqrt{K/I}$ = 1.5, Lead at 2, Lags at 10 rad/sec

would compensate for disturbance torques in the 2 to 4 rad/sec range more effectively than the system in Fig. G-7. For most of the SRS control loops, the most important requirement is on DC gain rather than on bandwidth. The zero location used in Fig. G-6 was selected for the preliminary designs given in Section 6, because slightly better damping is achieved and because the acceleration response is only 2 dB higher at 10 rad/sec than for the system in Fig. G-7.

The analog computer simulation results described in Section G-4 show that the modern two-stage controller is insensitive to changes in many parameters but that it is quite sensitive to any changes which cause modeling errors between the plant and the plant model in the estimator. Figures G-8 and G-9 are root-locus plots which graphically show how much more sensitive the system is to parameter variations which cause modeling errors.

In Fig. G-8 the gain on the inner actuator is varied in the plant only. The range of gains for which the system is stable is from about one-third to three times nominal. By contrast, the system is stable for all inner actuator gains greater than 0.15 times nominal when the gain is changed in both the plant and model. (The gain increase increases the system bandwidth in both cases and increases the system's sensitivity to sensor noise. Therefore, gain increase above a given value may not be acceptable even though stability is maintained.)

Figures G-10 and G-11 show how the critical estimator and control poles move for variations of the helium thruster and the error sensor gains. Both of these gains must remain within one-third to three times the nominal values for stability.

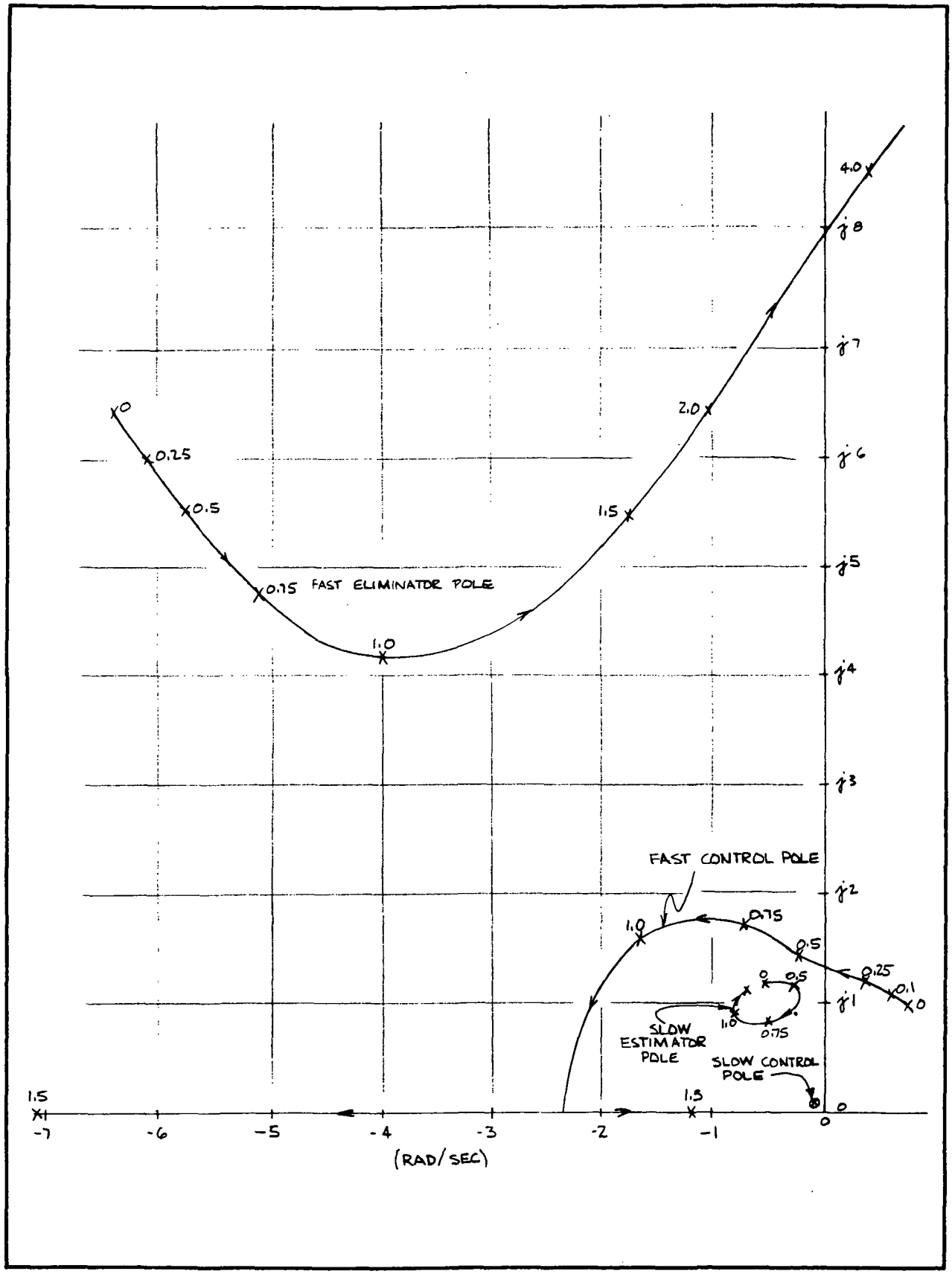


Fig. G-8 Root Locus for Variation of u_1 Gain in the Plant Only (Modern Controller)

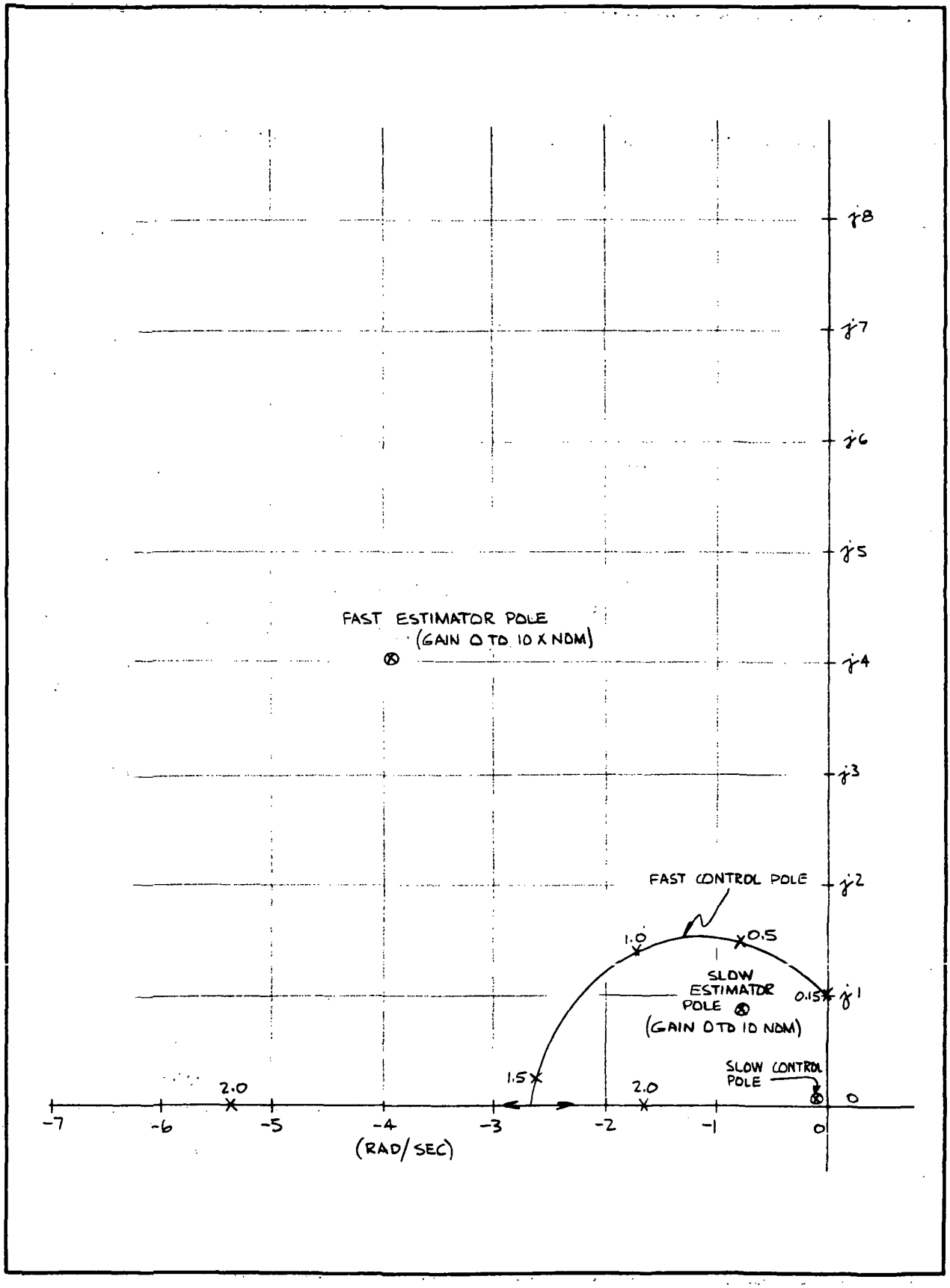


Fig. G-9 Root Locus for Variation of u_1 gain in both plant and Model (Modern Controller)

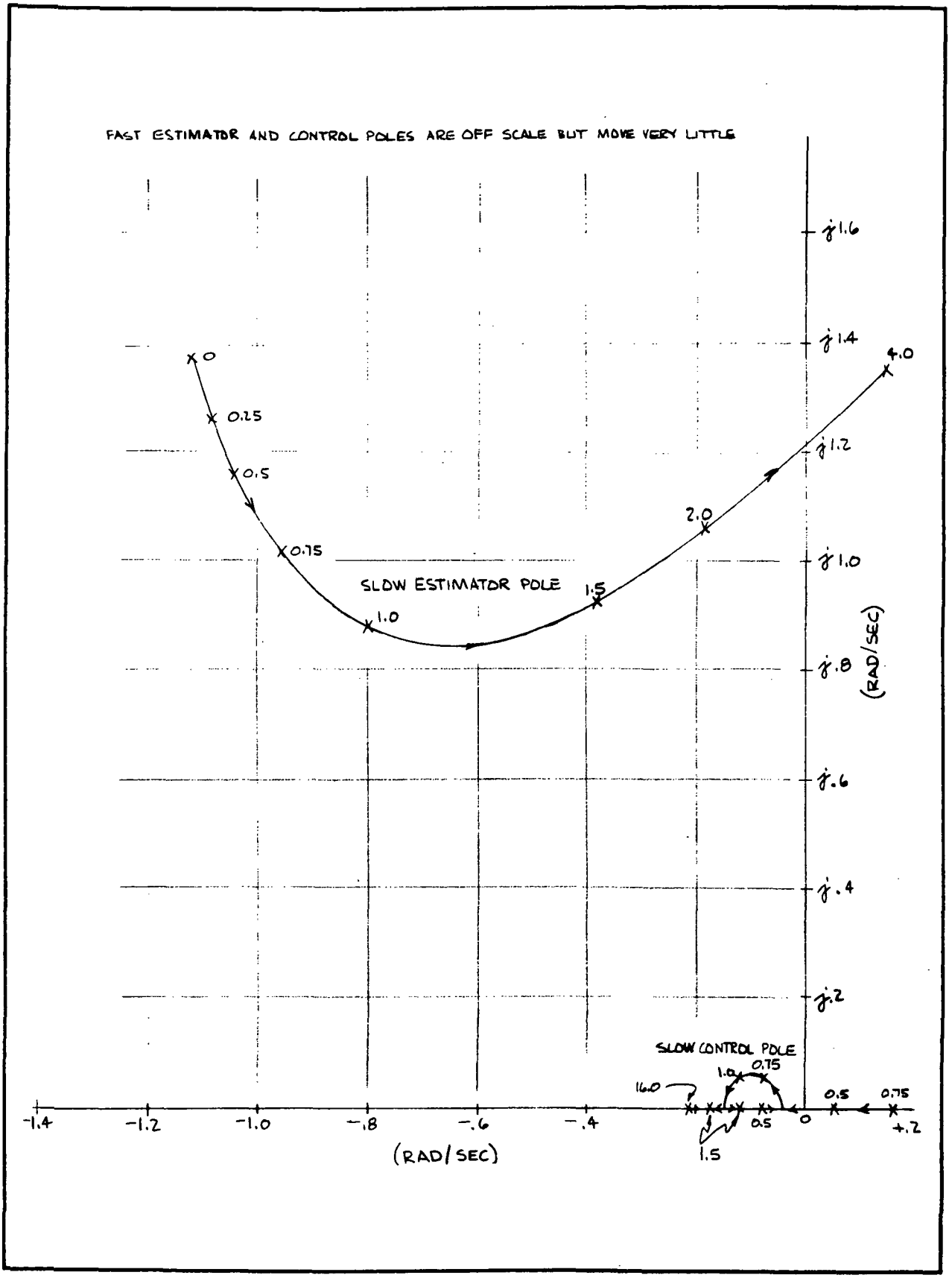


Fig. G-10 Root Locus for Variation of u_2 Gain in the Plant Only (Modern Controller)

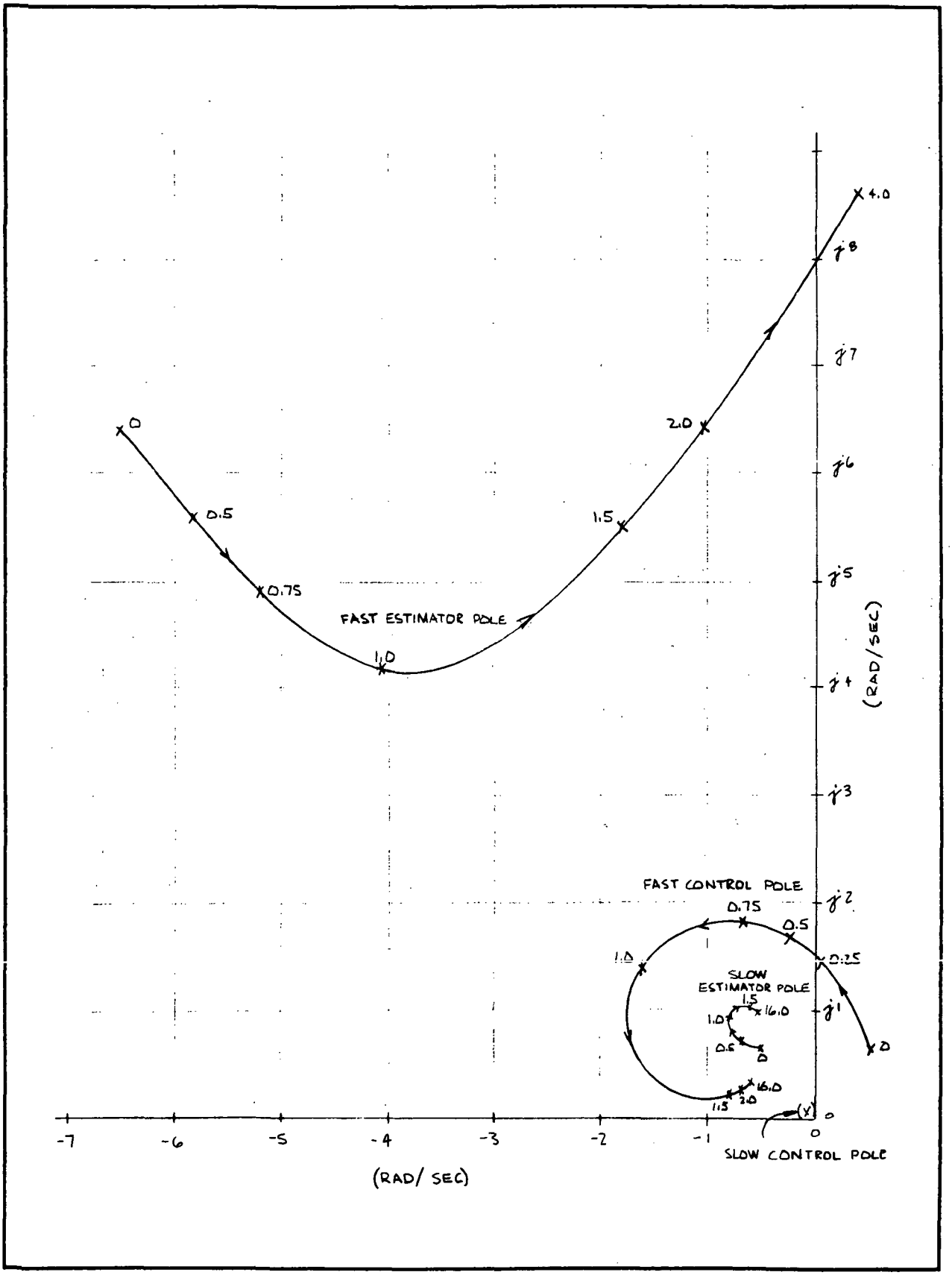


Fig. G-11 Root Locus for Variation of Telescope Gain in the Plant Only (Modern Controller)

This series of root-locus plots helps explain why various frequencies appear and are poorly damped in the analog computer simulations of Section G.4.

G.3 PITCH-YAW ANALOG COMPUTER SIMULATION DESCRIPTION

The pitch-yaw control systems are implemented as two stage modern control systems. One axis is shown schematically in Fig. G-12. One plant measurement, the inertial position of the quartz block, drives a mathematical model of the plant which estimates all the plant state variables. The control commands, formed from these estimates, drive both the plant and the model.

The analog simulation evolved over six sets of data and three distinct configurations. The beginning configuration used seven states to describe the plant and another seven to describe the model. The system dynamic model for this configuration is shown in Fig. G-13. In the intermediate configuration, the dewar was assumed to be rigidly attached to the outer body, thus only five state variables each were used in describing the plant and the model. For the final configuration, the beginning plant requiring seven state variables was estimated by the intermediate model using five state variables. This was done to verify that it is not necessary to model and estimate the satellite's relatively high frequency vibration modes.

Equations of Motion:

By inspection of Fig. G-13, the equations of motion of the beginning or "full" plant are:

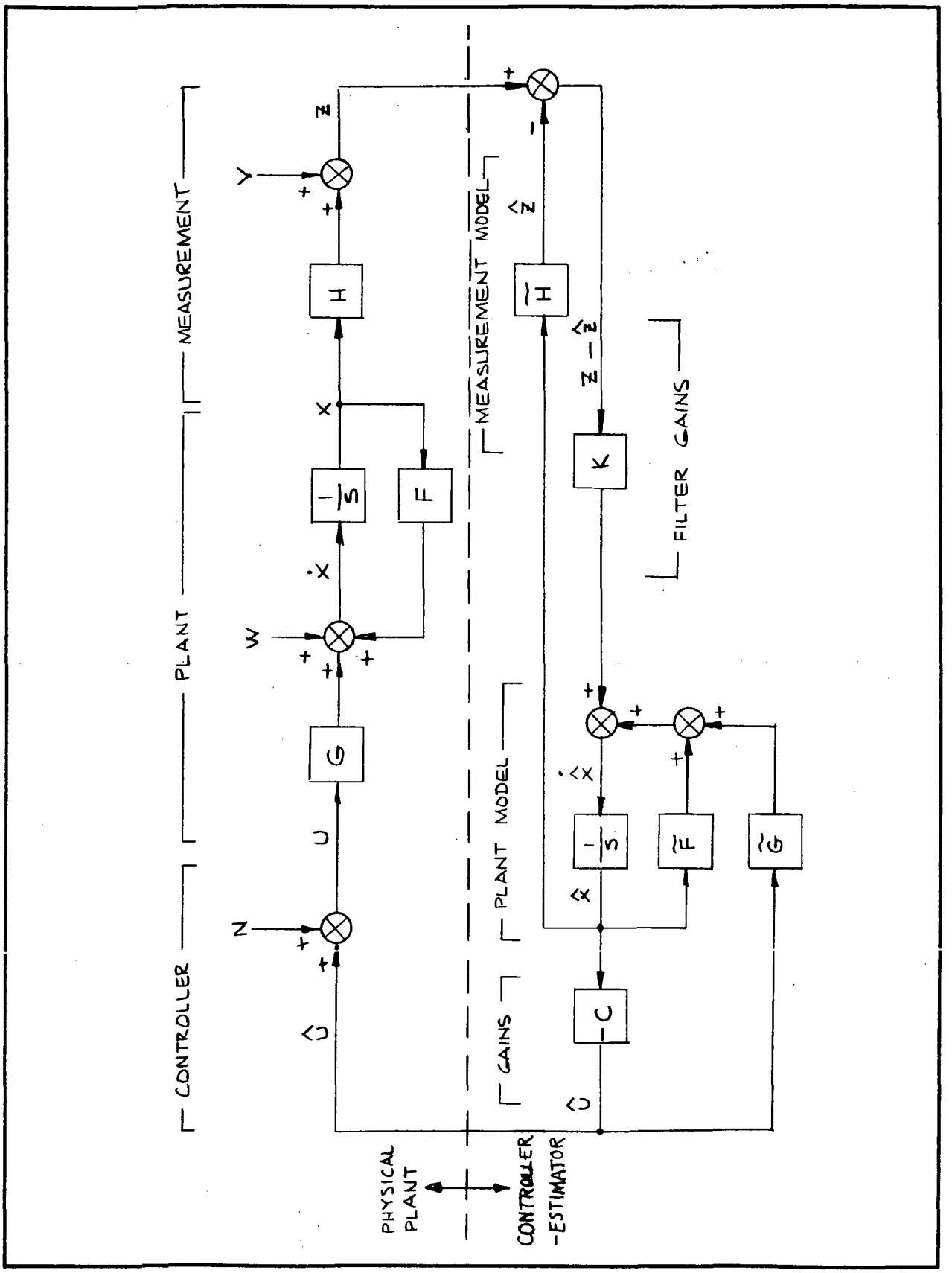


Fig. G-12 Pitch-Yaw Two Stage Control System

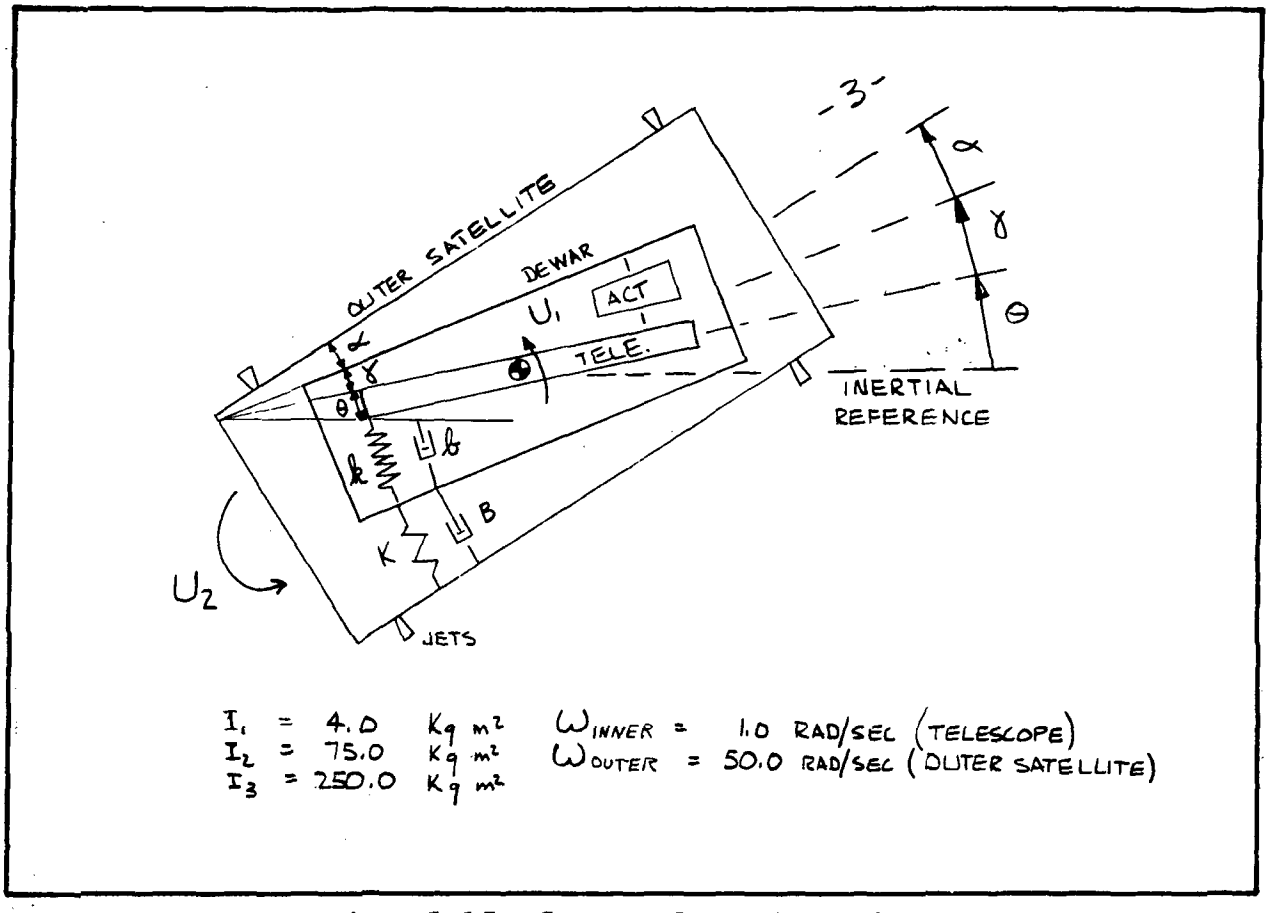


Fig. G-13 System Dynamic Model

$$u_1 + k\gamma + b\dot{\gamma} = I_1 \ddot{\theta}$$

$$-u_1 - k\gamma - b\dot{\gamma} + K\alpha + B\dot{\alpha} = I_2 (\ddot{\theta} + \ddot{\gamma}) \qquad \text{(Eq G-1)}$$

$$u_2 - K\alpha - B\dot{\alpha} = I_3 (\ddot{\theta} + \ddot{\gamma} + \ddot{\alpha})$$

By Laplace transforming and putting into matrix form, (Eq G-1) becomes

$$\begin{bmatrix} S^2 & -I_1^{-1}(bS+k) & 0 \\ S^2 & S^2+I_2^{-1}(bS+k) & -I_2^{-1}(BS+K) \\ S^2 & S^2 & S^2+I_3^{-1}(BS+K) \end{bmatrix} \begin{pmatrix} \theta \\ \gamma \\ \alpha \end{pmatrix} = \begin{pmatrix} I_1^{-1} \\ -I_2^{-1} \\ 0 \end{pmatrix} u_1 + \begin{pmatrix} 0 \\ 0 \\ I_3^{-1} \end{pmatrix} u_2$$

(Eq G-2)

This set is not readily adaptable to state variable form. Further it exhibits algebraic loops in acceleration which are not desirable for analog simulation. For these reasons, $\ddot{\theta}$ is eliminated from the second equation and $\ddot{\theta}$ and $\ddot{\gamma}$ are eliminated from the third equation to yield:

$$\begin{bmatrix} S^2 & -I_1^{-1}(bS+k) & 0 \\ 0 & S^2+(I_1^{-1}+I_2^{-1})(bS+k) & -I_2^{-1}(BS+K) \\ 0 & -I_2^{-1}(bS+k) & S^2+(I_2^{-1}+I_3^{-1})(BS+K) \end{bmatrix} \begin{pmatrix} \theta \\ \gamma \\ \alpha \end{pmatrix} = \begin{pmatrix} I_1^{-1}u_1 \\ -(I_1^{-1}+I_2^{-1})u_1 \\ I_2^{-1}u_1+I_3^{-1}u_2 \end{pmatrix}$$

(Eq G-3)

This set is both easy to put in state variable form and easy to simulate on an analog computer. However, now the control function u_1 appears in all equations. For some purposes, it is more convenient to have each control function appear in only one equation. By transforming coordinates as follows:

$$\begin{aligned} Y_4 &= \theta + a\gamma \\ Y_6 &= \theta + \gamma + \alpha \\ a &= I_2 (I_1 + I_2)^{-1} \end{aligned} \qquad \text{(Eq G-4)}$$

the equations of motion become:

$$\begin{bmatrix} S^2+a^{-1}I_1^{-1}(bS+k) & -a^{-1}I_1^{-1}(bS+k) & 0 \\ -I_1I_2^{-1}(I_1+I_2)^{-1}(BS+K) & S^2+I_2^{-1}(BS+K) & -(I_1+I_2)^{-1}(BS+K) \\ I_1I_2^{-1}I_3^{-1}(BS+K) & -(I_1+I_2)I_2^{-1}I_3^{-1}(BS+K) & S^2+I_3^{-1}(BS+K) \end{bmatrix} \begin{pmatrix} \theta \\ Y_4 \\ Y_6 \end{pmatrix} = \begin{pmatrix} I_1^{-1}u_1 \\ 0 \\ I_2^{-1}u_2 \end{pmatrix}$$

(Eq G-5)

This set is also easy to put in state variable form and is in fact the set of equations which were simulated.

In the above equations, θ represents the inertial position of the quartz block, γ represents the gimbal or relative angle between the quartz block and the dewar, α represents the relative angle between the dewar and the outer satellite, Y_6 represents the inertial position of the outer satellite, and Y_4 represents the inertial position of the center of mass of the combined quartz block and dewar.

It is apparent by inspection of Equations G-2, and G-3, that the characteristic equation of the dynamic model contains two poles at the origin. This is not apparent in Equation G-5, and in fact depends upon the subtraction of two pairs of very large numbers to obtain this result. This caused difficulty in the analog simulation because four significant figure pot settings are not accurate enough to properly locate the closed-loop low frequency roots. Changes of 0.1 percent in the pot settings involved in this subtraction can move one set of low frequency roots from exponentially divergent to stable and well damped to sinusoidally divergent. In running the simulation, one pot setting was varied until this set of roots were placed as close as possible to the closed loop roots given us by Stanford. In running the simulation, the offset was tuned out prior to running and periodically throughout the day between runs.

These sensitivity problems disappeared when the intermediate configuration was simulated. For this configuration, the dewar was assumed to be rigidly connected to the outer satellite. This implies $K = B = \infty$ and $\alpha = 0$. The equations of motion for this set are, referring to Fig. G-2,

$$u_1 + k\gamma + b\dot{\gamma} = I_1 \ddot{\theta}$$

$$-u_1 - k\gamma - b\dot{\gamma} + u_2 = I_2 (\ddot{\theta} + \ddot{\gamma}) \qquad \text{(Eq. G-6)}$$

Eliminating $\ddot{\theta}$ from the second equation and defining the center of mass coordinate,

$$Y_4 = \theta + a\gamma$$

$$a = I_2 (I_1 + I_2)^{-1}$$

After Laplace transforming the matrix form of the equations of motion are

$$\begin{bmatrix} S^2 + (aI_1)^{-1}(bS+k) & -(aI_1)^{-1}(bS+k) \\ 0 & S^2 \end{bmatrix} \begin{pmatrix} \theta \\ Y_4 \end{pmatrix} = \begin{pmatrix} I_1^{-1} u_1 \\ I_1 + I_2)^{-1} u_2 \end{pmatrix} \qquad \text{(Eq. G-7)}$$

By inspection, the characteristic equation of this dynamic model has two roots at the origin and a complex pair of frequency $\sqrt{k/aI_1}$.

Equation G-5 can be rewritten as

$$\begin{bmatrix} S^2 + B_{11}S + C_{11} & B_{12}S + C_{12} & 0 \\ B_{21}S + C_{21} & S^2 + B_{22}S + C_{22} & B_{23}S + C_{23} \\ B_{31}S + C_{31} & B_{32}S + C_{32} & S^2 + B_{33}S + C_{33} \end{bmatrix} \begin{pmatrix} \theta \\ Y_4 \\ Y_6 \end{pmatrix} = \begin{pmatrix} I_1^{-1} u_1 \\ 0 \\ I_2^{-1} u_2 \end{pmatrix} \qquad \text{(Eq. G-8)}$$

where:

$$B_{11} \triangleq b/aI \qquad B_{23} \triangleq -B/(I_1+I_2)$$

$$C_{11} \triangleq k/aI \qquad C_{23} \triangleq -K/(I_1+I_2)$$

$$B_{12} \triangleq -B_{11} \qquad B_{31} \triangleq I_1B/I_2I_3$$

$$C_{12} \triangleq -C_{11} \qquad C_{31} \triangleq I_1K/I_2I_3$$

$$B_{21} \triangleq -I_1B/[I_2(I_1+I_2)] \qquad B_{32} \triangleq -(I_1+I_2)B/I_2I_3$$

$$C_{21} \triangleq -I_1K/[I_2(I_1+I_2)] \qquad C_{32} \triangleq -(I_1+I_2)K/I_2I_3$$

$$B_{22} \triangleq B/I_2 \qquad B_{33} \triangleq B/I_3$$

$$C_{22} \triangleq K/I_2 \qquad C_{33} \triangleq K/I_3$$

(Eq. G-9)

To convert to state variables, let

$$Y \triangleq \begin{pmatrix} X_1 \\ X_2 \\ X_3 \\ X_4 \\ X_5 \\ X_6 \\ X_7 \end{pmatrix} \triangleq \begin{pmatrix} \int \theta \, dt \\ \theta \\ \dot{\theta} \\ Y_4 \\ \dot{Y}_4 \\ Y_6 \\ \dot{Y}_6 \end{pmatrix}$$

(Eq. G-10)

The state variable equations of motion of the beginning configuration corresponding to Equation G-8 are

$$\dot{Y} = FY + GU + W$$

(Eq. G-11)

where

$$F \triangleq \begin{bmatrix} 0 & 1 & 0 & 0 & 0 & 0 & 0 \\ 0 & 0 & 1 & 0 & 0 & 0 & 0 \\ 0 & -C_{11} & -B_{11} & -C_{12} & -B_{12} & 0 & 0 \\ 0 & 0 & 0 & 0 & 1 & 0 & 0 \\ 0 & -C_{21} & -B_{21} & -C_{22} & -B_{22} & -C_{23} & -B_{23} \\ 0 & 0 & 0 & 0 & 0 & 0 & 1 \\ 0 & -C_{31} & -B_{31} & -C_{32} & -B_{32} & -C_{33} & -B_{33} \end{bmatrix} \quad \text{(Eq. G-12)}$$

$$G \triangleq \begin{bmatrix} 0 & 0 \\ 0 & 0 \\ I_1^{-1} & 0 \\ 0 & 0 \\ 0 & 0 \\ 0 & 0 \\ 0 & I_3^{-1} \end{bmatrix} \qquad w \triangleq \begin{pmatrix} w_1 \\ w_2 \\ w_3 \\ w_4 \\ w_5 \\ w_6 \\ w_7 \end{pmatrix} \triangleq \text{Disturbance Noise}$$

(Eq. G-13)

Equation G-7 can be rewritten as

$$\begin{bmatrix} S^2+B_{11}S+C_{11} & B_{12}S+C_{12} \\ 0 & S^2 \end{bmatrix} \begin{pmatrix} \theta \\ Y_4 \end{pmatrix} = \begin{pmatrix} I_1^{-1} u_1 \\ (I_1+I_2)^{-1} u_2 \end{pmatrix} \quad \text{(Eq. G-14)}$$

where

$$B_{11} \triangleq b/aI_1 \qquad B_{12} \triangleq -B_{11}$$

$$C_{11} \triangleq k/aI_1 \qquad C_{12} \triangleq -C_{11}$$

(Eq. G-15)

To convert to state variables, let

$$Y \triangleq \begin{pmatrix} Y_1 \\ Y_2 \\ Y_3 \\ Y_4 \\ Y_5 \end{pmatrix} \triangleq \begin{pmatrix} \int \theta \, dt \\ \theta \\ \dot{\theta} \\ Y_4 \\ \dot{Y}_6 \end{pmatrix} \qquad \text{(Eq. G-16)}$$

The state variable equations of motion of the intermediate configuration corresponding to Equation G-14 is given by Equation G-11 where

$$F \triangleq \begin{bmatrix} 0 & 1 & 0 & 0 & 0 \\ 0 & 0 & 1 & 0 & 0 \\ 0 & -C_{11} & -B_{11} & -C_{12} & -B_{12} \\ 0 & 0 & 0 & 0 & 1 \\ 0 & 0 & 0 & 0 & 0 \end{bmatrix} \qquad \text{(Eq. G-17)}$$

$$G \triangleq \begin{bmatrix} 0 & 0 \\ 0 & 0 \\ I_1^{-1} & 0 \\ 0 & 0 \\ 0 & (I_1+I_2)^{-1} \end{bmatrix} \quad w \triangleq \begin{pmatrix} w_1 \\ w_2 \\ w_3 \\ w_4 \\ w_5 \end{pmatrix} \triangleq \text{Disturbance Noise} \qquad \text{(Eq. G-18)}$$

The matrix equations of motion of the entire closed loop system shown in Fig. G-12 are

$$
\begin{aligned}
\dot{Y} &= FY + GU + W \\
\dot{\hat{Y}} &= \tilde{F}\hat{Y} + \tilde{G}\hat{U} + K(Z - \hat{Z}) \\
Z &= HY + V \\
\hat{Z} &= \tilde{H}\hat{Y} \\
\hat{U} &= -C\hat{Y} \\
U &= \hat{U} + N
\end{aligned}
\qquad \text{(Eq. G-19)}
$$

where the "hatted" variables refer to the state variable estimates, the measurement estimate, and control commands. Nominally

$$
\begin{aligned}
\tilde{F} &= F \\
\tilde{G} &= G \\
\tilde{H} &= H
\end{aligned}
\qquad \text{(Eq. G-20)}
$$

When this is true, the eigenvalues separate into plant and filter eigenvalues

$$(F - GC)\,(F - KH) \qquad \text{(Eq. G-21)}$$

The remaining matrices not already defined are:

$$u \triangleq \begin{pmatrix} u_1 \\ u_2 \end{pmatrix} = \begin{pmatrix} \text{Actuator Torque} \\ \text{Jet Torque} \end{pmatrix} \qquad \text{(Eq. G-22)}$$

$$H \triangleq (H_1\ H_2\ H_3\ \ldots\ H_j) \quad j = 5 \text{ or } 7 \qquad \text{(Eq. G-23)}$$

$$C \triangleq \begin{bmatrix} C_{11} & C_{12} & C_{13} & \ldots & C_{1j} \\ C_{21} & C_{22} & C_{23} & \ldots & C_{2j} \end{bmatrix} \quad j = 5 \text{ or } 7 \qquad \text{(Eq. G-24)}$$

$$K = \begin{pmatrix} K_1 \\ K_2 \\ K_3 \\ \vdots \\ K_j \end{pmatrix} \qquad j = 5 \text{ or } 7 \qquad \text{(Eq. G-25)}$$

$$N = \begin{pmatrix} N_1 \\ N_2 \end{pmatrix} = \begin{pmatrix} \text{Actuator Noise} \\ \text{Jet Noise} \end{pmatrix} \qquad \text{(Eq. G-26)}$$

$$Z = Z_1 = \theta + V_1 \qquad \text{(Eq. G-27)}$$

$$V = V_1 = \text{(sensor noise)} \qquad \text{(Eq. G-28)}$$

The scalar quantities in the "hatted" matrices are simply "hatted." For example:

$$\hat{u} \triangleq \begin{pmatrix} \hat{u}_1 \\ \hat{u}_2 \end{pmatrix} \qquad \text{(Eq. G-29)}$$

etc.

Parameter values:

The results of the simulation of the last two configurations are given later in this appendix. The parameters used are given below:

$$\left.\begin{aligned} I_1 &= 4. \\ I_2 &= 75. \\ I_3 &= 250. \end{aligned}\right\} \text{Full Plant} \qquad \left.\begin{aligned} I_1 &= 4 \\ I_2 &= 325 \end{aligned}\right\} \text{Model and Reduced Plant}$$

Only the plants differ in the two configurations. The full plant contains the α mode. The reduced plant does not. The model does not contain the α mode in either case. The matrices follow:

$$F = \begin{bmatrix} 0 & 1 & 0 & 0 & 0 & 0 & 0 \\ 0 & 0 & 1 & 0 & 0 & 0 & 0 \\ 0 & -1 & 0 & 1 & 0 & 0 & 0 \\ 0 & 0 & 0 & 0 & 1 & 0 & 0 \\ 0 & 101.3 & 0 & -2001 & 0 & 1900 & 0 \\ 0 & 0 & 0 & 0 & 0 & 0 & 1 \\ 0 & -32.02 & 0 & 632.3 & 0 & -600.3 & 0 \end{bmatrix} \quad \text{Full Plant}$$

$$\bar{F} = \begin{bmatrix} 0 & 1 & 0 & 0 & 0 \\ 0 & 0 & 1 & 0 & 0 \\ 0 & -1 & 0 & 1 & 0 \\ 0 & 0 & 0 & 0 & 1 \\ 0 & 0 & 0 & 0 & 0 \end{bmatrix} = \tilde{F} \quad \text{Reduced Plant and Model}$$

$$C = \begin{bmatrix} 1.932 & 17.84 & 14.22 & 2.817 & -.3466 \\ 6.468 & -.9229 & -1.034 & 86.63 & 246.8 \end{bmatrix}$$

$$K = \begin{bmatrix} 1.000 \\ 9.511 \\ 45.23 \\ 60.55 \\ 39.65 \end{bmatrix}$$

$$H = \begin{pmatrix} 0 & 1 & 0 & 0 & 0 \end{pmatrix} = \tilde{H}$$

$$G = \begin{bmatrix} 0 & 0 \\ 0 & 0 \\ .25 & 0 \\ 0 & 0 \\ 0 & 0 \\ 0 & 0 \\ 0 & .004 \end{bmatrix}$$ Full Plant

$$G = \begin{bmatrix} 0 & 0 \\ 0 & 0 \\ .25 & 0 \\ 0 & 0 \\ 0 & .003039 \end{bmatrix} = \tilde{G}$$ Reduced Plant and Model

$$N = \begin{pmatrix} 0 \\ 0 \end{pmatrix} \text{ or } \begin{pmatrix} 50.0 \\ 500.0 \end{pmatrix}$$ dyne cm rms white noise bandlimited at 100 rad/sec

$$w = \begin{pmatrix} 0 \\ 0 \\ 0 \\ 0 \\ 0 \end{pmatrix}$$

v = .03 arc-sec rms white noise bandlimited at 100 rad/sec

G.4 SIMULATION RESULTS

The analog computer simulations include the response of the two stage pitch-yaw system to telescope noise, to step changes in the external and interbody disturbance torque, and to offset point commands from the sensor. These simulations characterize the expected orbital response of the system under nominal operating conditions. Runs were also made to show that the flattening of the telescope output for initial errors larger than about 0.5 arc-second can greatly reduce the damping for offset point commands. The effects of errors in modeling the plant within the estimator, including the effect of using a five state model to represent a seven state plant, and the effects of changes in each of the gains in the controller-estimator were simulated in terms of their effects on the system response to an initial error in the telescope angle. Responses to various combinations of initial conditions demonstrate the difference in response characteristics of the inner and outer loops and demonstrate the potential advantages associated with using a modern state variable estimator.

Figure G-14 shows the system response to telescope sensor noise of 0.03 arc-sec (rms) band limited at 100 rad/sec. The input sensor noise is the 4th trace from the top and is labeled w. The second trace from the top is the filtered estimate of the quartz block error, labeled $\hat{\theta}$. The estimator pole for telescope motion is located at about 5 rad/sec and the filtering action is evident from a comparison of the w and $\hat{\theta}$ traces. The four additional state variable estimates are not shown in Fig. G-14, but they are summed together with $\hat{\theta}$ through the two sets of controller gains to produce the inner actuator control torque u_1 and the helium thruster control torque u_2. These control torques are in the 5th and 6th traces from the top in Fig. G-14. By comparing u_1 with $\hat{\theta}$ it can be seen that u_1 follows $\hat{\theta}$ closely. The quartz block acceleration $\ddot{\theta}$ in the 3rd trace from the top of Fig. G-14 closely follows u_1 as is expected.

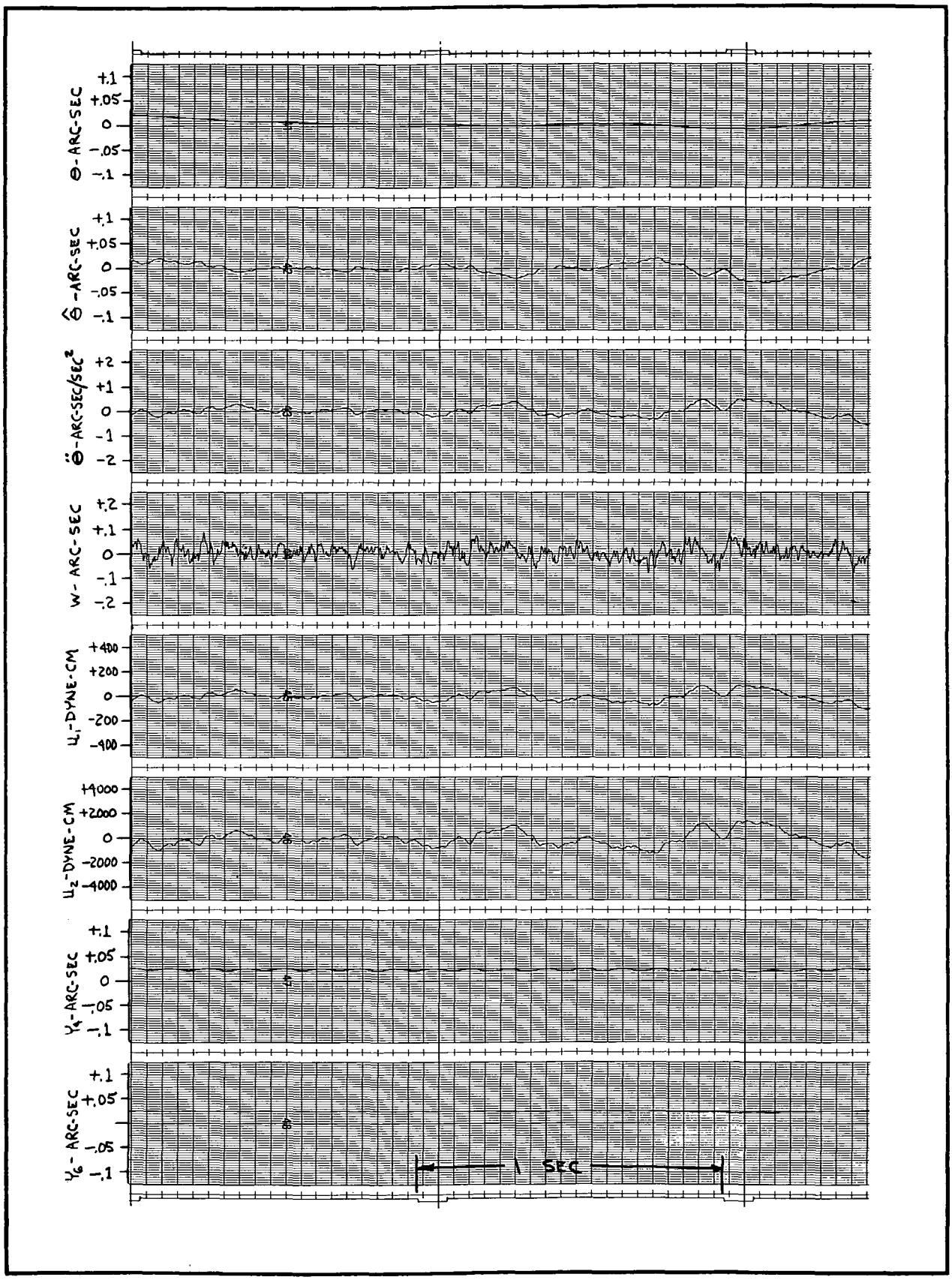


Fig. G-14 Response to 0.03 arc-sec Telescope Noise

The angular motion of the quartz block θ is strongly filtered by the block's inertia as can be seen in the top trace in Fig. G-14. The bottom two traces in Fig. G-14 are approximately the attitude of the middle, Y_4, and outer, Y_6, dewar walls. The large inertias of the middle and outer bodies strongly filter the helium thruster noise u_2. The 50 rad/sec oscillation which is present in both traces is a dewar wall mechanical vibration which was assumed to be undamped in this particular simulation run. The rms values of the traces was electronically measured during the simulation with the following results: θ = 0.01 arc-second, $\hat{\theta}$ = 0.013 arc-second, $\ddot{\theta}$ = 0.22 arc-second/sec^2 = 10^{-6} rad/sec^2, w = 0.03 arc-second, u_1 = 45 dyne-cm = 4.5 10^{-6} N·m, u_2 = 750 dyne-cm = 7.5 x 10^{-5} N·m.

The system response to 100 dyne cm (rms) of thruster noise and 10 dyne cm (rms) of inner actuator noise was also simulated on the analog computer. The traces are not included because they do not help describe the result. The thruster noise had little effect on the quartz block because of the rotational decoupling provided by the gimbals. It had little effect on the outer bodies because of their large inertias. The inner actuator noise caused 0.005 arc-second (rms) quartz block motion and 0.06 arc-second/sec^2 (rms) quartz-block acceleration. The quartz-block motion feeds back through the telescope error signal to give a steady state inner actuator noise of 17 dyne cm (rms) and a thruster noise of 160 dyne cm (rms).

Figure G-15 shows the system step response to ±500 dyne cm step changes in the external disturbance torque. Step changes nearly this large are expected when the satellite enters and leaves the earth shadow. The eight traces are the same as those plotted in Fig. G-14 except that the 4th trace is $\ddot{Y}_4$ (the acceleration of the middle wall of the dewar). The disturbances enter as 500 dyne-cm

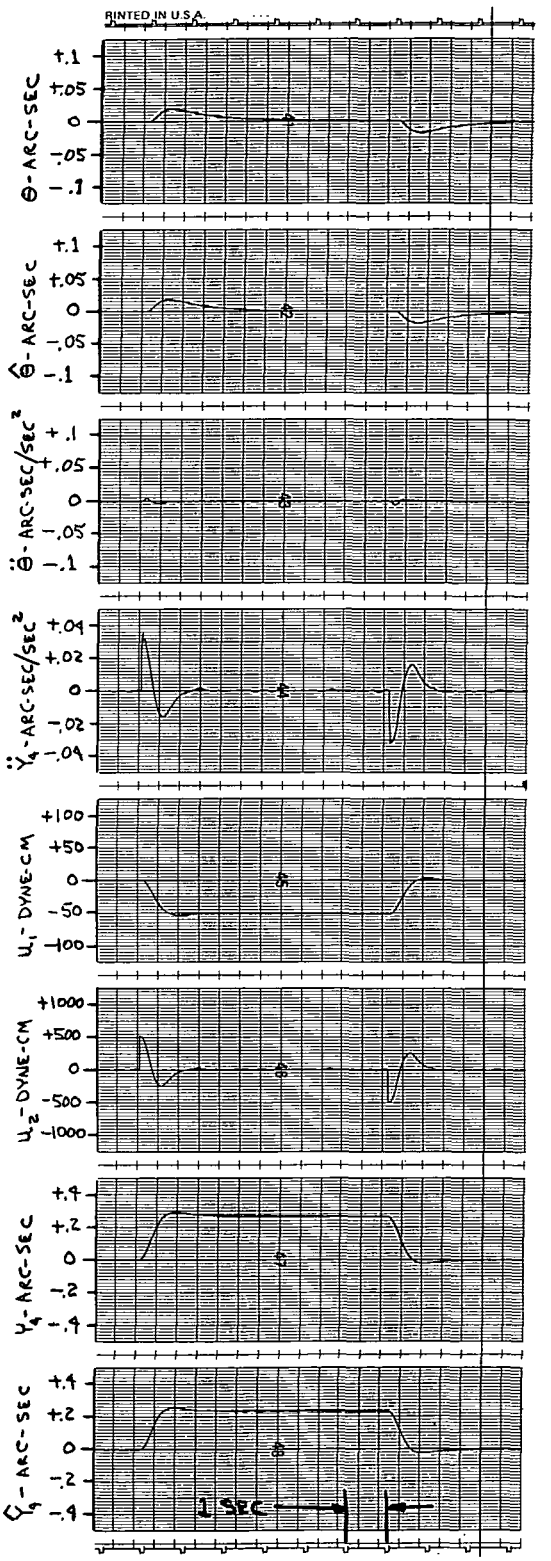


Fig. G-15 Step Response to ±500 dyne-cm Step in External Torque

steps in u_2. The lower two traces in Fig. G-15 show that the static error in pointing the outer satellite grows to about 0.25 arc-second.

The θ trace in Fig. G-15 shows how the integral θ feedback nulls the telescope pointing error. With the telescope error nulled, but with the outer satellite offset at 0.2 5 arc-seconds, the flexure in the telescope gimbal is in torsion. This torque must be reacted by the inner actuator u_1.

Figure G-16 shows the system response to ±0.1 arc-second step commands to θ. In the figure, a positive command is given and is followed by a negative command. Two overshoots are visible in the response following both commands. The $\hat{\theta}$ trace shows the estimate "catching up" with the motion. The peak quartz block acceleration exceeds one arc-second per second squared, but only for a fraction of a second. Peak control torques are over 200 and 400 dyne-cm for the actuators and thrusters respectively. The dewar wall vibration mode is not simulated in Fig. G-16, and the lower trace represents the estimate of the outer body attitude, $\hat{Y}_4$. The quartz block motion has largely settled after 3 seconds. It takes about three times as long for the outer body motion to settle. It takes correspondingly longer for $\hat{Y}_4$ to catch up than for $\hat{\theta}$. Both estimates settle to zero because the flexure is not in torsion and the estimator has no clue that the two bodies have moved to a new attitude.

Figure G-17 shows how the flattening of the telescope output for errors above a certain value interfered with damping. In the left and right half of the figure, error offset commands of ±1 arc-second are simulated. In the left half of the figure the telescope output is assumed to be flattened at 0.25 arc-second as can be seen in the $\hat{\theta}$ trace. On the right hand side the telescope output is limited

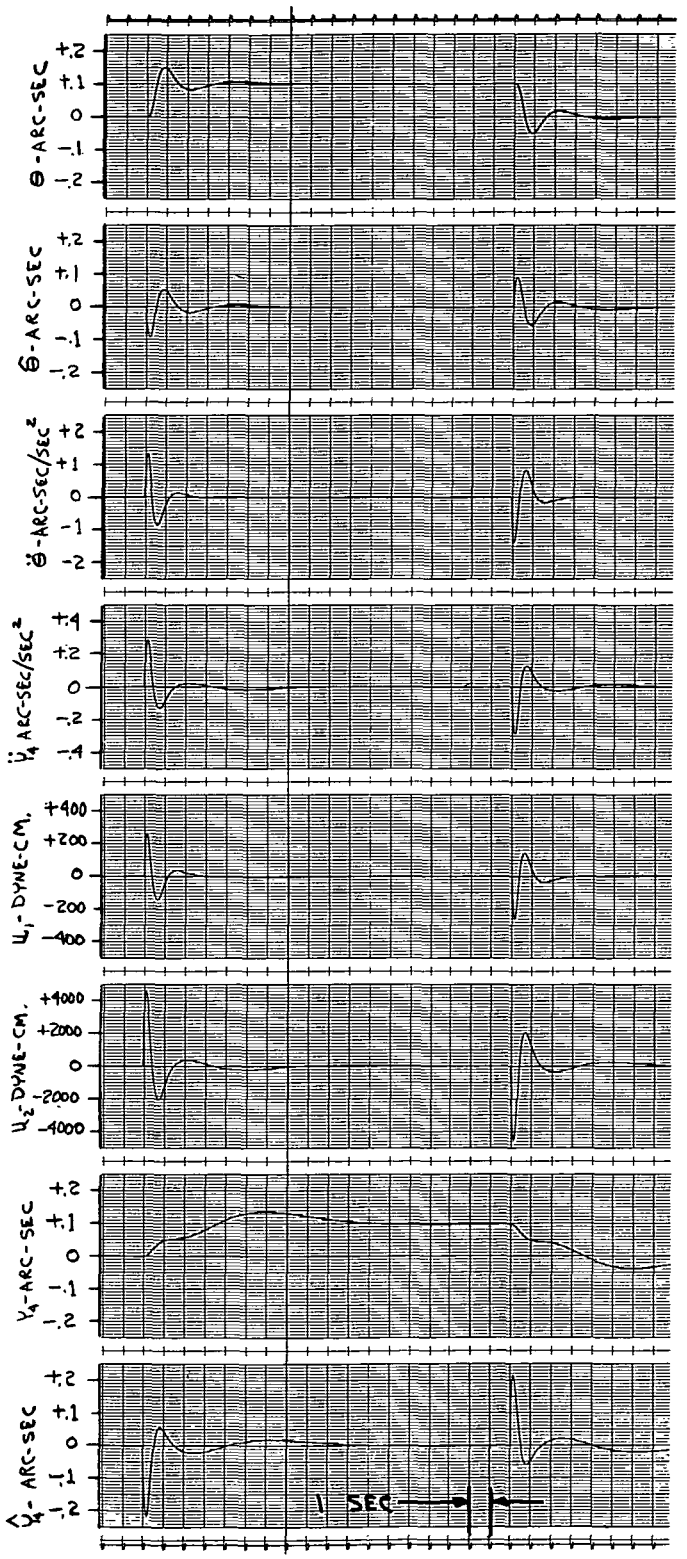


Fig. G-16 Response to ±0.1 arc-sec Step Commands to θ

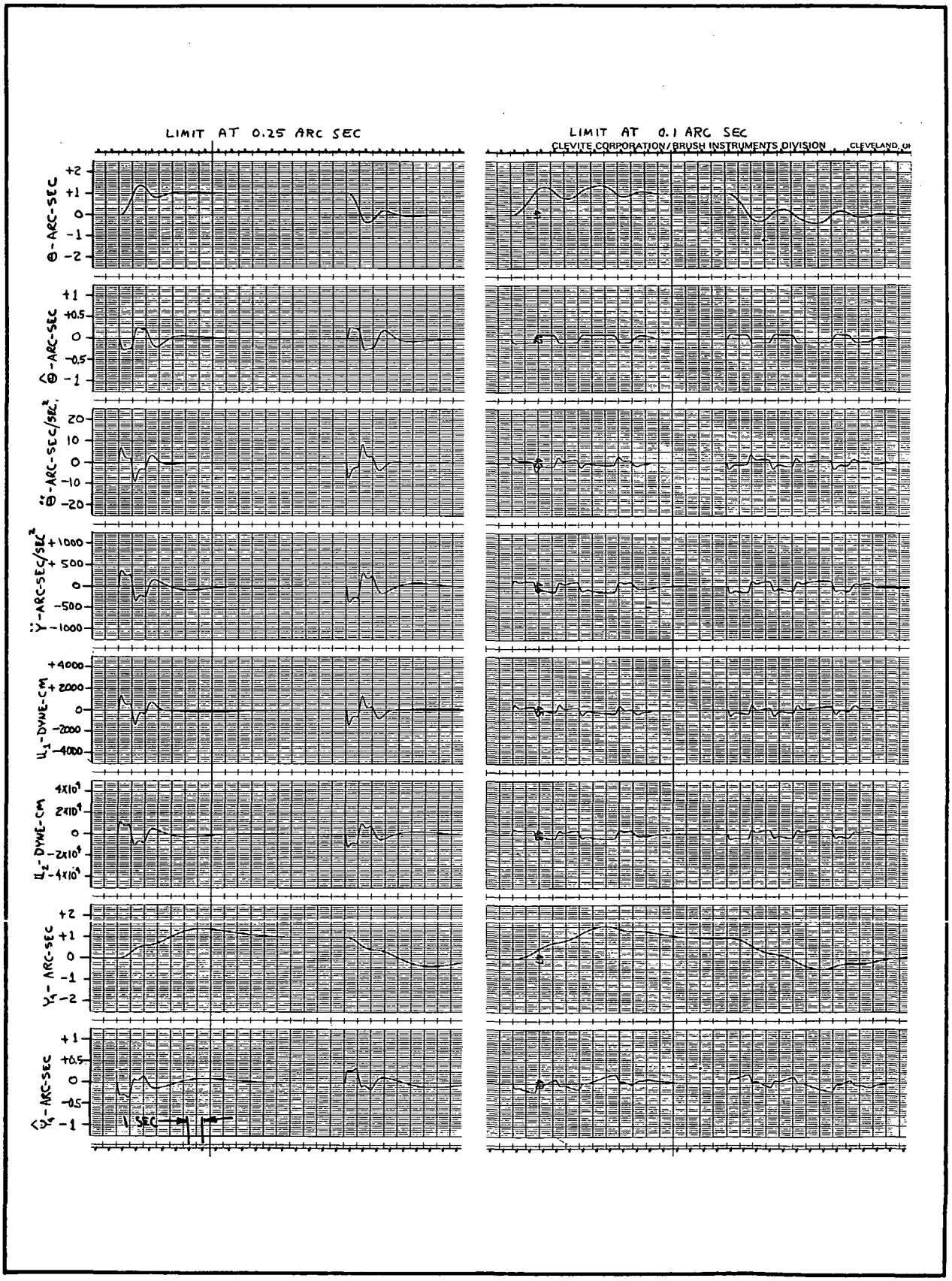


Fig. G-17 Effect of Non-linear Telescope Output

at 0.1 arc-second. The loss of damping is obvious in the θ trace. Instability results for errors 20 times larger than the telescope output limit. The $\hat{Y}_4$ trace shows how the limit on telescope output affects the outer body as well as the telescope attitude estimate. The resulting limits on the state variable estimates are naturally passed on by the controller to u_1 and u_2.

An important potential advantage associated with using a modern state variable estimator is shown in Fig. G-18. The system response to ±0.1 arc-second step commands in the telescope error signal is shown on the left side of the figure. On the right side is shown the response when the step command is entered where $\hat{\theta}$ enters the controller. In this case, the plant and the estimator's model of the plant start at the same initial condition. This allows the model to follow the plant response accurately. The result is a faster and a much better damped response. This is an ideal point to enter intentional offset point or raster scan commands. The system response is slower and less well-damped for signals summed with the telescope error signal. However, the system is less sensitive to sensor noise than it would be if the noise were entered where $\hat{\theta}$ drives the controller.

Figure G-19 shows the system response to an initial 0.1 arc-second error in θ. The first overshoot is larger than in the θ-command response because the gimbal flexure is initially in torsion and effectively increases the gain for the initial condition response. It takes $\hat{\theta}$ a frcction of a second to "catch up" with the quartz block motion. The peak quartz block acceleration is 1.5 arc-second/second^2, but it only lasts for a fraction of a second. The erroneous $\hat{\theta}$ estimate drives the helium thrusters as well as the inner actuator. The outer body is disturbed as a result.

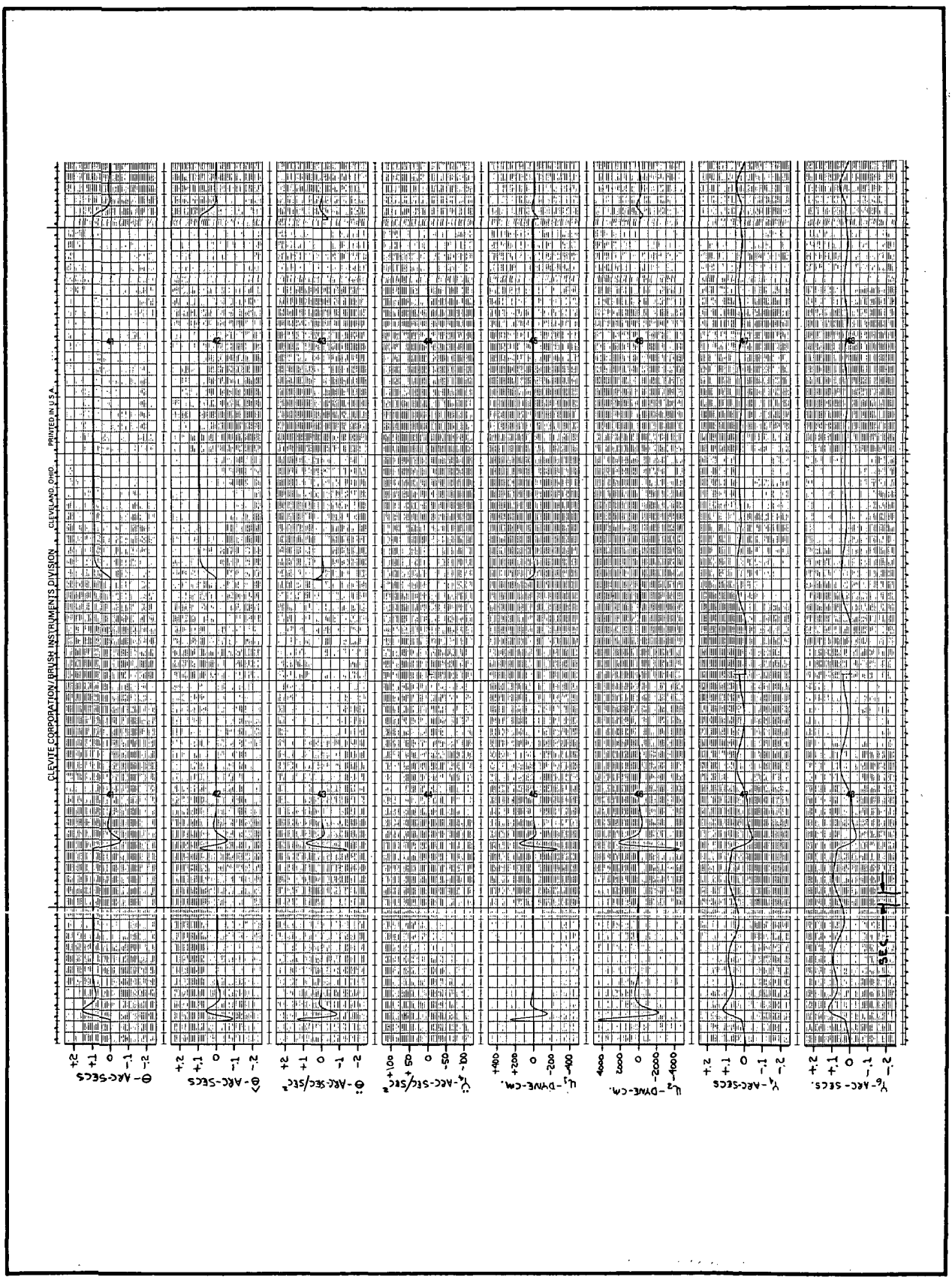


Fig. G-18 Advantage of Commanding the Plant and Model

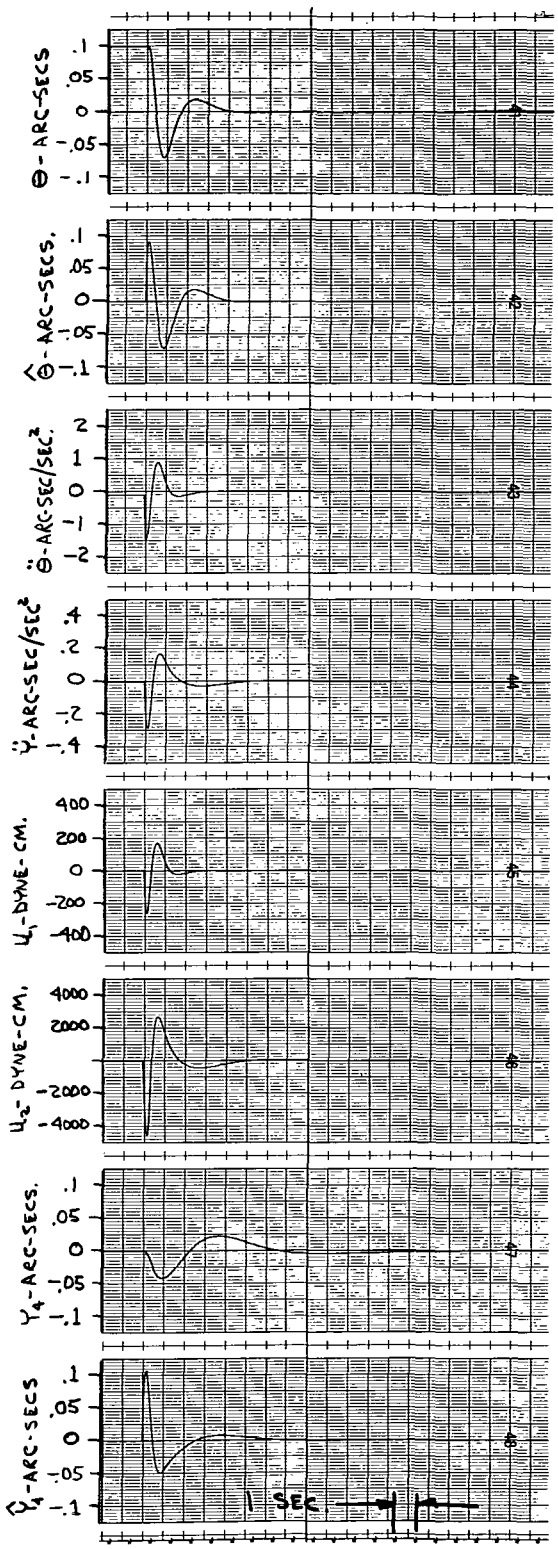


Fig. G-19 Initial Condition Response to $\theta(0) = 0.1$ arc sec

The slower response of the outer loop of the two stage controller is evident from the response to an initial 0.1 arc-second error in Y_4 shown in Fig. G-20. It takes over a second for $\hat{Y}_4$ to "catch up" with Y_4. The inner actuator, as well as the thrusters, is driven by the erroneous $\hat{Y}_4$, but the perturbation in θ is quickly estimated in $\hat{\theta}$ and the $\hat{\theta}$ gain to the inner actuator quickly reduces the resulting offset in θ.

Figure G-21 shows how the system response is improved when the plant and estimator model start with the same initial condition on θ. The improved damping (over Fig. G-19) is dramatic but notice also that the peak quartz block acceleration is only 1/3 as large. Also, the disturbances to the u_2 and to the outer body Y_4 are virtually eliminated. The response to simultaneous initial conditions in Y_4 and $\hat{Y}_4$ shows a similar improvement over that to Y_4 only in Fig. G-20.

The effect of variation of the spring constant of the quartz block flexure is shown in Fig. G-22. Five simulation runs are presented in sequence in the figure. The first is for the nominal inner loop mechanical vibration frequency of 1 rad/sec. In the next four runs the inner body mechanical frequency is varied in the plant without any change being made in the estimator's model. These modeling errors would occur in orbit if either the flexure spring constant or the quartz block or dewar inertias were not accurately known or if they change in orbit.

In the second run in Fig. G-22, where the quartz block mechanical frequency is 1.4 times as large as the estimator model thinks it is, a pronounced lightly damped oscillation occurs in the outer body as can be seen in the bottom two traces. The frequency of this oscillation is about 1 rad/sec which is the frequency of the lowest

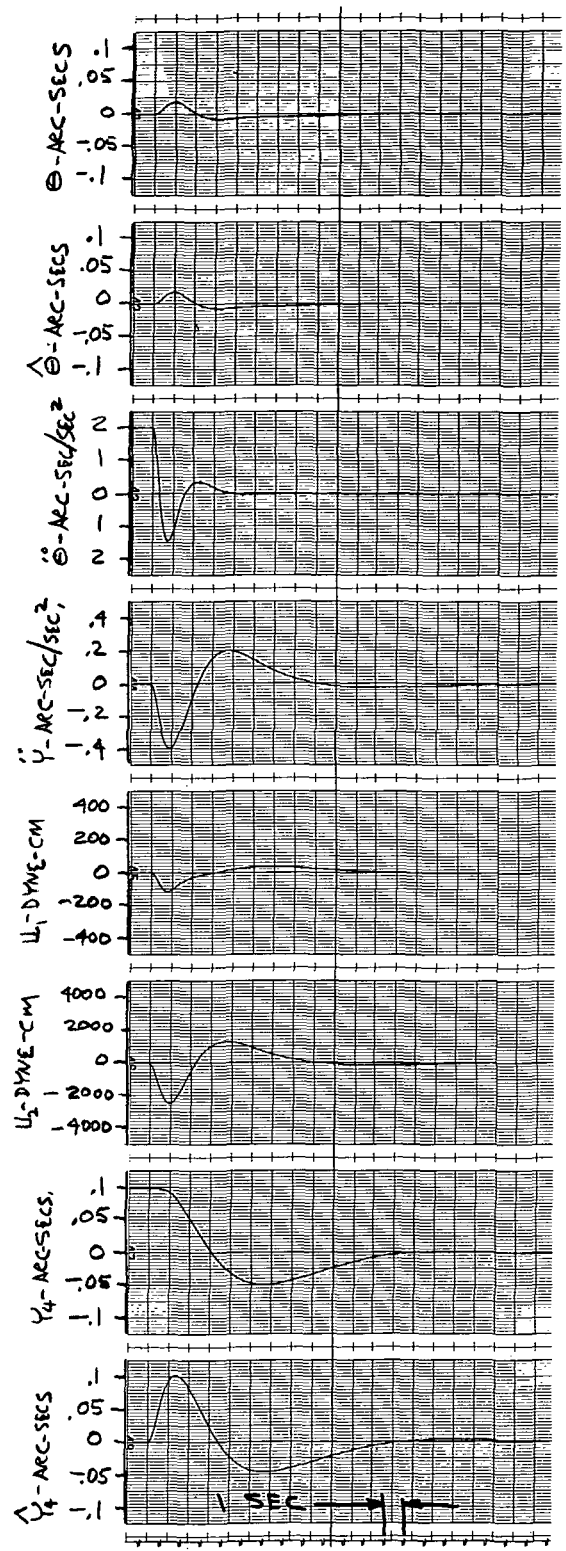


Fig. G-20 Initial Condition Response to $Y_4(0)$ = 0.1 arc sec

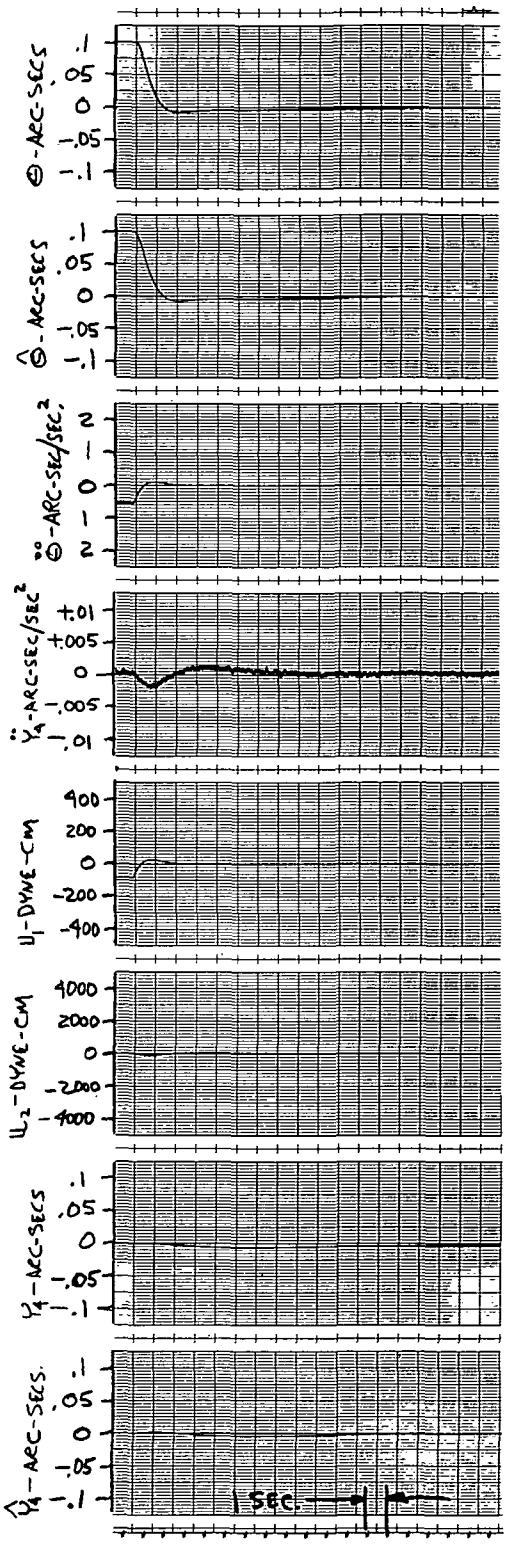


Fig. G-21 Initial Condition Response to $\theta(0) = \hat{\theta}(0) = 0.1$ arc sec

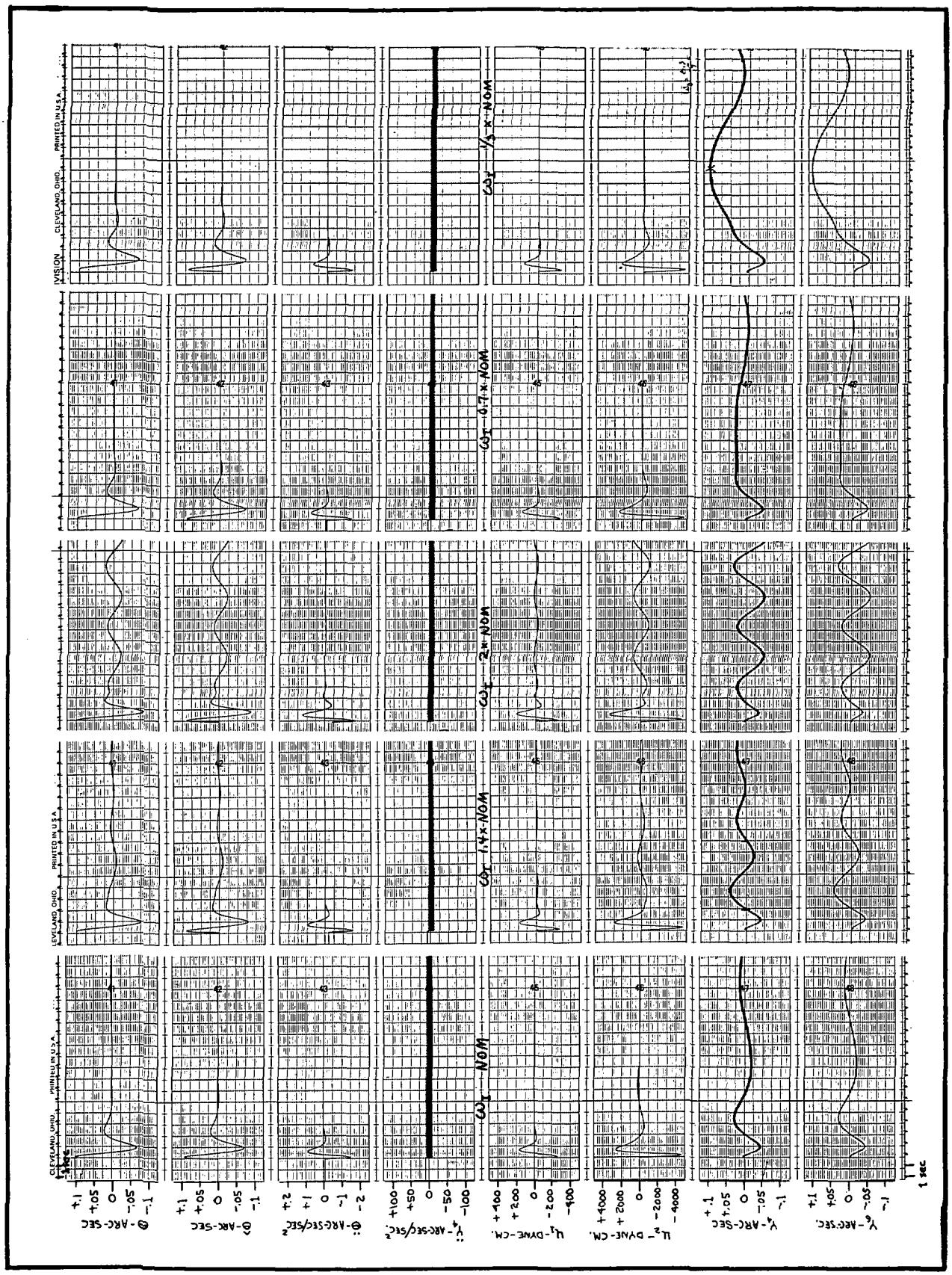


Fig. G-22 Variation of the Quartz Block Mechanical Vibration Frequency

estimator pole (this pole can be thought of as the outer-loop estimation pole). In the third run in the figure, the flexure spring constant in the plant is tiwce that in the estimator. For a modeling error this large, both the inner and outer body go unstable at the frequency of the estimator's outer-loop pole. In the 4th run, the plant's spring constant is 0.7 times that in the estimator model. This produces a lower frequency oscillation in the outer body. In the last run the plant's spring constant is one-third as large as that in the estimator model. For this modeling error, the outer body is only marginally stable. For lower than estimated inner loop mechanical frequencies, the outer satellite goes unstable at the dominate outer-loop control frequency instead of at the dominate outer-loop estimator frequency.

It is understandable that flexure spring constant modeling errors would significantly degrade control of the outer body because, the estimator depends on the coupling through the flexure to drive the quartz block in a way that can be used to predict the outer body motion. When the coupling frequency is not accurately known, the estimator makes poor estimates of the outer body attitude and rate, and there is little chance of good control or damping. If a gimbal angle pick-off was used together with the telescope error signal to drive the estimator, then the system tolerance for spring constant modeling errors would be much greater. Without this measurement the inner body mechanical vibration frequency must be known and constant to ±20 or ±30 percent.

The dewar wall mechanical vibration frequency was varied between 25 and 150 rad/sec in the simulations. These runs showed little effect on the system response to an initial condition on θ. The root-locus plot in Section G.2 shows that the high frequency plant poles have little effect on the control poles, if the plant poles are as high as 50 rad/sec. The BODE plot in Fig. G-3 shows that it is desirable to place these frequencies well above 50 rad/sec.

Figure G-23 shows the effect of variation of the gain through which the estimate of $\int\theta$ drives the inner actuator. As in the previous figure and in the sequence of figures which follow the telescope response to an initial condition error is used to show the effect of gain variation. Additional effects might appear if initial conditions were placed on other variables or if other types of response were simulated. Noise response would be an especially interesting alternative. Time was simply not available in the mission definition study to examine the effect of gain variation on more than one type of response. In Fig. G-23, the effect of varying the gain from $\int\theta$ to the inner actuators can only be detected in the last (right hand) of the three runs. The fact that the first and second runs are identical shows that the chosen nominal gain is low enough that integral control does not interfere with transient response to errors within the telescope's linear range. Only for 10 times the nominal gain is the effect of the added stiffness pronounced enough to cause concern. Therefore, the system is very insensitive to variation of this gain.

Figure G-24 shows how variation of the controller gains through which θ drives the inner actuators affects the response to an initial condition on θ. The system is more sensitive to variation of this gain than the previous one. Surprisingly, the $\int\theta$ signal to the inner actuator and the θ signal to the helium thrusters effectively null the initial θ error even with the θ gain to the actuators set at zero. This response is shown in the left hand run in the figure. For five times nominal gain, the increased stiffness and decreased damping in the telescope response are evident. Nevertheless, the system has a comfortable margin for variation of this gain.

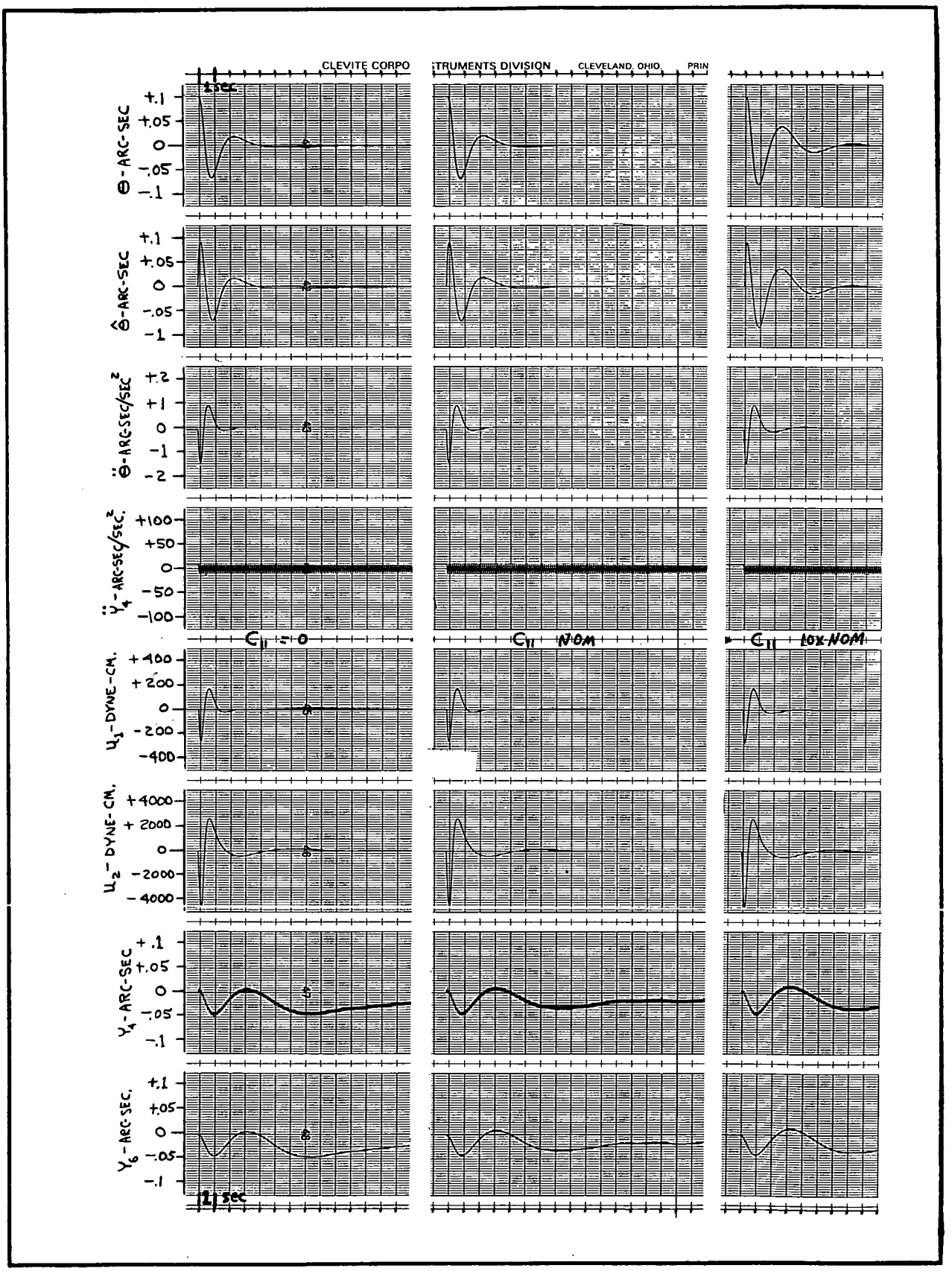


Fig. G-23 Variation of the Control Gain from $\int\theta$ to u_1

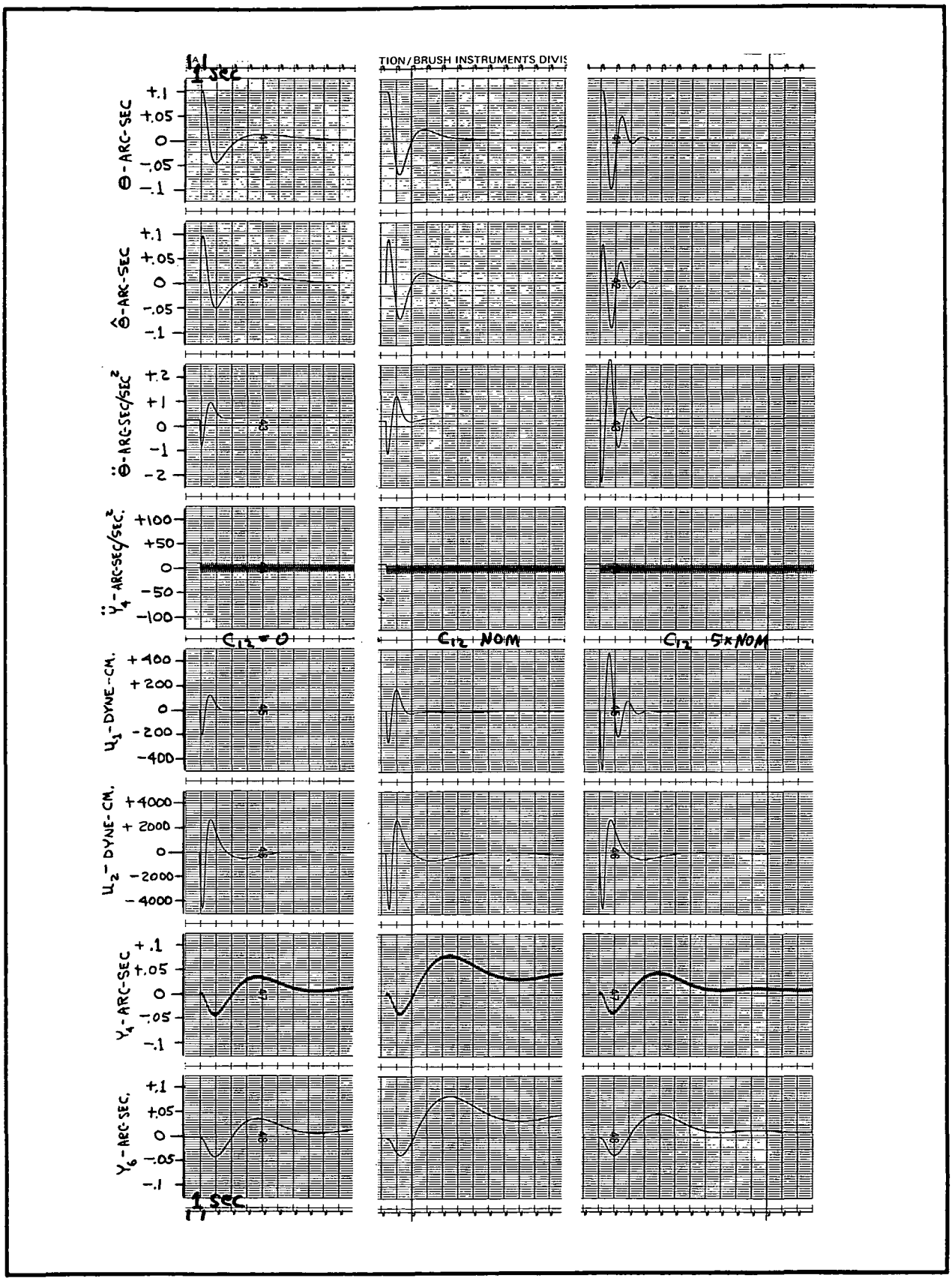


Fig. G-24 Variation of the Control Gain from θ to u_1

Figure G-25 shows the effect of variation of the controller gain through which $\dot{\theta}$ drives the inner actuators. This gain is the principal source of damping in the telescope motion. As might be expected, the system is unstable when this gain is set at zero. The oscillation in θ is uncomfortably large for this gain one third of nominal as can be seen in the left hand run in the figure. The response is satisfactory for up to seven times nominal gain, as can be seen in the right hand run in the figure. Note, however, that the initial spike in the acceleration trace is over twice as large as for nominal gain indicating increased noise sensitivity. This system has a comfortable margin for variation of this gain.

The next two controller gains whose variations were simulated are those through which the estimates of the outer body attitude and rate drive the inner actuator. The runs showed that the response is highly insensitive to variation in these "cross-loop" gains.

In the next five series of computer runs, the effect of variation of the gains through which the estimator output drives the helium thrusters was investigated. The first three sets of runs simulated the effect of varying the cross-loop gain through which the three telescope state-estimates drive the thrusters. As was the case where the outer body states drove the inner actuator, the system is very insensitive to variation of these gains. The $\int\theta$ gain on the thrusters had greatest effect, but the effect is small and acceptable for a gain ten times nominal.

Figure G-26 shows the effect of varying the gain through which the Y_4 estimate drives the helium thrusters. The system is surprisely well behaved for zero gain. It is possible that the $\int\theta$ gain, driving the thrusters, gives the outer-loop enough stiffness to maintain control. On the other hand, it is possible that the initial condition response to θ doesn't drive the outer body in a way that

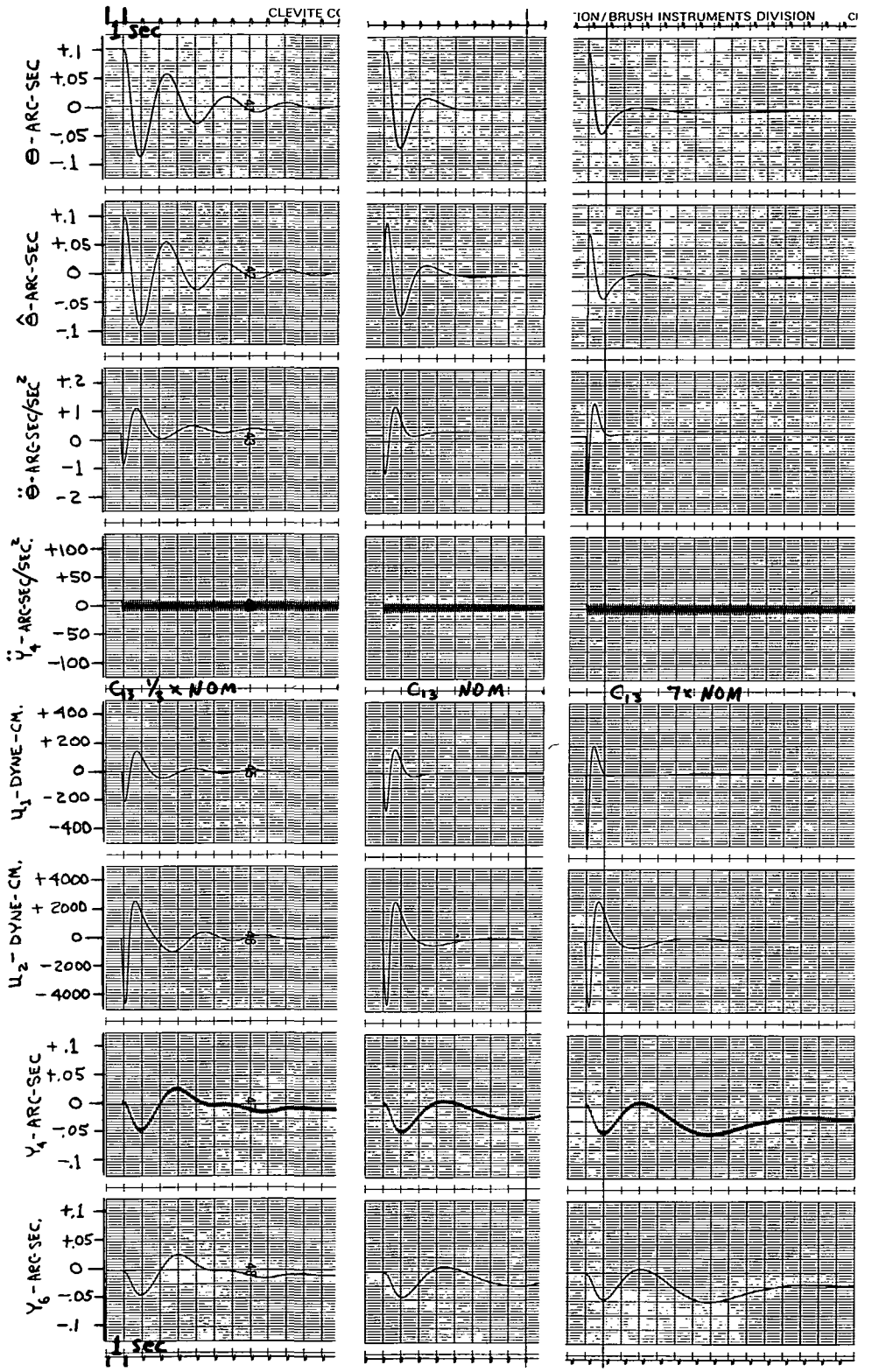


Fig. G-25 Variation of the Control Gain from $\dot{\theta}$ to u_1

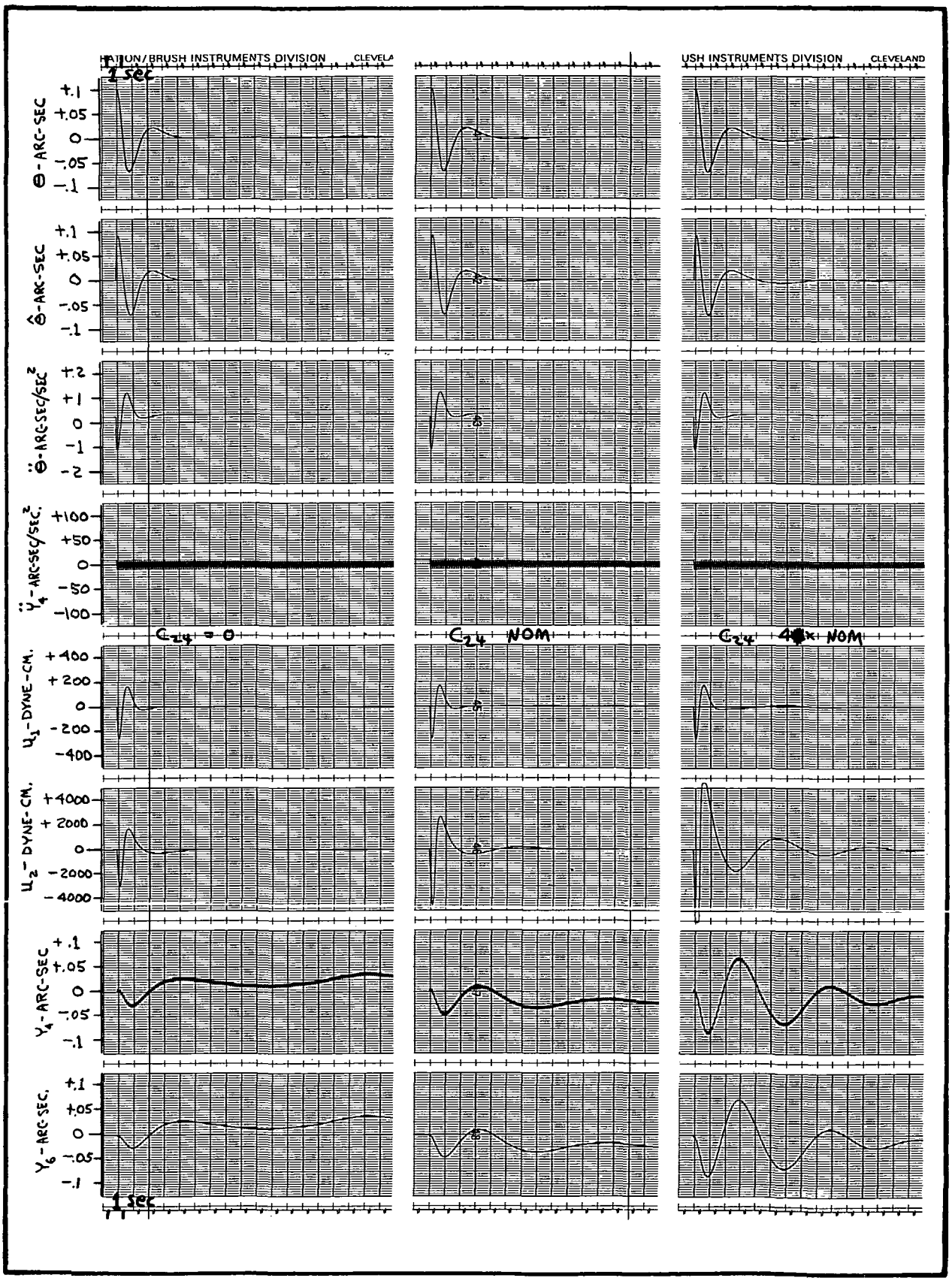


Fig. G-26 Variation of the Control Gain from Y_4 to u_2

illustrates the system's weakness with this gain set to zero. Responses to initial conditions on the outer body should be simulated to verify that reduction of this gain has an acceptable effect. Increasing this gain increases the stiffness in the outer control loop and reduces the damping on the outer body. This can be seen in the right hand trace in the figure. The system appears to have a comfortable margin for variation of this gain.

Figure G-27 shows the effect of variation of the gain through which the estimate of $\dot{Y}_4$ drives the helium thrusters. As might be expected, nulling this gain allows the outer body to go unstable. The response was satisfactory for one-half times the nominal gain and remained excellent for up to ten times the nominal gain. These computer outputs were not available for inclusion in the figure. The system has a good margin for variation of this gain.

The next five sets of computer runs used the system response to an initial condition on θ to show the effect of variation of the filter (or estimator) gains. These are the five gains through which $Z - \hat{Z}$ (really $\theta - \hat{\theta}$) drive the plant model within the estimator.

As might be expected from the system's lack of sensitivity to variation of the controller gains on $\int\theta$, the system is insensitive to variation of the estimator gain through which $Z - \hat{Z}$ drives $\int\hat{\theta}$ in the plant model. These computer runs are not shown because of the similarity of the traces for gains from zero to 10 times nominal.

Figure G-28 shows the effect of variation of the estimator gains through which $Z - \hat{Z}$ drives $\hat{\theta}$. The effect is quite dramatic and interesting. The root-locus plots of Section G.2 help explain the results. For less than nominal gain $\hat{\theta}$ oscillates at the higher (or telescope) estimator dominate frequency of about 6 rad/sec.

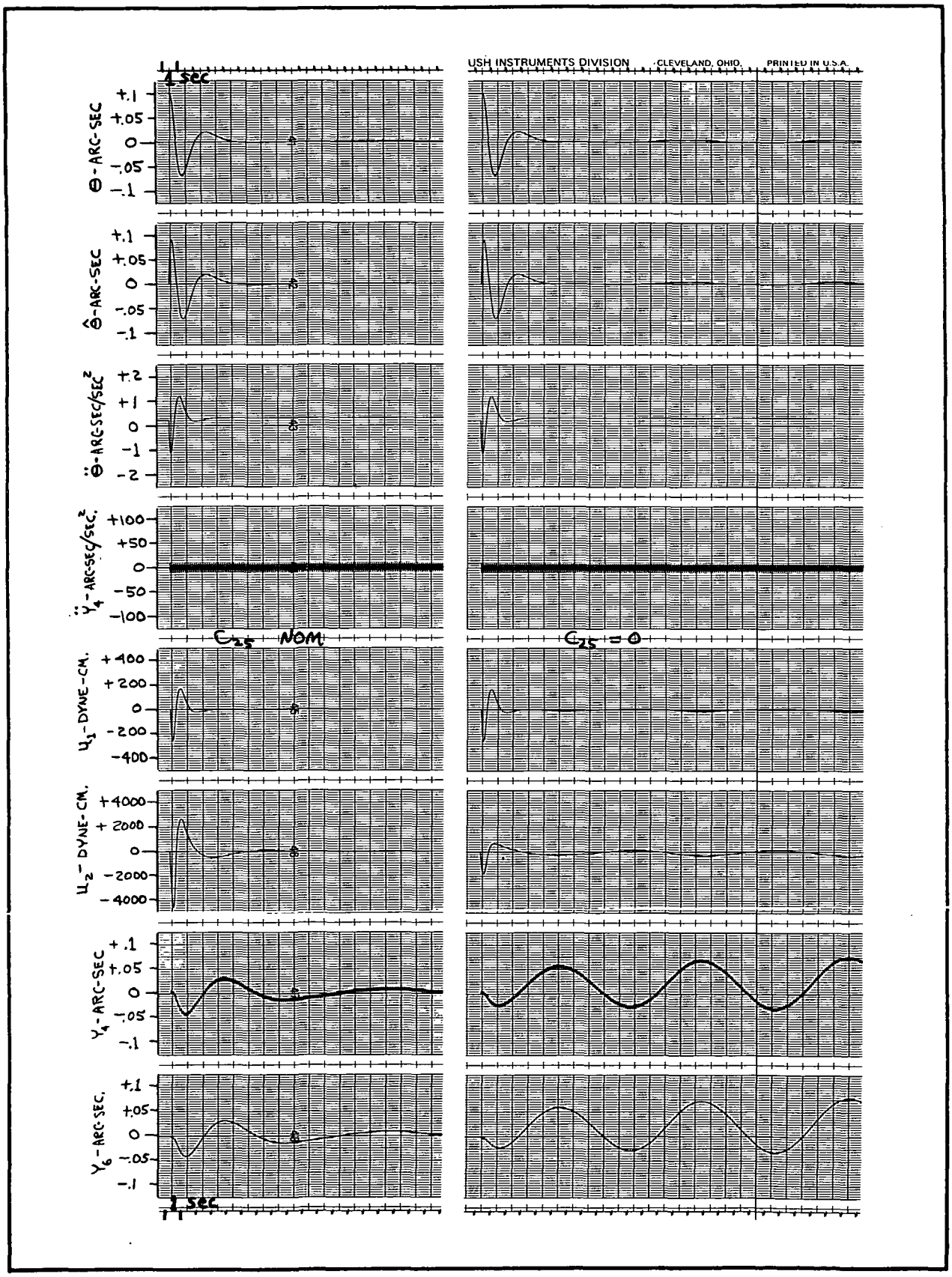


Fig. G-27 Variation of the Control Gain from $\dot{Y}_4$ to u_2

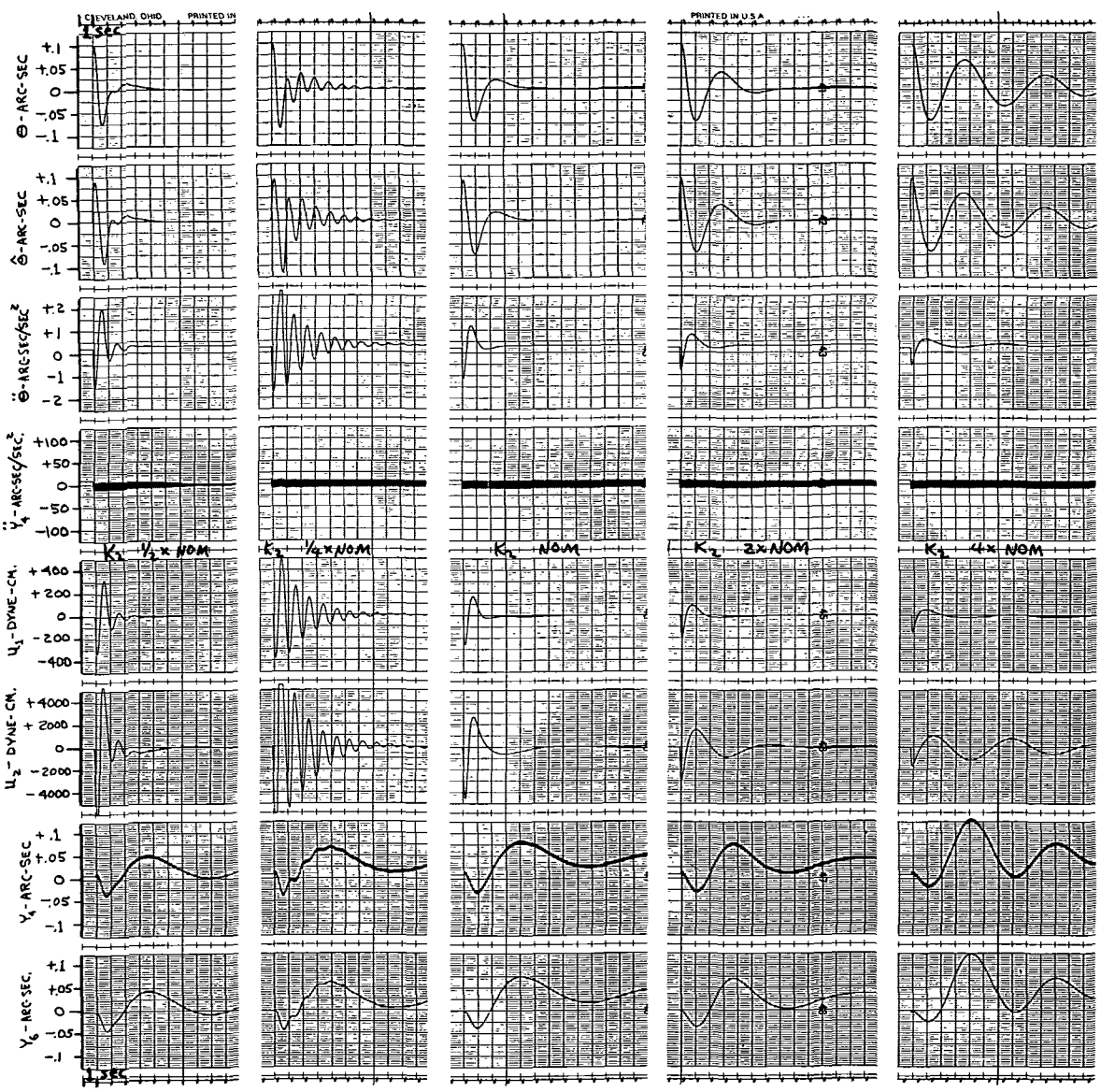


Fig. G-28 Variation of the Estimator Gain from $\hat{Z}$-$\hat{Z}$ to $\hat{\theta}$

By carefully comparing the two uppermost traces in the figure, the error in the $\hat{\theta}$ estimate is evident. This erroneous estimate drives the inner actuators and helium thrusters which in turn reinforces the oscillation by driving the quartz block and outer body. For higher than nominal gain $\hat{\theta}$, θ, u_2, and Y_4 and Y_6 oscillate with poor damping at the lower (or outer-body) estimator dominate frequency of about 1 rad/sec. The error in the $\hat{\theta}$ estimate appears to be small in these runs (on the right hand side of the figure). We believe that the error responsible for the poor response is in the estimate of outer body motion $\hat{Y}_4$. Unfortunately, this trace is not displayed in the figure. The system is quite sensitive to variation of this gain. It is necessary to place this gain within ±20 to ±30 percent of nominal.

The system is also quite sensitive to variation of the estimator gain through which the Z- $\hat{Z}$ drives $\dot{\hat{\theta}}$. The left hand run in Fig. G-29 shows the oscillations which occur when this gain is reduced from the nominal value. The system is unstable for this gain one-fourth times nominal. The frequency at which the system goes unstable is the dominate control frequency of the inner loop. It might be expected that the telescope would go unstable at its dominate control frequency for reduced gain because, reducing this gain reduces the authority of the rate estimate through the controller. For higher than nominal gain the $\dot{\hat{\theta}}$ estimate is apparently emphasized at the expense of the $\dot{\hat{Y}}_4$ estimate. Unfortunately $\dot{\hat{Y}}_4$ is not shown in the figure. In any case the outer satellites stability is degraded by increasing this gain. The frequency of oscillation of the outer satellite is the dominate outer-loop controller frequency of about 0.5 rad/sec. As was the case for the K_2 gain, care should be taken to place this gain to within ±20 to ±30 percent of the nominal value.

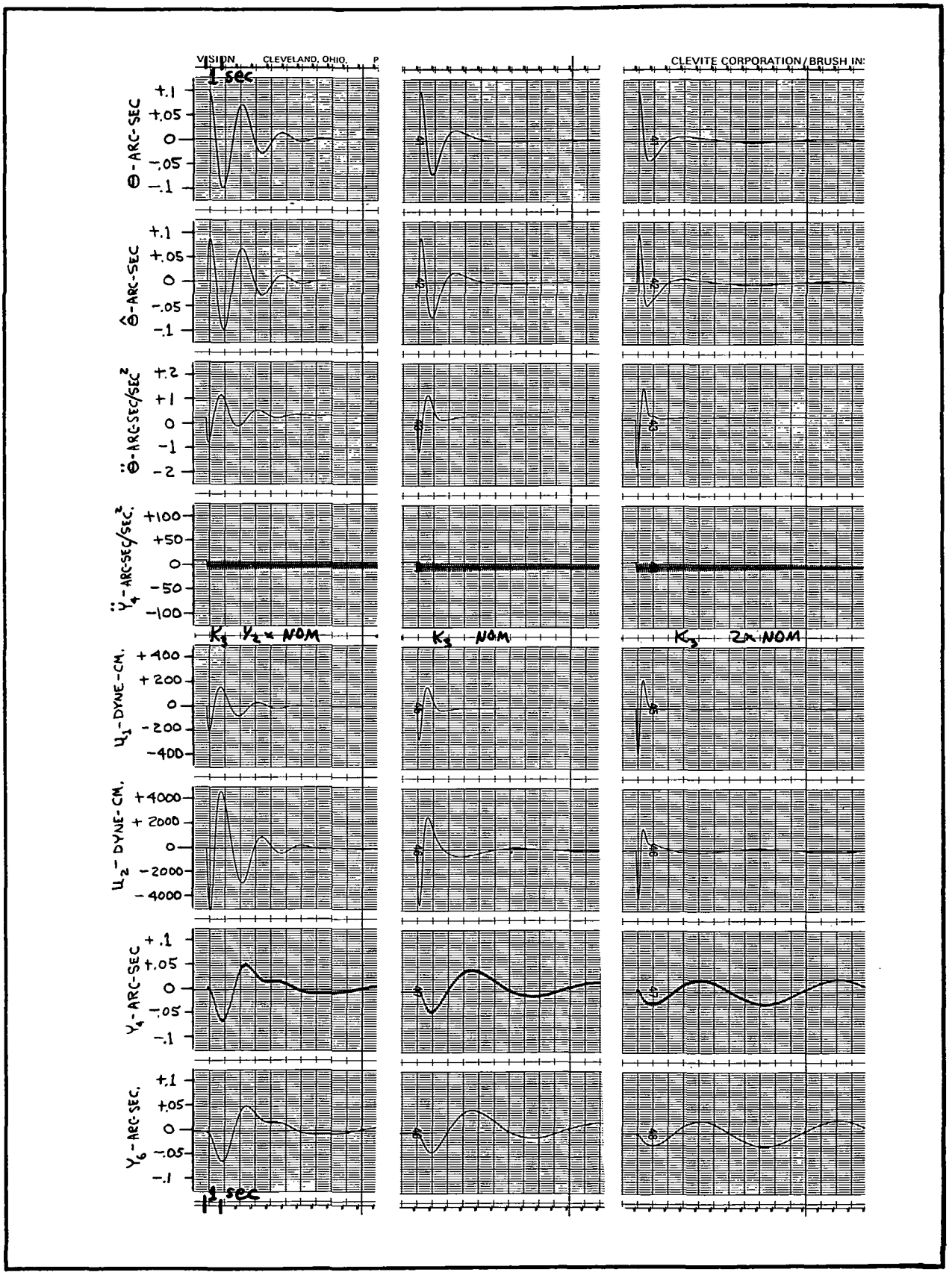


Fig. G-29 Variation of the Estimator Gain from $Z-\hat{Z}$ to $\dot{\hat{\theta}}$

The effect of variation of the gain through which Z- $\hat{Z}$ drives the outer body state estimates have converse effects to those caused by varying the gains which drives the inner bodies state estimates. Figure G-30 shows that the system goes unstable at the lowest dominate frequency of the estimator for lower than nominal estimator gain from Z- $\hat{Z}$ to $\hat{Y}_4$. For higher than nominal gain the system goes unstable at the highest estimator dominate frequency. (The converse was true with respect to the estimator gain from Z- $\hat{Z}$ to $\hat{\theta}$.) Apparently, the relative values of these two gains is important in the sense that increasing one decreases the effectiveness of the other. This reemphasizes the importance of accurately placing these gains.

Figure G-31 shows that, as was the case for the estimated gains that drive the inner and outer body position estimates, the effect of variation of the estimator gains from Z- $\hat{Z}$ to $\hat{\dot{Y}}_4$ is the converse of the effect of varying the gain from Z- $\hat{Z}$ to $\hat{\dot{\theta}}$.

The left hand trace in the figure shows that a reduced gain produces a lightly damped oscillation of the outer body at the dominate outer-loop controller frequency of about 0.5 rad/sec. The right hand run in the figure shows that increasing this gain causes the telescope to oscillate at the dominate inner-loop frequency of the controller. For four times nominal gain the oscillation was much worse, but the system was still stable.

In summary, the last four sets of runs show that the system is generally more sensitive to variation of the estimator gains than it is to variation of the controller gains.

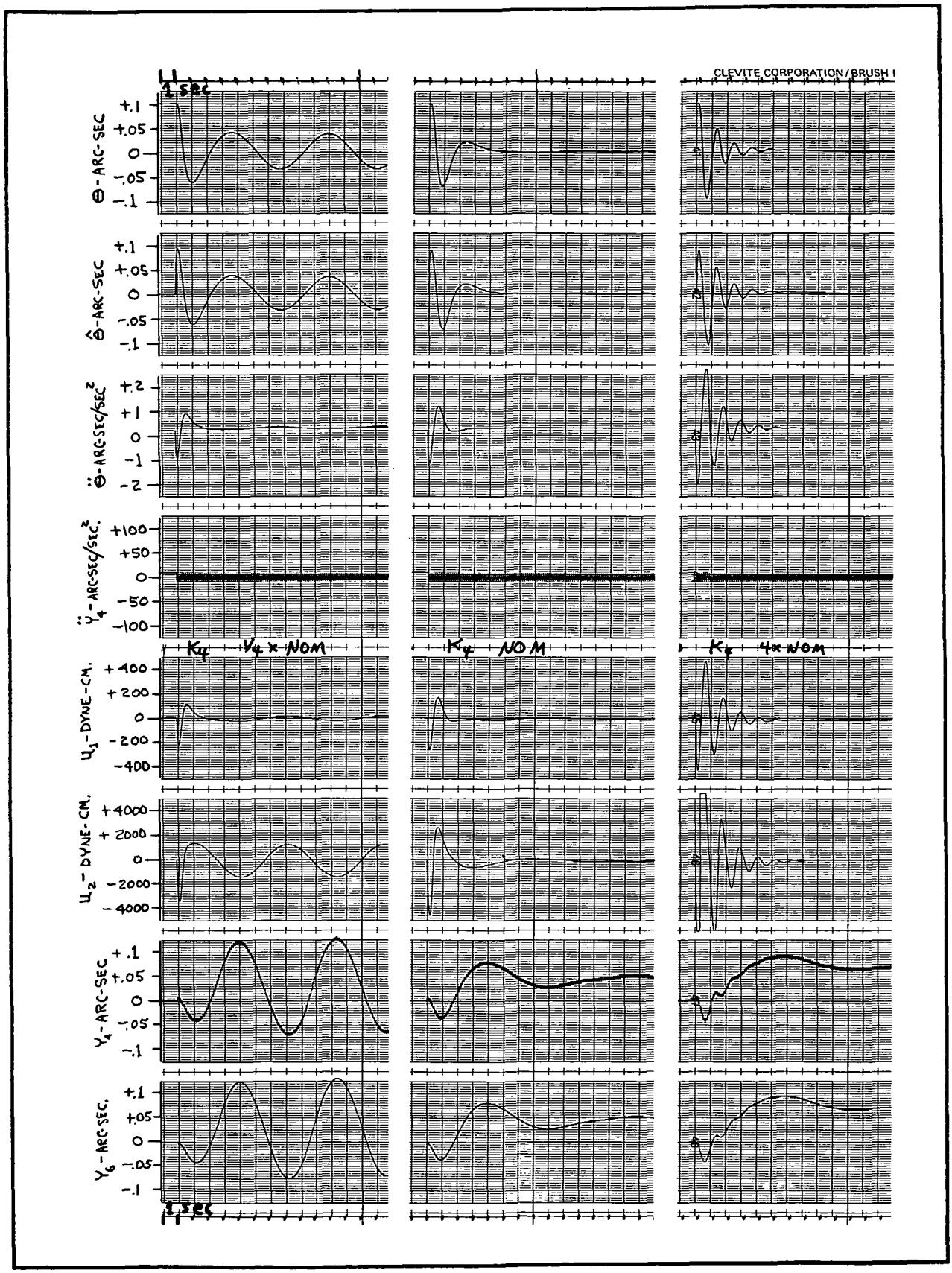


Fig. G-30 Variation of Estimator Gain from $Z-\hat{Z}$ to $\hat{Y}_4$

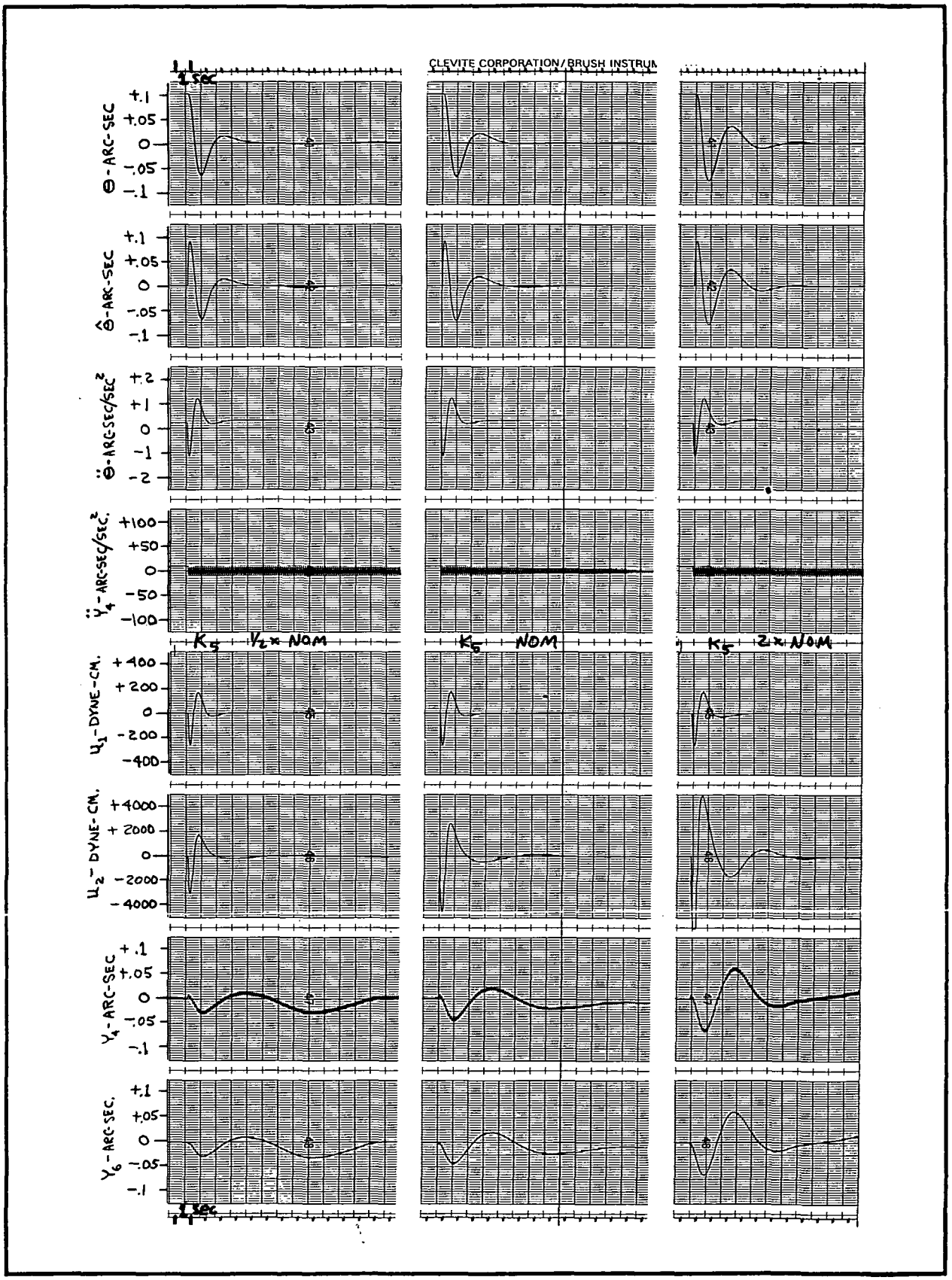


Fig. G-31 Variation of the Estimator Gain from $Z-\hat{Z}$ to $\hat{\dot{Y}}_4$

In the next three sets of runs the gains on the control torquers are varied. In the first two sets of runs the gains on the torquers are varied, but only in the plant. In the third set of runs, these gains are varied identically in both the plant and in the estimator's model of the plant. As should be expected by now, the system is far more sensitive to the former variations because they cause modeling errors. The root-locus plots of Section G.2 graphically explain the difference in the way the dominate poles move.

Figure G-32 shows the effect of varying the inner actuator gain only in the plant. For a gain that is 60 percent of nominal, the system has a large amplitude lightly damped oscillation at the inner-loop dominate controller frequency. On the right side of the figure it may be seen that doubling the inner actuator gain produces pronounced lightly-damped oscillation but this time at the highest dominate frequency of the estimator. The system is sensitive to inner actuator gain changes which are not reflected in the estimator model. It is important to model the actuator gain accurately.

Figure G-33 shows that the system is also quite sensitive to changes in the helium thruster gains which are not reflected in the estimators model of the plant. For one-half the nominal gain the outer body oscillates with light damping at the dominate outer-body controller frequency while it oscillates at the dominate inner-body controller frequency for higher than nominal gain. This sensitivity to changing thruster gain is of great concern because of the expected variation in the helium boil-off rate (and therefore in the thruster gain) during the mission. However, a ±50 percent variation in the thruster gain is probably tolerable.

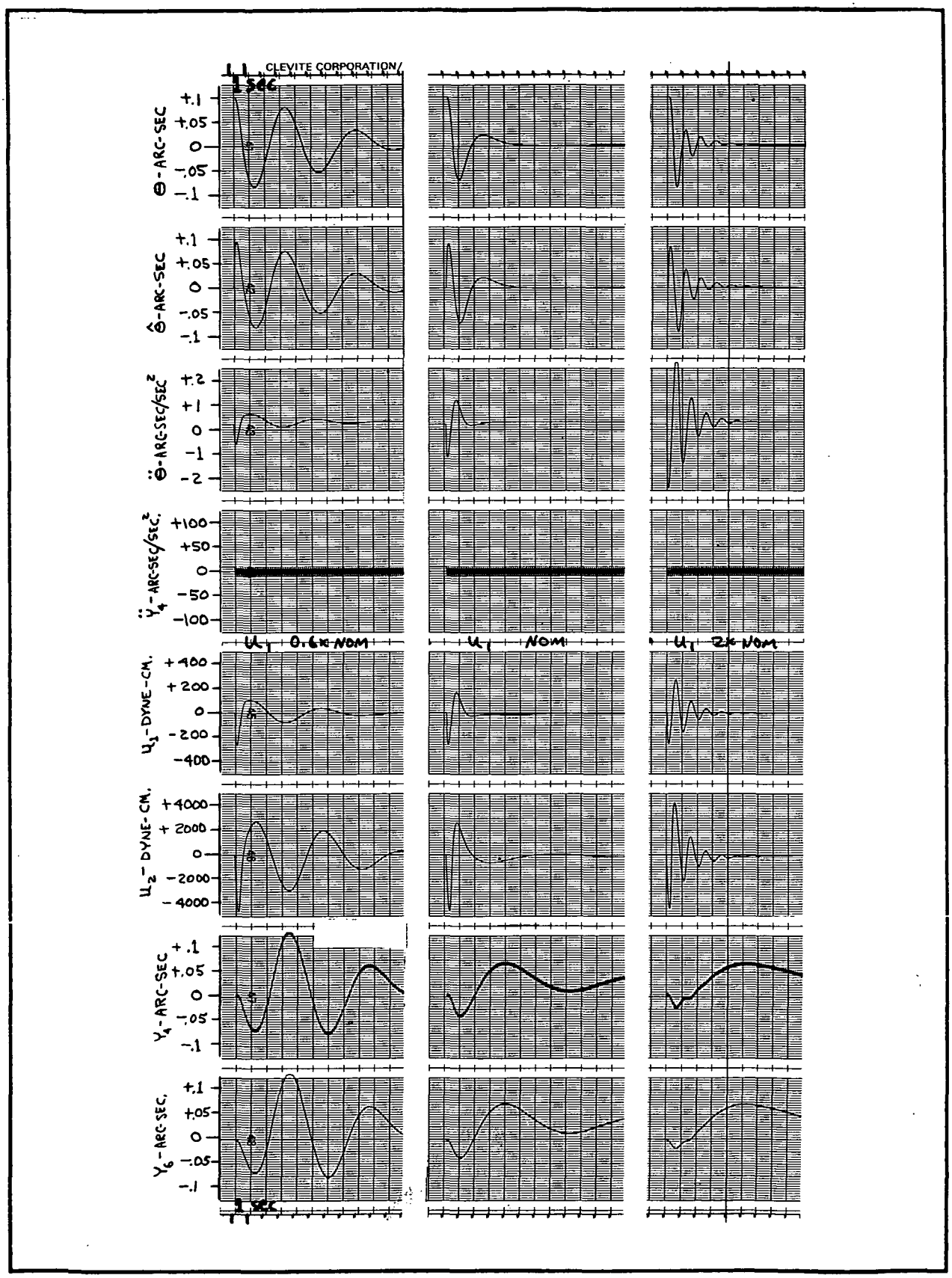


Fig. G-32 Variation of u_1 Gain in the Plant Only

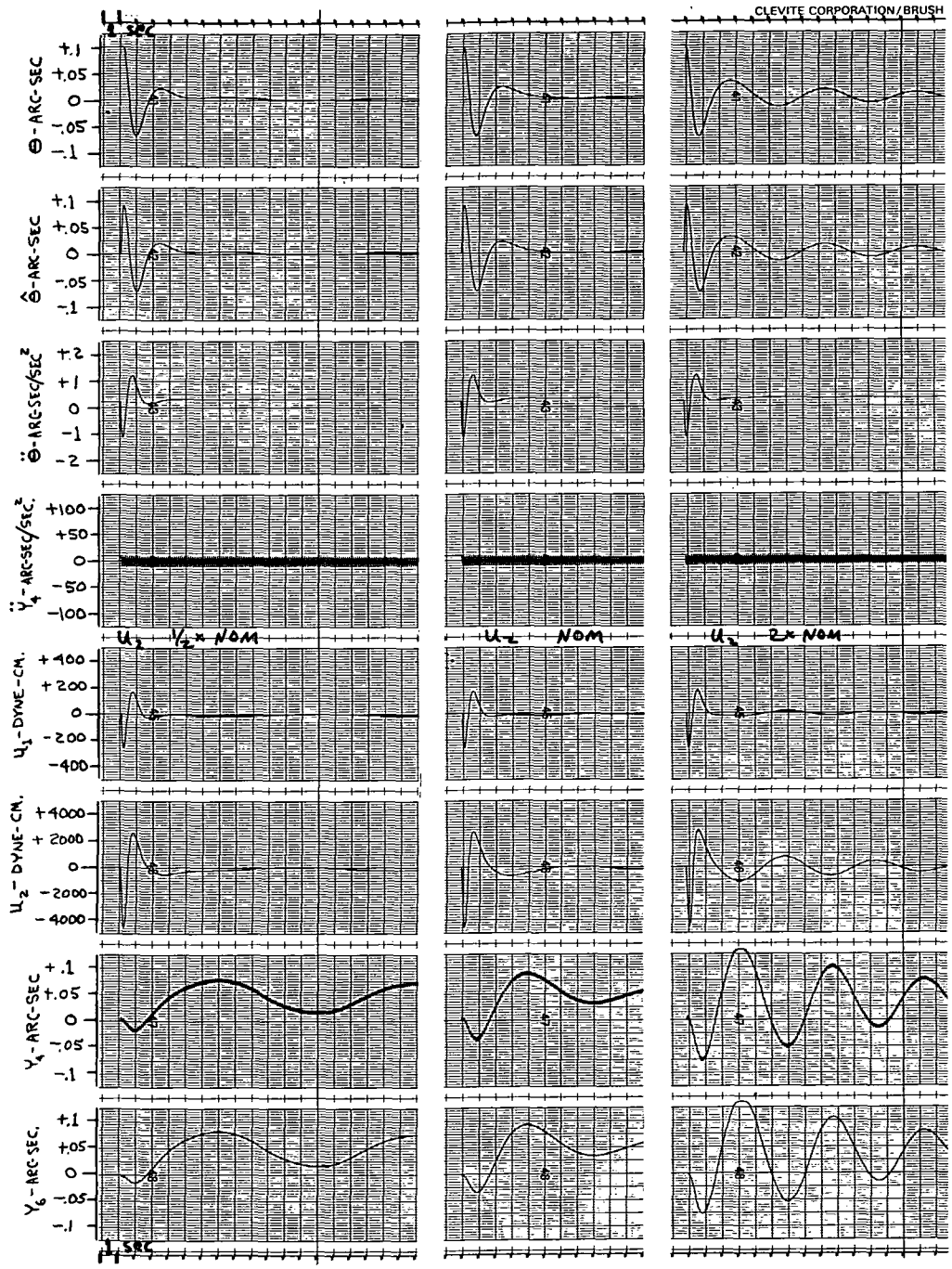


Fig. G-33 Variation of u_2 Gain in the Plant Only

Figure G-34 shows that the system has substantially greater margin for variation of the inner actuator gain if that gain is varied both in the plant and in the estimator's model of the plant. The system oscillation at the controller's dominate inner-loop frequency is pronounced but probably acceptable for one-fourth times the nominal gain in both plant and model. At the other extreme, the response is probably acceptable for 10 times nominal gain in both plant and model. However, the peak acceleration is nearly three times nominal. The final set of computer runs showed that the system is also far less sensitive to variation in thruster gain if the gain is varied in both the plant and in the estimator's model of the plant instead on only in the plant.

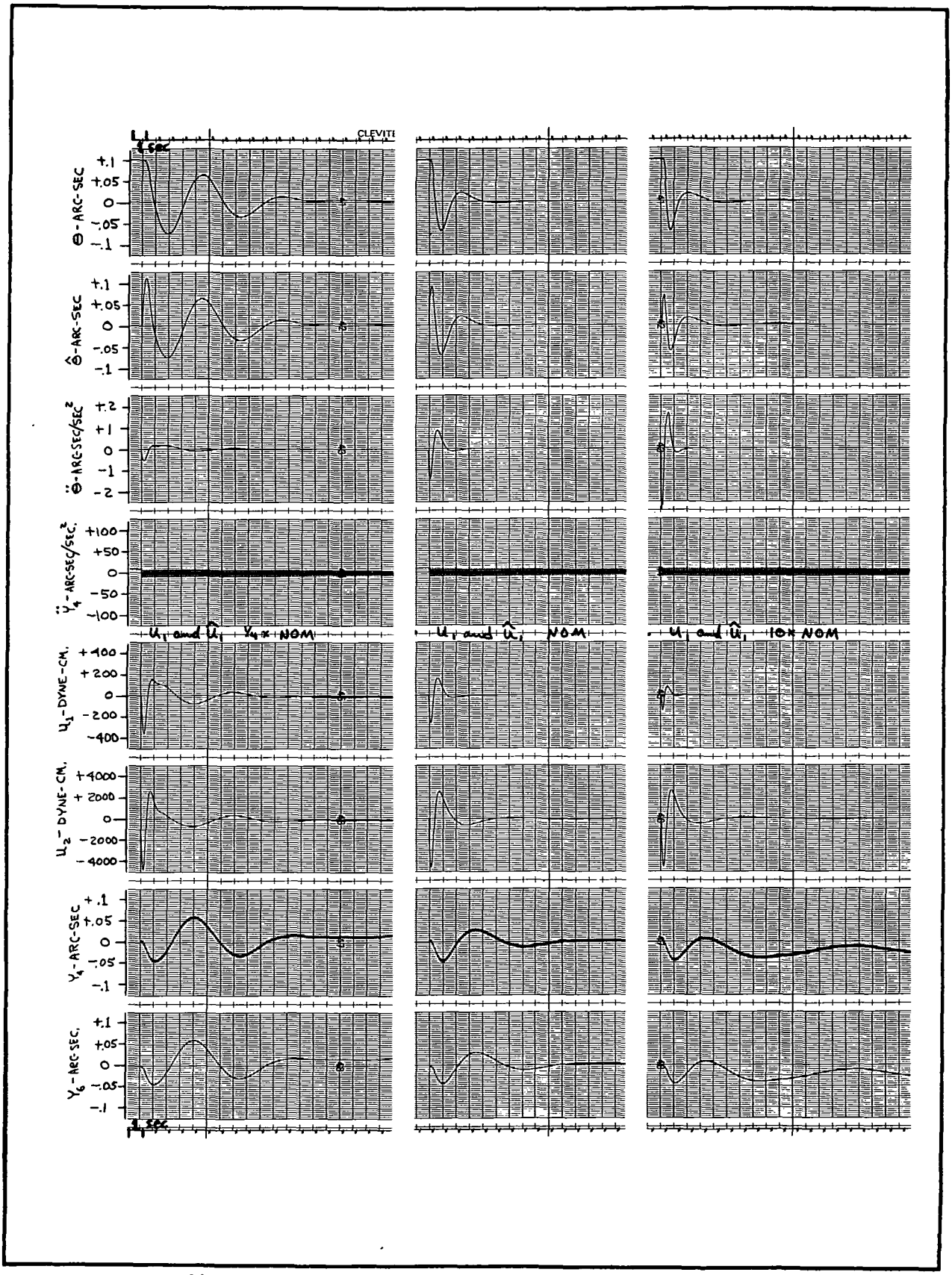


Fig. G-34 Variation of the u_1 Gain in Both the Plant and Estimator Model


Ball